MODELLING IMPROVEMENT AND PITCHPOLING ASSESSMENT

OF WAVE ENERGY STRUCTURES

A Dissertation

by

HAO WANG

Submitted to the Office of Graduate and Professional Studies of
Texas A&M University
in partial fulfillment of the requirements for the degree of

DOCTOR OF PHILOSOPHY

| | |
|---|---|
| Chair of Committee, | Jeffrey M. Falzarano |
| Committee Members, | Moo-Hyun Kim |
| | Richard S. Mercier |
| | Alan B. Palazzolo |
| Head of Department, | Sharath Girimaji |

August 2020

Major Subject: Ocean Engineering

ABSTRACT

Nonlinear effects become more important in predicting the motions of a wave energy structure (WES), which is subject to large (relative to its dimensions) motion amplitudes. To model the WES more accurately, a time-domain program (SIMDYN) is further developed. In particular, SIMDYN's "blended" option improves the linear option by accounting for not only the nonlinearity of important external forces but also the nonlinearity due to large body rotations (i.e., inertia forces). To reveal the significance of these nonlinear effects, forced motion analysis are performed. The simulation results from SIMDYN under the blended option are examined by model test correlations, which has seldom been done before for a WES.

Besides that, the other important discrepancy in WES modelling: viscous damping is studied. By applying an advanced system identification technique, Reverse-Multiple Input Single Output (R-MISO), to model tests of a WES under random waves, viscous damping of a realistic (typical catenary moored) system is studied. Based on the comparisons between the frequency dependent transfer functions from the simulations and those from the model tests, reasonable linear or quadratic damping have been extracted. In a sense, this methodology can become a powerful alternative in damping corrections for WES under random sea states.

Compared to other quantities of interest which have been extensively studied in typical design practice, the dynamic stability has not been investigated adequately. The Melnikov function model and the Markov process model are two efficient approaches providing

quantitative predictions of capsizing. In the last part, to predict the pitchpoling risks of a moored floating cylinder representing a generic WES under random excitation, the two methods has been explored. Using the Melnikov approach, the rate of phase space flux was evaluated to quantify the dynamic stability. This approach is compared with the Markov approach, which evaluates the mean first escape rate to quantify the vessel's dynamic stability. The two methods are investigated systematically by varying important parameters, which include the linear and quadratic damping, the mooring systems and the sea states.

# ACKNOWLEDGEMENTS

CONTRIBUTORS AND FUNDING SOURCES

**Contributors**

**Funding Sources**

TABLE OF CONTENTS

LIST OF FIGURES

LIST OF TABLES

# 1. INTRODUCTION

Wave energy is a promising renewable energy resource, and it is distributed extensively in coastal areas (Astariz and Iglesias 2015). According to the Bureau of Ocean Energy Management, the recoverable wave energy in the U.S. is capable of powering more than 100 million homes. In terms of energy density, the wave power is of a higher order of magnitude compared to solar and wind power. In addition, the electricity supply from wave energy can be forecast days in advance and it is available all day and night (Columbia Power Technologies 2017).

Many wave energy structures (WESs) were designed to convert wave energy to electricity (Falnes, 2002; Drew et al., 2009; Lópeza et al., 2013). Typical wave energy structure (WES) includes oscillating water columns (OWC), attenuators, point absorbers (PA), oscillating wave surge converters (OWSC), submerged pressure differential devices (SPD) etc. (Falcão 2010). While some WESs are fixed onto the shore or the seabed, many are floating (see Figure 1.1) or submerged structures. It is worth noting that a WES may be any structure in the wave energy conversion system. In the dissertation, the floating power system (FPS) used in the model test correlations is a necessary unit in the wave energy conversion system, but the FPS itself is not a wave energy converter (WEC). That is the reason why the more general term wave energy structure or "WES" is used to refer to it.
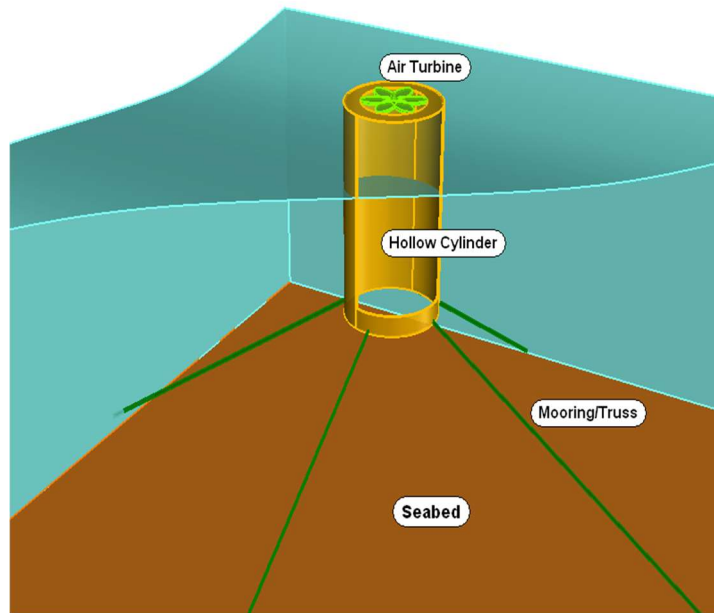
**Figure 1.1** Floating wave energy structure (OWC)

Floating systems positioned by mooring lines is the typical form of many wave energy structures. For instance, in the department of energy sponsored competition for the wave energy devices (namely, "wave energy prize"), the most successful design (namely, AquaHarmonics) is of the point absorber form (see Figure 1.2).
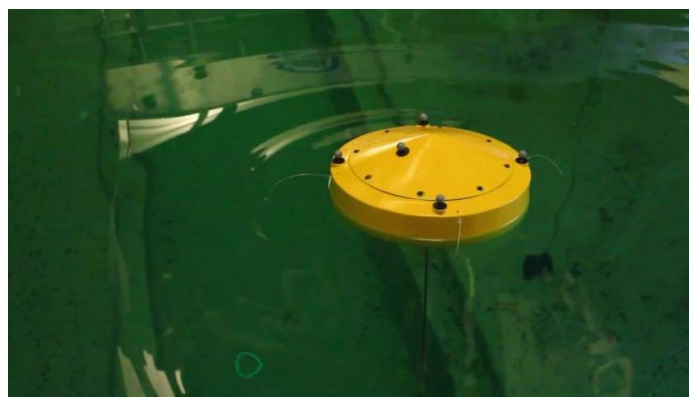


**Figure 1.2** AquaHarmonics, reprinted (Water Power Technologies Office, 2016)

As wave passes by, AquaHarmonics rises and falls on the waves and spins generator through a tether (Water Power Technologies Office, 2016). In fact, the point absorber (PA) is also one of the most mainstream WEC types (Shami et al., 2018). The largest U.S. wave energy device manufacturer, Ocean Power Technologies, also launched a point absorber as its flagship product. Therefore, this dissertation categorizes the most common/general form of WES as:

- Geometry: typical floating body

- Motions: free floating with six degrees of freedom

- Positioning: (traditional) mooring system

The concurrent status of WESs has been reviewed in the Extreme Conditions Modelling Workshop (ECMW) when experts from industry and universities gathered in Golden, Colorado (Coe et al., 2014). It was summarized that most WESs operates in two modes: the "normal" mode when the wave energy is converted into electricity (Korde and Ringwood, 2016); and the "survival" mode when large amplitude motions/loads are induced (Coe et al., 2014). Design optimizations, including the implementation of control algorithms (Korde and Ringwood, 2016), mainly aim at improving the output in the normal mode. On the other hand, the reliability and the cost of WESs depend largely on the survival mode.

It's worth noting that this dissertation does not consider the power take off problem. The power take off (i.e. generator) works in the power conversion chain (PCC), which is also subject to harsh sea states (e.g. large relative motion between the PTO's

stator and slider). Currently the survival strategy of many WESs is to either "lock" the PCC or allow "freewheeling" to reduce motions/loads for this sensitive component (Coe et al., 2014). Life extending controls (LECs) that can help reduce the PCC forces, are also developed for WECs. However, the "natural" status for PCC is still either "locked" or "freewheeling". When the PCC is locked, the WEC moves as a rigid body (six degree of freedom at most). When the PCC is freewheeling, then the stator (usually positioned by the mooring system) moves as a rigid body, the slider yields an additional degree of freedom. It can noticed that design details are needed for accurately modelling the PCC, so its influences will be considered in future studies.

As for the environmental variables (wave, wind and current) in the study, according to the ECMW (Coe et al., 2014), wave loads (due to regular and irregular waves) are the dominant element for WES's survival scenarios; wind is generally a marginal component (except for WESs with large areas above the water line, like OWCs); current exerts additional drag force in certain direction. As current practices of modelling for WESs are usually limited to the wave loading (e.g. Yu et al., 2015, Yu 2017), this dissertation will not consider the wind and current loading.

## 1.1. Background and the Research Scope Overview

Accurate numerical modelling is critical to both normal mode and survival mode. Numerical modelling is anything but new in traditional naval architecture and offshore engineering practices (Pastoor, 2002; Dietz, 2004; Reed and Beck, 2017). However, for WESs, concurrent numerical modelling was first reviewed comprehensively by experts from the relevant industry, universities, and national laboratories in the ECMW (Coe et

4

al., 2014). The ECMW concluded that more research in the numerical modelling area is necessary, because wave energy structures are different from traditional ships and offshore structures in two aspects.

The first significant problem pointed out by the ECMW is that WESs are usually subject to larger motion amplitudes (relative to their dimensions), therefore nonlinear effects become more important. To select the best pathway to develop the most appropriate modelling tool, existing hydrodynamic modelling methods are listed in Table 1.1. Generally, the cost and time involved in application of a modelling method (see Table 1.1) increases with its fidelity (Yu 2017). They were used comprehensively to take advantage of either their efficient turnaround time or high fidelity.

**Table 1.1** List of hydrodynamic modelling methods

|   | Hydrodynamics | Software |
|---|---|---|
| 1 | Morison's Equation (DNV 2010) | N/A |
| 2 | Linear time (frequency) domain potential flow (ANSYS Inc. 2011) | AQWA (ANSYS Inc. 2011), WAMIT (WAMIT Inc. 2013), Nemoh (Penalba et al., 2017) |
| 3 | Blended time domain potential flow (Reed and Beck 2017) | WEC-Sim (NREL and Sandia 2014), SIMDYN (Somayajula and Falzarano 2015) |
| 4 | Nonlinear time domain potential flow (Stern et al., 2008) | Aegir (Stern et al., 2008) |

**Table 1.2** Continued

| | Hydrodynamics | Software |
|---|---|---|
| 5 | Computation Fluid Dynamics (RANS (Yu et al., 2015), SPH (Yeylaghi et al., 2015), LES (Sagaut 2006) | STAR-CCM+ (CD-adapco 2014), OpenFoam (OpenFOAM Ltd. 2019) |
| 6 | Model tests (Lawson et al., 2015) (Physical modelling) | N/A |

The linear time-domain potential flow method (ANSYS Inc. 2011) is the most common method for the analysis of offshore structures (e.g., semisubmersibles). Inverse Fourier transforms are conducted on the linear frequency domain hydrodynamic analysis results to conveniently generate time series (e.g., the Froude-Krylov force time series). Model test correlations of WES responses with the linear time-domain programs have been performed by many researchers (e.g., Lawson et al., 2015). Though this is a basic and very efficient method, it does not address the nonlinear effects, which are important when waves and motion amplitudes are relatively large.

The blended time-domain method usually accounts for the nonlinearity in the Froude-Krylov forces, hydrostatic forces, and the equations of motion (inertia forces), while the remaining forces are computed using either linear or nonlinear modelling (Reed and Beck 2017). The blended method has been applied to simulate ship motions by many researchers (Umeda et al., 2012, Belenky et al., 2003, Chen 2002). Wave Energy Converter SIMulator (WEC-Sim), developed by the Sandia National Laboratory and the

National Renewable Energy Laboratory, incorporates the blended method option (Lawson et al., 2014), but it has not been compared with model test results of a WES.

The nonlinear time-domain potential flow method solves the fluid flow problem using the fully nonlinear free-surface boundary conditions instead of the linearized free-surface boundary conditions used in the linear and blended time-domain methods (Beck and Reed 2001). These nonlinear modelling approaches have been reviewed in past research (Penalba et al., 2017). But this method is calculationally intensive (i.e. it usually takes an order of magnitude more runtime than the blended time-domain method).

Computational fluid dynamics (CFD) methods overcome the discrepancies of many of the other methods based upon the assumptions of the potential flow theory (by including fluid viscosity); they are also used to simulate WESs. CFD methods include Reynolds-averaged Navier-Stokes (e.g., Yu et al., 2015), smoothed-particle hydrodynamics (e.g. Yeylaghi et al., 2015), and large eddy simulation (e.g., Sagaut 2006). These CFD methods are capable of capturing the full range of phenomena in extreme waves (see Ransley et al., 2017). Therefore, CFD methods are more accurate than the previously described methods, but the computational time is significantly longer than even the nonlinear time-domain method.

The blended time-domain method has been selected to model the WES motions under the assumption that it can address the nonlinear forces in a time-efficient manner. The previous research in the Marine Dynamic Laboratory (MDL) at Texas A&M University (where my research is conducted) has formed a foundation for such a tool: the frequency domain program MDL-HYDROD (Guha, 2016; Liu and Falzarano, 2017) and

time domain program SIMDYN (Somayajula and Falzarano, 2015). SIMDYN were originally developed to simulate the ship motion, usually those simulations consist of limited degrees of freedom (e.g. sway, heave and roll only). In this study, SIMDYN was improved so that it can account for the nonlinear effects of a WES with regards to Froude-Krylov forces, hydrostatic forces, and inertia forces. In addition, by coupling with the open-source Mooring Analysis Program, MAP++ (MAP++ Documentation 2019) and implementing other forces (e.g. slowly varying wave drift forces) when necessary, SIMDYN has become capable of accurately and efficiently simulating WES motions, which are six degrees of freedom.

Physical modelling/model tests are considered as the "gold standard" in hydrodynamics. Experimental study has been conducted on typical WESs such as the oscillating water column (e.g., Elhanafi et al., 2017), the point absorber (e.g., Sirnivas et al., 2016), and the oscillating surge wave energy converter (e.g., Ruehl et al., 2016). The model test correlations in these studies have examined and improved simulation tools in different ways. In this dissertation, the accuracy of the program was verified by correlating the simulations with open access model test results. These model tests were conducted on a floating power system (FPS) by the Beaufort Research and Hydraulics and Maritime Research Centre (HMRC). Designed to provide power and connection to the grid (Bosma et al., 2014), the FPS did not generate electricity in the model tests. This makes it a perfect benchmark model for the study herein.

With the improved modelling tool in hand, the remaining uncertainty lies mainly in the viscous damping. Actually, this is exactly what the ECMW pointed out as the other

aspect (the first aspect being the nonlinear effects) in which wave energy structures are different from traditional ships and offshore structures: WESs have much smaller scales, resulting in smaller Reynolds numbers, therefore accurately modeling viscous damping is more significant. Viscous damping is a "grey" area for modelling tools based on the potential flow theory and usually needs to be corrected manually. The viscous damping corrections can be achieved through empirical methods (Falzarano et al., 2015) or through free decay tests (Sirnivas et al., 2016; Handschel et al., 2015). However, WESs are relatively novel design, so the empirical equations for ship shaped hulls may not be applicable to the typical WES geometries. On the other hand, accessible WES model tests data are inadequate and limited. For example, for the FPS, a free decay test result was not available.

As an alternative, the viscous damping can be evaluated through the previously developed system identification technique (Somayajula and Falzarano, 2016). It can directly deal with cases under random sea states, which are the most common situations, as the actual sea states in nature are random. System identification is not just the choice when other alternatives are absent, it is superior to other methods in that it reveals the variation of transfer functions with frequency, which cannot easily be done otherwise.

Popular system identification techniques include Restoring Force Surface (RFS) (Masri et al., 1987), Nonlinear Auto-Regressive Moving Average with eXogenous inputs (NARMAX, see Leontaritis and Billings 1985), Hilbert transform (Feldman 1994) and Reverse-Multiple Input Single Output (R-MISO, see Bendat and Palo 1989, Bendat 1990, Palo et al. 1998, Bendat and Piersol 2011). Somayajula and Falzarano (2016) have

reviewed and discussed the advantages and limitations of these methods when applied to marine structures. The Marine Dynamics Laboratory (MDL) has studied the application of the R-MISO technique in naval architecture and ocean engineering problems (Falzarano et al., 2004, Somayajula and Falzarano 2016, Somayajula and Falzarano 2017).

The dimensions and geometry of the FPS are similar to a point absorber type WEC, which is believed to be the most typical WEC form. Therefore, the model test results of the FPS has been used to explore the applicability of the system identification method in this dissertation. The FPS has been tested in irregular (random) waves that were determined according to the sea state records of Galway Bay in Ireland. The wave time series measured in the model test were input to SIMDYN to make an "apples-to-apples" comparison between the simulated motions and the measured motions. All the model tests data are open access from Beaufort Research and HMRC based in Cork, Ireland (Bosma et al., 2014). As the system identification method is general, it is expected to be applicable to many other WESs.

With the two problems in WES modelling (nonlinear effects and viscous damping) better addressed, many quantities of interest (QOI) can be studied. The common QOIs (DNV, 2010) are: motions (e.g. roll and pitch are important to the dynamic stability); local loads (e.g. the connecting structure between the controller module and the main frame is subject to shearing stress due to the local lateral accelerations); mooring loads (e.g. tension and offset). Though the local accelerations and the mooring loads (are the most common QOIs) can also be studied, usually extensive time domain simulations are required, which makes it similar to traditional design practice. Compared with those QOIs analyzed

extensively in the typical global performance analysis (frequency domain and time domain), the dynamic stability (capsizing dynamically) is given relatively less attention (Haslum et al., 1999).

When it comes to the stability issue, while the static stability of larger floating structures like semi-submersibles/spars has been regulated by the various classification societies, their dynamic stability is usually of less concerned about (Koo et al., 2004, Mao and Yang 2016). As any emerging type of structure with smaller dimensions, a wave energy converter may experience more severe dynamic instabilities (Tarrant and Meskell 2016, Giorgi and Ringwood 2018, Gomes et al., 2017, Palm et al., 2018, Kurniawan et al., 2019) than traditional offshore structures because WESs usually sustain larger motion amplitudes (relative to their dimensions). Actually, several model tests of point absorber type WECs (Payne et al., 2008, Sheng et al., 2012, Gomes et al., 2012) have observed instability phenomenon, which can induce unexpected roll/pitch capsizing.

As for a wave energy converter, the "head seas" situation (as shown in Figure 1.3) is usually of most concerned, since WESs have no forward speed. In the head seas, the first concern, is for its dynamic stability. That is the possibility of pitchpoling due to the direct wave excitation, though the parametric excitation may also lead to instability. Of all the existing WES designs, many are floating bodies and are of the cylindrical geometries (e.g. Wang and Falzarano 2017, Wang et al., 2017). Mooring systems are designed to maintain the position of WESs. In this study, the most common WES form, a moored floating cylindrical geometry, is used as a generic model. Figure 1.3 depicts a generic

point absorber type wave energy converter, for which the modelling and analysis are representative of the majority of WES designs.
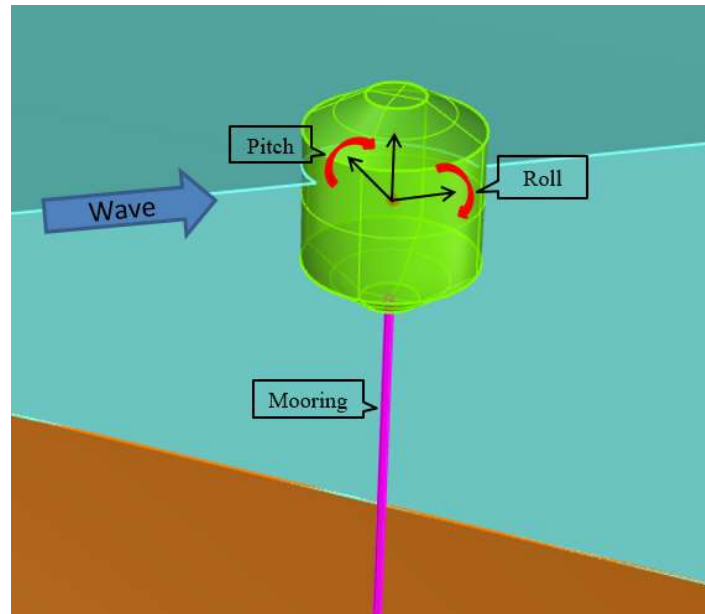


**Figure 1.3** Generic wave energy structure

Time domain analysis (see e.g. Somayajula and Falzarano 2015, Wang et al., 2020, Tarrant and Meskell 2016) seems to be a natural method for capsizing risk assessment. However, as it is very time consuming (Somayajula et al., 2019), time domain analysis is by its very nature inefficient in design. An alternative to time domain simulation is the Melnikov approach (Melnikov, 1963). It was initially applied by several researchers (e.g. Guckenheimer and Holmes 1984, Wiggins 2003) to analyze the nonlinear dynamics of mechanical oscillators. Falzarano (1990) was one of the first researchers to apply the Melnikov approach to study ship capsizing excited by regular beam seas. Frey and Simiu (1993) as well as Hsieh et al. (1994) extended this approach to systems under random

excitation by showing that the outflowing phase space flux from the safe region is related to the area enclosed by the non-negative Melnikov function. Therefore, an attempt will be made to apply the Melnikov approach to analyze the pitchpoling of a generic WES (with mooring).

The stability of the WES can alternatively be analyzed using the stochastic averaging method (see e.g. Su and Falzarano 2013). The system is averaged over the period of the unperturbed solution so that the energy of the system can be approximated as a Markov process (this approach is called the Markov approach). The mean first passage (failure) time of a Markov process can be numerically found by solving a set of differential equations. Using this approach, researchers have analyzed ship rolling under either random direct excitation (Su 2012, Su and Falzarano 2013) in beam seas or random parametric excitation in head seas (Somayajula and Falzarano 2019, Somayajula et al., 2019). The Markov approach generally has shown good agreement with the Melnikov approach on the ship rolling problem, although different parameters influence the comparison (Su, 2012, Somayajula 2017). It will be attempted as another method to analyze the pitchpoling of a generic WES (with mooring).

The dissertation is organized as follows. Section 2 covers the improvement of a blended time domain program for the motion predictions of a wave energy structure, benchmarked with model test results. Section 3 explores the application of system identification technique in model tests correlations of a realistic wave energy structure under random sea states, which can be used to correct the viscous damping. Section 4 studies the pitchpoling vulnerability of a typical wave energy structure geometry based on

Melnikov and Markov approaches. Section 5 summarizes the conclusions and discusses about future research directions. The format of the dissertation closely follows what has already been described in three journal papers (section 2: Wang et al. 2020b, published with Journal of Marine Science and Engineering; section 3: Wang et al. 2020a, published with Applied Ocean Research; section 4: a manuscript authored by Wang and Falzarano, submitted to Ships and Offshore Structures is in the final stages of review and acceptance).

# 2. DEVELOPMENT OF A BLENDED TIME-DOMAIN PROGRAM FOR PREDICTING THE MOTIONS OF A WAVE ENERGY STRUCTURE

## 2.1. Introduction

In designing a WES, predicting the motions is important and other quantities (e.g. mooring loads) are usually closely correlated with the motions. The significant problem in WES modelling (pointed out by the ECMW) is that WESs are usually subject to larger motion amplitudes (relative to their dimensions), therefore nonlinear effects become more important. After comparing existing hydrodynamic modelling methods, it's observed that the blended time domain method can be a time-efficient approach to address the nonlinear effects (although not all of them, though). This section discusses the development of such a time domain program (SIMDYN) capable of modelling realistic WES (six-degree of freedom, with an attached mooring system) while accounting for nonlinear effects.

SIMDYN was originally developed to simulate time domain ship motions (non-linearly). Usually those simulations involve roll motion only. Sometimes those simulations will couple with limited degrees of freedom (e.g. sway, heave and roll only). The author first added an interface to allow SIMDYN to couple with the open-source Mooring Analysis Program, MAP++ (MAP++ Documentation 2019). After implementing other forces as necessary (e.g. the drift forces), SIMDYN became capable of simulating

---

the WES motions, which have six degrees of freedom. "Other forces" include slowly varying wave drift forces and Morison element forces etc.

More importantly, SIMDYN was improved so that it can more accurately account for the nonlinear effects in Froude-Krylov forces, hydrostatic forces, and inertia forces. Available open source model test data has enabled us to examine and improve the accuracy of the simulation program. In 2014, the Beaufort Research and Hydraulics and Maritime Research Centre (HMRC) conducted model tests on a floating power system (FPS). The FPS was used in the model test correlation because suitable (and accessible) model test data was very limited. In fact, the geometry and dimensions of the floating power system are similar to a point absorber. Designed to provide power and connection to the grid (Bosma et al., 2014), the FPS is a necessary unit in wave energy conversion, but it is not a wave energy converter (WEC). That is the reason why the more general term "WES" is used to refer to it.

The FPS did not generate electricity in the model tests, thus reducing uncertainty and making it a perfect benchmark model for the study herein. Therefore, the motions of the FPS under the sea states tested in the experiments were simulated in SIMDYN to verify the accuracy of the program. Since the blended time domain method and the program are general they should be applicable to different types of WESs (e.g. the oscillating water column, the point absorber). The rest of the section is organized as follows. Subsection 2.2 gives the mathematical model of SIMDYN, including formulating the nonlinear equations of motion and the external forces. Subsection 2.3 discusses the nonlinear effects of Froude-Krylov and hydrostatic forces through a series of forced motion analyses.

Subsection 2.4 details the nonlinear inertia forces due to a large-angle of rotations and discusses their significance. Subsection 2.5 presents the model test correlations with the simulations for the regular wave cases. Subsection 2.6 is the discussion about the results.

## 2.2. Mathematical Model Description

### 2.2.1. Coordinate systems

To describe rigid body motions conveniently, two right-handed coordinate systems were used. The global coordinate system (GCS) is fixed to the earth (see Figure 2.1); a point in the GCS is $x = (x, y, z)$. The local coordinate system (LCS) translates and rotates with the rigid body; a point in the LCS is $x' = (x', y', z')$.
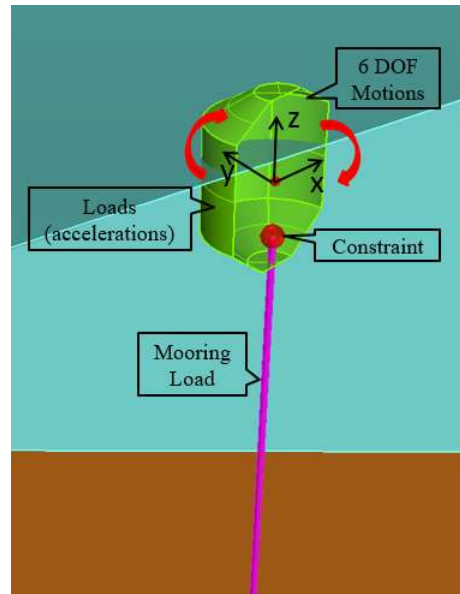


**Figure 2.1** Generic wave energy structure

The vector $\xi = (\xi_1, \xi_2, \xi_3)$ represents the translation from the GCS origin $(0,0,0)$ at the calm water line to the LCS origin $(\xi_1, \xi_2, \xi_3)$. The rotation vector $\alpha = (\xi_4, \xi_5, \xi_6)$

consists of the Euler angles between the GCS and the LCS. The coordinates in the LCS, $x'$, are related to the coordinates in the GCS, $x$, through rotation matrix $R$:

$$x' = R(x - \xi), \quad R = \begin{bmatrix} c_5 c_6 & (c_4 s_6 + s_4 s_5 c_6) & (s_4 c_6 - c_4 s_5 c_6) \\ -c_5 s_6 & (c_4 c_6 - s_4 s_5 s_6) & (s_4 c_6 + c_4 s_5 s_6) \\ s_5 & -s_4 c_5 & c_4 c_5 \end{bmatrix} \quad (2.1)$$

In equation 2.1, $c_i$ represents $cos(\xi_i)$, and $s_i$ represents $sin(\xi_i)$. In SIMDYN, the order of rotation used was roll first, then pitch, and then yaw. This is the convention specified by Ogilvie (1983). The angular velocity in the GCS is $\omega = R^T \omega'$, where $\omega'$ is the angular velocity in the LCS. In the matrix form, the angular velocity is:

$$\omega = \begin{bmatrix} 1 & 0 & s_5 \\ 0 & c_4 & s_4 c_5 \\ 0 & s_4 & c_4 c_5 \end{bmatrix} \begin{Bmatrix} \dot{\alpha}_1 \\ \dot{\alpha}_2 \\ \dot{\alpha}_3 \end{Bmatrix} = Q\dot{\alpha} \quad \omega' = \begin{bmatrix} c_5 c_6 & s_6 & 0 \\ -c_5 s_6 & c_6 & 0 \\ s_5 & 0 & 1 \end{bmatrix} \begin{Bmatrix} \dot{\alpha}_1 \\ \dot{\alpha}_2 \\ \dot{\alpha}_3 \end{Bmatrix} = P\dot{\alpha} \quad (2.2)$$

## 2.2.2. Governing equations

The blended time-domain method is based on the nonlinear equations of motion. The exact equations of motion are as (Somayajula and Falzarano 2015):

$$\begin{cases} m\left[\ddot{\xi} + \dot{\omega} \times (x_G - \xi) + \omega \times [\omega \times (x_G - \xi)]\right] = F \\ I\dot{\omega}' + \omega' \times I\omega' = R[M - x_G \times F] \end{cases} \quad (2.3)$$

Where $m$ is the mass, and $I$ is the mass moment of inertia with respect to the center of gravity. $\dot{\xi}$ is the time derivative and $\ddot{\xi}$ is the second time derivative. The force in equation 2.3 is applied at the center of gravity of the rigid body. The moment in equation 2.3 is referred to the center of gravity of the rigid body in the LCS. The left sides of equation 2.3 are the inertia forces. The right sides of equation 2.3 are external forces $F$ (force at center of gravity, in the GCS) and moments $M$ (moment with respect to the LCS origin, in the GCS):

18

$$[F, M]^T = F_{FK} + F_{dif} + F_{rad} + F_{vis} + F_{hyd} + F_{mor} + F_{me} + F_{PTO} + F_{sv} \quad (2.4)$$

WEC-Sim is a specific wave energy converter simulator developed by the Sandia National Laboratory and the National Renewable Energy Laboratory (WEC-Sim Documentation, 2019). Compared to WEC-Sim, SIMDYN includes an additional force: i.e., the slowly varying drift forces $F_{sv}$ (used under the linear time domain option). The other forces are Froude-Krylov forces ($F_{FK}$), diffraction forces ($F_{dif}$), radiation forces ($F_{rad}$), viscous forces ($F_{vis}$), hydrostatic forces ($F_{hyd}$), forces from the mooring system ($F_{mor}$), Morison element forces ($F_{me}$), and power take-off (PTO) forces ($F_{PTO}$).

Equation 2.4 includes the power take-off term to demonstrate the program completely. However, in the simulations performed, the PTO modelling is not used. This is because the floating power system in the model tests had no PTO, which helps reduce the difficulty of model test correlations. The viscous forces, radiation forces, diffraction forces, and Morison forces can be calculated in the usual way adopted by any time domain program (e.g., ANSYS Inc. 2011).

**Table 2.1** Comparison of time domain programs

| Code Name | AQWA | WaveDyn | WEC-Sim | SIMDYN |
|---|---|---|---|---|
| Developer | ANSYS Inc. | DNV GL | SNL & NREL | MDL |
| Froude-Krylov | Linear, Nonlinear | Linear, Nonlinear | Linear, Nonlinear | Linear, Nonlinear |
| Hydrostatics | Linear, Nonlinear | Linear, Nonlinear | Linear, Nonlinear | Linear, Nonlinear |

**Table 2.2** Continued

| Code Name | AQWA | WaveDyn | WEC-Sim | SIMDYN |
|---|---|---|---|---|
| Inertia Forces | Linear | Linear | Linear | Nonlinear |
| Drift Forces | Full QTF | N/A | N/A | Full QTF |
| License | Commercial | Commercial | Open-Source | Research |

Table 2.1 compares several programs on how the important forces are calculated. Compared to other programs, the nonlinear inertia forces are not applied in other programs shown in Table 2.1. The drift forces are not applied in other programs except in the commercial software AQWA.

**2.2.3. Mooring forces/moments**

Mooring in SIMDYN is modeled by coupling with the open-source quasi-static Mooring Analysis Program (MAP++). MAP++ ignores the inertia forces of the mooring lines and the fluid drag forces on the mooring lines (Masciola et al., 2013). Figure 2.2 shows how MAP++ is coupled with SIMDYN.
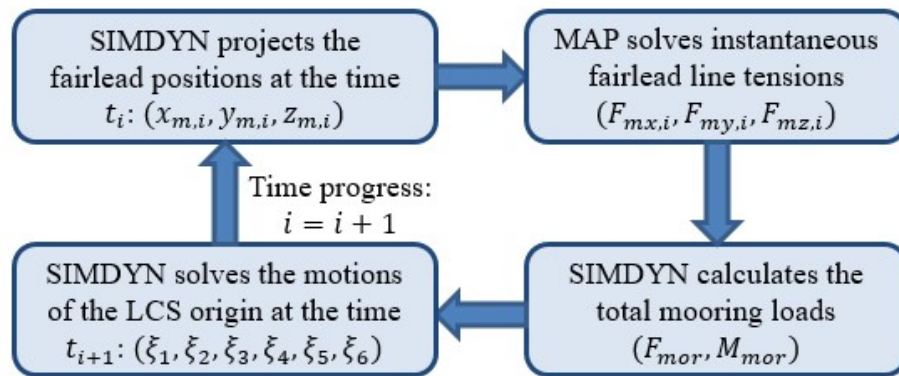


**Figure 2.2** Coupling of SIMDYN and MAP++

$(F_{mx,i},\ F_{my,i}, F_{mz,i})$ denotes the instantaneous fairlead translation forces of mooring line number $i$. The fairlead position of mooring line number $i$, $(x_{m,i},\ y_{m,i},\ z_{m,i})$, is projected from the origin of the body coordinate system, $(\xi_1, \xi_2, \xi_3)$.

### 2.2.4. Slowly varying drift forces/moments

Slowly varying drift forces will affect WES responses under irregular waves. Therefore, when the (linear) time domain option is used, SIMDYN calculates the drift forces. In this study, the quadratic transfer functions were output from the Marine Dynamic Laboratory's frequency domain hydrodynamic analysis program, MDL-HYDROD. Details on how quadratic transfer functions (QTFs) are evaluated can be found in previous work (Somayajula and Falzarano, 2017; Xie et al., 2019). Figure 2.3 show the (difference frequency) quadratic transfer functions for surge and pitch.
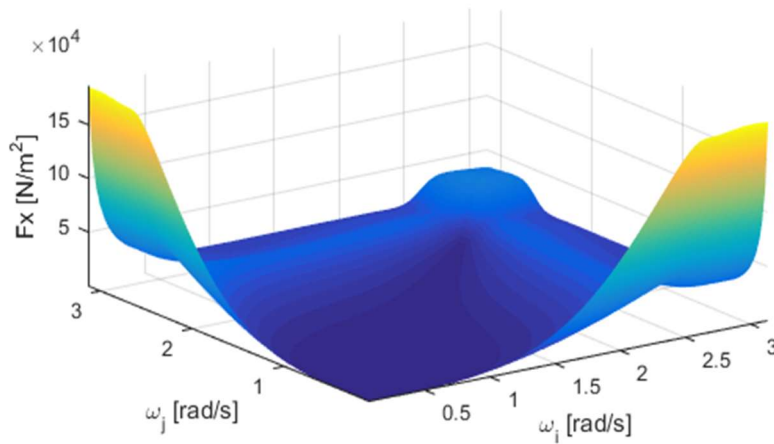


(a) Surge QTF

**Figure 2.3** (a) Surge QTF; (b) pitch QTF

21
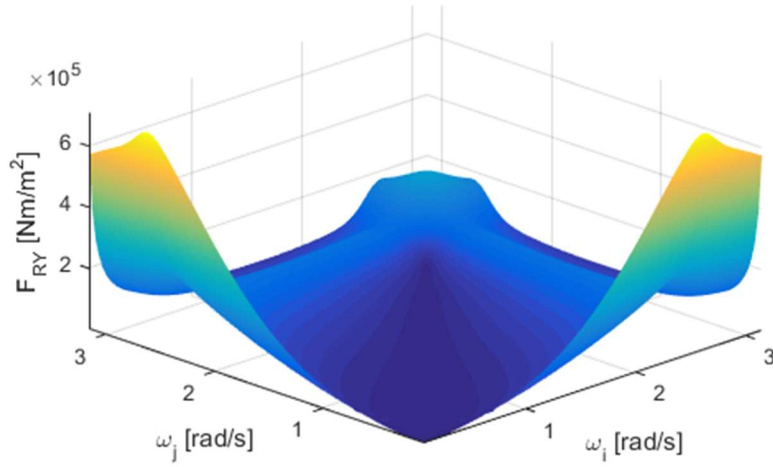
(b) pitch QTF

**Figure 2.4** Continued

If the random incident wave is decomposed as:

$$\eta = \sum_{i=1}^{NF} a_i \cos(\omega_i t + \epsilon_i) \tag{2.5}$$

The corresponding slowly varying wave drift force are (see ANSYS Inc. 2011):

$$F_{sv}(t) = \sum_{i=1}^{NF} \sum_{j=1}^{NF} [a_i a_j P_{ij}^- \cos(-\omega^- t + \epsilon^-) + a_i a_j Q_{ij}^- \sin(-\omega^- t + \epsilon^-)] \tag{2.6}$$

$a_i, a_j$ are the amplitude of the wave components with the frequency $\omega_i$ and $\omega_j$ and the phase $\epsilon_i$ and $\epsilon_j$. $\omega^- = \omega_i - \omega_j$, $\epsilon^- = \epsilon_i - \epsilon_j$. $NF$ is the number of frequencies used to define the frequency range. $P_{ij}^-$ are the in-phase components of the quadratic transfer function for the difference frequency $\omega^-$. $Q_{ij}^-$ are the out-of-phase components of the quadratic transfer function for difference frequency $\omega^-$. The sum frequency

22

components in the drift forces are neglected in equation because their contributions are usually much smaller than the difference frequency components.

## 2.2.5. Viscous forces/moments

There are two terms related to viscous drag: $\boldsymbol{F_{vis}}$ and $\boldsymbol{F_{me}}$. Either of them can be used in SIMDYN. The viscous forces $\boldsymbol{F_{vis}}$ can be calculated using the linearized (equivalent) damping coefficient $B_{eq}$:

$$F_{vis} = -B_{eq}\dot{\xi}_J(t) \tag{2.7}$$

Alternatively, the viscous forces can be modeled in the quadratic form of:

$$F_D = -\frac{1}{2}C_{dv}\dot{\xi}_J(t)\left|\dot{\xi}_J(t)\right| \tag{2.8}$$

$C_{dv}$ are the quadratic damping coefficients and $\dot{\xi}_J$ is the jth degree of freedom velocity. The drag coefficients should be determined by model tests correlations (e.g. free decay tests) or empirical formula. Practically, the user should input the degrees of freedom to which the damping values apply as well as the corresponding damping values. For example:

*external_damping 4 1 4E4  → a linear viscous rolling damping of $4{\times}10^4$ Ns/m is applied.

*quadratic_damping 1 2 2E3 → a quadratic viscous surge damping of $2{\times}10^3$ Ns$^2$/m$^2$ is applied.

## 2.3. Nonlinear Froude-Krylov and Hydrostatic Forces

## 2.3.1. Formulation of nonlinear Froude-Krylov and hydrostatic forces

In the blended time domain method, the Froude-Krylov forces are calculated by integrating the nonlinear dynamic pressure over the instantaneous wetted surface of the rigid body (Penalba et al., 2017). In this way, the method accounts for the effects of the instantaneous body motions and the instantaneous incident wave. Linear incident wave potential at point $(x, y, z)$ in the GCS due to a unidirectional irregular sea incident at counterclockwise angle $\beta$ to the body's longitudinal axis is given by the following:

$$\phi_I = \sum_{i=1}^{NF} -\frac{H_i g}{2\omega_i} \cdot \frac{cosh[k_i(h + zw)]}{cosh(k_i h)} sin[k_i(xcos\beta + ysin\beta) - \omega_i t] \qquad (2.9)$$

For the wave frequency component $i$, $H_i$ is the wave height, $\omega_i$ is the frequency, $k_i$ is the wave number, $h$ is the water depth, and $NF$ is the total number of wave frequencies. The linear incident wave potential is not defined for the points above the mean water line($z = 0$). SIMDYN employs Wheeler stretching (1970) to extrapolate the incident and hydrostatic pressure profiles to provide an expression for pressure inside the incident wave crest (OrcaFlex Documentation 2019, Giorgi and Ringwood 2019).

The Wheeler stretching is a usual way of extrapolating the incident wave pressure above the mean water level in calculating the nonlinear Froude-Krylov forces. Its accuracy has been benchmarked for ships (Du et al. 2009) and for wave energy converters (Giorgi and Ringwood 2017) and is assumed to be appropriate in this study. Mathematically, this can be considered as scaling the z-coordinate to compute pressure up to instantaneous free surface elevation $\eta$ (measured from the calm water plane) due to the incident wave (OrcaFlex Documentation 2019, Giorgi and Ringwood 2019). Vertical coordinate $z$ is modified to $zw$ through Wheeler stretching:

$$zw = \frac{h}{h + \eta(t, x, y)} [z - \eta(t, x, y)] \qquad (2.10)$$

Dynamic pressure $p$ is as follows:

$$p(t, x, y, zw) = -\rho \frac{\partial \phi_I}{\partial t}(t, x, y, zw) - \frac{\rho}{2} |\nabla \phi_I(t, x, y, zw)|^2 \qquad (2.11)$$

The dynamic pressure $-\frac{\rho}{2} |\nabla \phi_I(t, x, y, zw)|^2$ is also nonlinear. The surface panels

of the rigid body satisfying condition $z \le \eta(t, x, y)$ form instantaneous wetted panels $P_B$.

The Froude-Krylov forces/moments are as follows:

$$\boldsymbol{F_{FK}} = \iint_{P_B} p(t, x, y, zw) \cdot \boldsymbol{n} dS, \quad \boldsymbol{M_{FK}} = \iint_{P_B} p(t, x, y, zw) \cdot (\boldsymbol{x} \times \boldsymbol{n}) dS \quad (2.12)$$

$\boldsymbol{n}$ is the normal vector of the panel, and $\boldsymbol{x}$ is the position vector of the wetted panel

centroid (in the GCS). SIMDYN integrates the results of a pre-processed potential

problem solved under linear conditions

Similar to the Froude-Krylov forces, the blended time domain method calculates

the hydrostatic forces and moments by integrating the hydrostatic pressure over the

instantaneous wetted surface area (Lawson et al., 2014):

$$\begin{cases} \boldsymbol{F_{hyd}} = -mg\widehat{\boldsymbol{k}} + \iint_{P_B} -\rho gz \cdot \boldsymbol{n} dS \\ \boldsymbol{M_{hyd}} = -\boldsymbol{x_G} \times (mg\widehat{\boldsymbol{k}}) + \iint_{P_B} -\rho gz \cdot (\boldsymbol{x} \times \boldsymbol{n}) dS \end{cases} \qquad (2.13)$$

Where $-mg\widehat{\boldsymbol{k}}$ is the rigid body weight vector, and $P_B$ are the instantaneous wetted

panels satisfying $z \le \eta(t, x, y)$. Note that the hydrostatic pressure, $-\rho g\boldsymbol{z}$, is calculated

using the actual vertical coordinate $z$ instead of $zw$. In this way, equations 2.12 and 2.13

satisfy the dynamic free-surface boundary condition.

## 2.3.2. Nonlinear effects of Froude-Krylov and hydrostatic forces
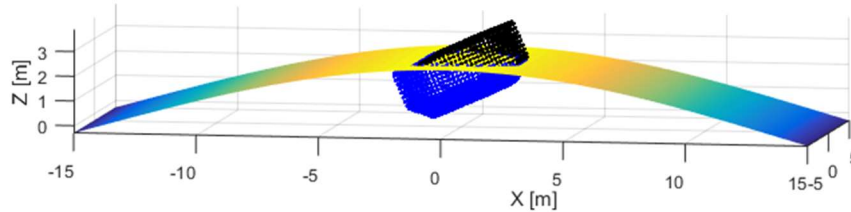


**Figure 2.5** Geometry of a floating power system

This subsection presents the nonlinear effects through the forced motion tests. The forced motion tests are important because:

- The forced motion tests shows the effect of different forcing corresponding to the same motions. Therefore, in an implicit way, they indicate the motion (as the final result) differences between the linear and the blended method;

- The forced motion test is a control-variable test. It eliminates the effects of other forces, which makes the effect from each force component clearer.

- Any simulation tool comes with limitations. The forced motion test can disable modules not robust enough and not very relevant (for example, the mooring module is not the focus of this study);

The geometry used in these tests is the floating power system as plotted in Figure 2.4. The forced motion tests refer to a series of SIMDYN simulations that use the specified (forced) motion time series to study a force component (e.g., Froude-Krylov). In these tests, SIMDYN generates the same incident wave for the linear time domain simulation

and the blended time domain simulation. This practice ensures that the body motions and wave elevations in the two types of simulations at any time instant are identical. The only variable in the forced motion tests is the method (linear or nonlinear) of calculating the Froude-Krylov and hydrostatic forces.

It should be noted that in this study, the mesh on the FPS geometry is not remeshed at each time step. A panel is either fully submerged or fully emerged by whether the instantaneous centroid of the panel is above/below the free surface. In this case, the mesh number is enough for the output to be stable: more panels significantly increases the computational time without noticeable accuracy improvements. The integration could be improved by re-meshing the geometry in every time step, as conducted by Jang and Kim (2019, 2020).

The body motions (from the linear time-domain simulation) under a regular wave of $H = 1m, T = 7.0s$ are recorded as the reference motions $(M1)$ and the forced motions were set at five times the reference motions $(5 \times M1)$. The study used a (large-amplitude) regular wave of $H = 5m, T = 7.0s$, Note that the motions in the forced motion tests were not simulated but were specified (as input). This is a quite extreme condition (large wave and motions) for the FPS; therefore, nonlinear effects could be observed clearly.

Figure 2.5 compares the Froude-Krylov and hydrostatic heave forces (when $H = 5m, T = 7.0s$, motions $5 \times M1$).
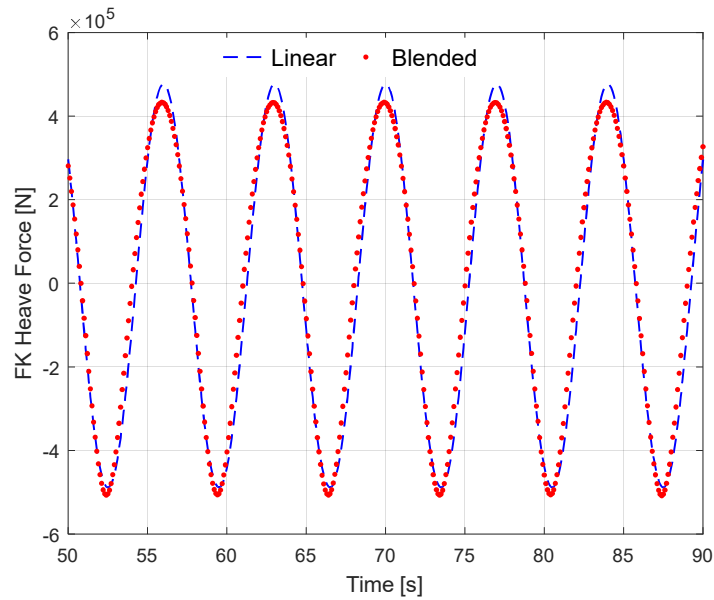
(a) Froude-Krylov
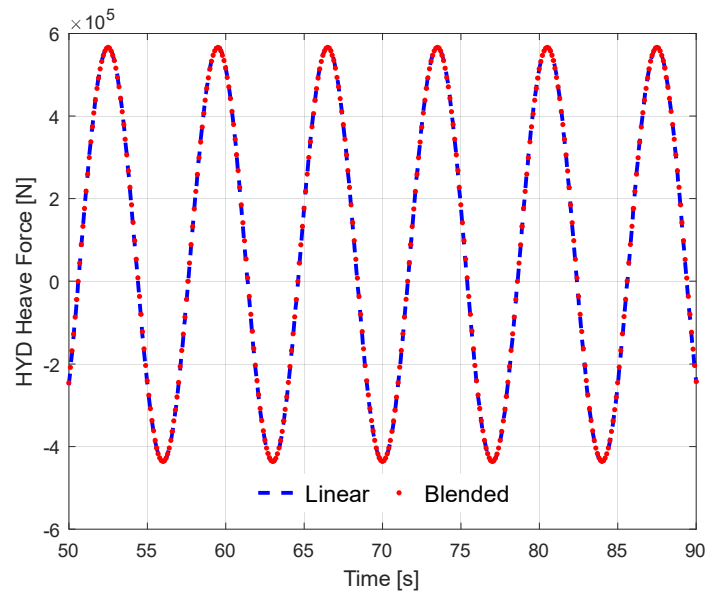


(b) hydrostatic

**Figure 2.6** Heave forces: (a) Froude-Krylov; (b) hydrostatic

In Figure 2.5, the hydrostatic heave forces using the two methods are very close, while the Froude-Krylov heave forces show slight differences.

28
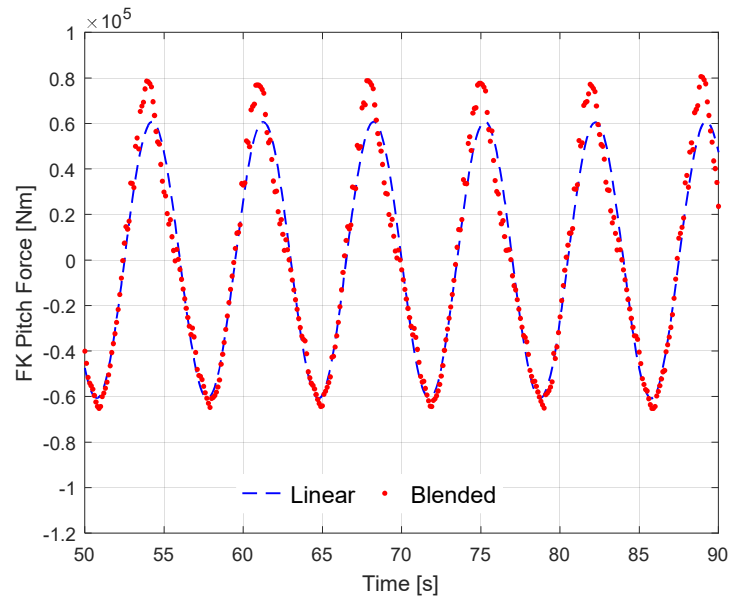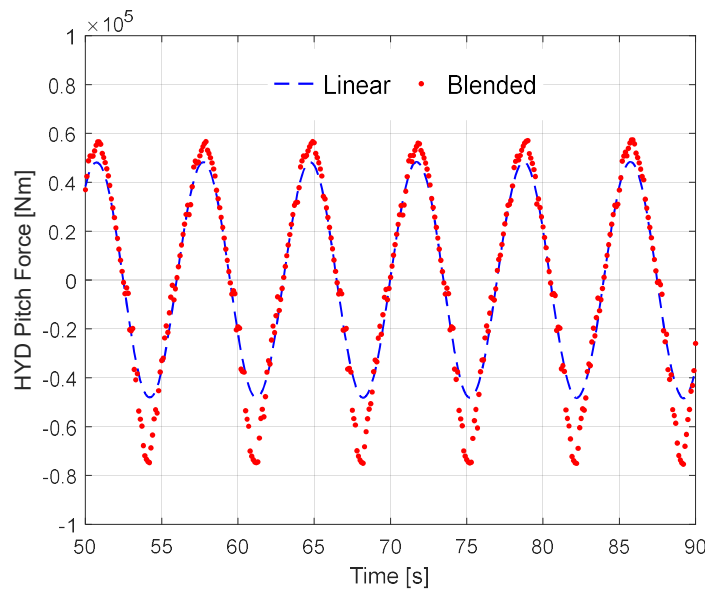
(a) Froude-Krylov



(b) hydrostatic

**Figure 2.7** Pitch moments: (a) Froude-Krylov;  (b) hydrostatic

Figure 2.6 compares the Froude-Krylov and hydrostatic pitch moments (when $H = 5m, T = 7.0s$, motions $5 \times M1$). The Froude-Krylov and hydrostatic pitch moments show

significant relevance to the nonlinear effects: as the wave and motion amplitude increase, the heave force and pitch moment become more and more relevant to the nonlinear effects.

Figure 2.7 compares different sets of assumption applied in the nonlinear method (upper) with the linear method (lower). The model in the two methods are subject to the same regular wave of $H = 2.0m, T = 6.0s$.
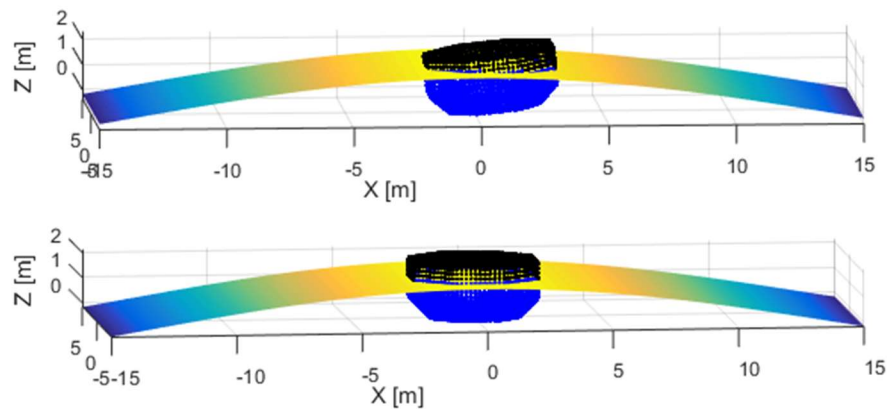


**Figure 2.8** FPS modelling (upper: blended; lower: linear)

From Figure 2.7, the following can be found:

1. The instantaneous rotations of the structure are not addressed in the linear modelling, so the wetted surfaces and the corresponding pressures are different.

2. The instantaneous rotations of the structure are not addressed in the linear modelling, so the normal direction variation of each panel is not captured.

3. The translational motions of the structure are not captured in the linear method, so the wetted surfaces and the corresponding pressures are different. Note that the

surge and sway influence the relative phase of the incident wave, so they also

contribute to the differences.

## 2.4. Nonlinear Inertia Forces

### 2.4.1. Derivations of the nonlinear inertia forces

For an irregular wave, the radiation forces are as follows (Cummins 1962):

$$\{\boldsymbol{F_{rad}}\} = -[A(\infty)]\{\ddot{\xi}\} - \int_0^\infty [h(\tau)]\{\dot{\xi}(t-\tau)\}d\tau \qquad (2.14)$$

$[A(\infty)]$ is the $6 \times 6$ added mass matrix at infinite frequency. It can be written as

following:

$$[A(\infty)] = \begin{bmatrix} A_{11}^{3\times3} & A_{12}^{3\times3} \\ A_{21}^{3\times3} & A_{22}^{3\times3} \end{bmatrix} \qquad (2.15)$$

$A_{11}^{3\times3}$, $A_{12}^{3\times3}$, $A_{21}^{3\times3}$, and $A_{22}^{3\times3}$ represent the four $3 \times 3$ blocks of the $6 \times 6$ added

mass matrix $[A(\infty)]$, and $[h(\tau)]$ is the $6 \times 6$ retardation function matrix corresponding to

the frequency-dependent radiation damping. Note that in the blended time domain method,

acceleration term $-[A(\infty)]\{\ddot{\xi}\}$ in equation 2.14 should be moved to the left side of

equation 2.3. The equations of motion become the following:

$$\begin{cases} m\{\ddot{\xi} + \dot{\omega} \times (x_G - \xi) + \omega \times [\omega \times (x_G - \xi)]\} + A_{11}^{3\times3}\ddot{\xi} + A_{12}^{3\times3}\ddot{\alpha} = F \\ I\dot{\omega}' + \omega' \times I\omega' + A_{21}^{3\times3}\ddot{\xi} + A_{22}^{3\times3}\ddot{\alpha} = R[M - x_G \times F] \end{cases} \qquad (2.16)$$

Angular velocities $\omega'$ and $\omega$ defined in equation 2.2 can be expressed in matrix

form as shown below:

$$\boldsymbol{\omega} = Q\dot{\alpha}, \qquad \boldsymbol{\omega}' = P\dot{\alpha} \qquad (2.17)$$

Differentiating equation 2.17 with respect to time, the angular accelerations are

achieved ($\dot{\omega}'$ in the LCS, $\dot{\omega}$ in the GCS):

$$\dot{\omega} = Q\ddot{\alpha} + \dot{Q}\dot{\alpha}, \qquad \dot{\omega}' = P\ddot{\alpha} + \dot{P}\dot{\alpha} \tag{2.18}$$

Substituting equations 2.17 and 2.18 into equation 2.3 and rearranging to keep only the terms containing acceleration on the left side:

$$m\ddot{\xi} + A_{11}^{3\times3}\ddot{\xi} + mQ\ddot{\alpha} \times (x_G - \xi) + A_{12}^{3\times3}\ddot{\alpha}$$

$$= F - m\dot{Q}\dot{\alpha} \times (x_G - \xi) - m\omega \times [\omega \times (x_G - \xi)] \tag{2.19}$$

Substituting equations 2.17 to 2.19 into equation 2.16, yields the following:

$$IP\ddot{\alpha} + I\dot{P}\dot{\alpha} + A_{21}^{3\times3}\ddot{\xi}$$
$$+ A_{22}^{3\times3}\ddot{\alpha} + P\dot{\alpha} \times IP\dot{\alpha} =$$

$$RM - mRx_G \times (Q\ddot{\alpha} + \dot{Q}\dot{\alpha}) \times (x_G - \xi) \tag{2.20}$$
$$- R\{mx_G \times \ddot{\xi} + mx_G \times Q\dot{\alpha} \times [Q\dot{\alpha} \times (x_G - \xi)]\}$$
$$- R\{A_{11}^{3\times3}x_G \times \ddot{\xi} + A_{12}^{3\times3}x_G \times \ddot{\alpha}\}$$

Equations 2.19 and 2.20 are rearranged into the matrix form. Let $v$ denote a generic vector. Cross multiplication $x_G \times v$ can be written in the matrix form:

$$x_G \times v = \begin{bmatrix} 0 & -x_{G3} & x_{G2} \\ x_{G3} & 0 & -x_{G1} \\ -x_{G2} & x_{G1} & 0 \end{bmatrix} \begin{Bmatrix} v_1 \\ v_2 \\ v_3 \end{Bmatrix} = L_1(x_G)v \tag{2.21}$$

Similarly, cross multiplication $v \times (x_G - \xi)$ can be written in the matrix form:

$$v \times (x_G - \xi) = \begin{bmatrix} 0 & x_{G3} - \xi_3 & -(x_{G2} - \xi_2) \\ -(x_{G3} - \xi_3) & 0 & x_{G1} - \xi_1 \\ x_{G2} - \xi_2 & -(x_{G1} - \xi_1) & 0 \end{bmatrix} \begin{Bmatrix} v_1 \\ v_2 \\ v_3 \end{Bmatrix}$$

$$= L_2(x_G - \xi)v \tag{2.22}$$

Using equation 2.22, 2.19 can be written as follows:

$$m\ddot{\xi} + A_{11}^{3\times3}\ddot{\xi} + mL_2(x_G - \xi)Q\ddot{\alpha} + A_{12}^{3\times3}\ddot{\alpha}$$

$$= F - mL_2(x_G - \xi)\dot{Q}\dot{\alpha} - m\omega \times [L_2(x_G - \xi)\omega] \tag{2.23}$$

Substituting equations 2.21 and 2.22 into equation 2.20 and rearranging to keep only the terms containing acceleration on the left side results in the following:

$$mRL_1(\boldsymbol{x_G})\ddot{\boldsymbol{\xi}}+RA_{11}^{3\times3}L_1(\boldsymbol{x_G})\ddot{\boldsymbol{\xi}} + A_{21}^{3\times3}\ddot{\boldsymbol{\xi}} + IP\ddot{\boldsymbol{\alpha}} + mRL_1(\boldsymbol{x_G})L_2(\boldsymbol{x_G} - \boldsymbol{\xi})Q\ddot{\boldsymbol{\alpha}}$$
$$+A_{22}^{3\times3}\ddot{\boldsymbol{\alpha}} + RA_{12}^{3\times3}L_1(\boldsymbol{x_G})\ddot{\boldsymbol{\alpha}} = RM - mRL_1(\boldsymbol{x_G})L_2(\boldsymbol{x_G} - \boldsymbol{\xi})\dot{Q}\dot{\boldsymbol{\alpha}}$$
$$-mR\{L_1(\boldsymbol{x_G})Q\dot{\boldsymbol{\alpha}} \times [L_2(\boldsymbol{x_G} - \boldsymbol{\xi})Q\dot{\boldsymbol{\alpha}}]\} - P\dot{\boldsymbol{\alpha}} \times IP\dot{\boldsymbol{\alpha}} - I\dot{P}\dot{\boldsymbol{\alpha}} \qquad (2.24)$$

In the matrix form, equations 2.23 and 2.24 can be written as follows:

$$\begin{bmatrix} m + A_{11}^{3\times3} & mL_2(\boldsymbol{x_G} - \boldsymbol{\xi})Q + A_{12}^{3\times3} \\ mRL_1(\boldsymbol{x_G}) + RA_{11}^{3\times3}L_1(\boldsymbol{x_G}) + A_{21}^{3\times3} & IP + mRL_1(\boldsymbol{x_G})L_2(\boldsymbol{x_G} - \boldsymbol{\xi})Q+A_{22}^{3\times3} + RA_{12}^{3\times3}L_1(\boldsymbol{x_G}) \end{bmatrix}\begin{Bmatrix} \ddot{\boldsymbol{\xi}} \\ \ddot{\boldsymbol{\alpha}} \end{Bmatrix}$$
$$= \begin{Bmatrix} \boldsymbol{F} \\ RM - mRL_1(\boldsymbol{x_G})L_2(\boldsymbol{x_G} - \boldsymbol{\xi})\dot{Q}\dot{\boldsymbol{\alpha}} \\ -mL_2(\boldsymbol{x_G} - \boldsymbol{\xi})\dot{Q}\dot{\boldsymbol{\alpha}} \\ -mR\{L_1(\boldsymbol{x_G})Q\dot{\boldsymbol{\alpha}} \times [L_2(\boldsymbol{x_G} - \boldsymbol{\xi})Q\dot{\boldsymbol{\alpha}}]\} \\ -m\boldsymbol{\omega} \times [L_2(\boldsymbol{x_G} - \boldsymbol{\xi})\boldsymbol{\omega}] \\ -P\dot{\boldsymbol{\alpha}} \times IP\dot{\boldsymbol{\alpha}} - I\dot{P}\dot{\boldsymbol{\alpha}} \end{Bmatrix} \qquad (2.25)$$

Equation 2.25 is the nonlinear equation of motion used in SIMDYN. It is solved using the fourth-order Runge-Kutta method (Somayajula and Falzarano, 2015).

**2.4.2. Nonlinear effects of the inertia force**

This subsection presents the nonlinear effects of the inertia force (see Giorgi, and Ringwood, 2019; Tarrant and Meskell, 2016) through forced motion tests on the FPS geometry shown in Figure 2.4. In equation 2.16, all the nonlinear terms are related to rotations. Note that equation 2.16 includes the inertia forces due to the added masses on the left sides. Equation 2.16 can be rewritten as follows:

$$\begin{cases} \boldsymbol{F} = m\left[\ddot{\boldsymbol{\xi}} + \dot{\boldsymbol{\omega}} \times (\boldsymbol{x_G} - \boldsymbol{\xi}) + \boldsymbol{\omega} \times [\boldsymbol{\omega} \times (\boldsymbol{x_G} - \boldsymbol{\xi})]\right] + A_{11}^{3\times3}\ddot{\boldsymbol{\xi}} + A_{12}^{3\times3}\ddot{\boldsymbol{\alpha}} \\ \boldsymbol{M} = R^T\left(I\dot{\boldsymbol{\omega}}' + \boldsymbol{\omega}' \times I\boldsymbol{\omega}' + A_{21}^{3\times3}\ddot{\boldsymbol{\xi}} + A_{22}^{3\times3}\ddot{\boldsymbol{\alpha}}\right) + \boldsymbol{x_G} \times \boldsymbol{F} \end{cases} \qquad (2.26)$$

Using equation 2.26, nonlinear inertia forces $\boldsymbol{F}$ and moments $\boldsymbol{M}$ can be calculated. Note that in the linear time-domain method, the motions and rotations are assumed small:

$$x_G \approx x_G' , \omega \approx \omega' \approx \dot{\alpha}, \dot{\omega} \approx \dot{\omega}' \approx \ddot{\alpha} \qquad (2.27)$$

$x_G'$ are the coordinates of the center of gravity in the LCS, which is constant. Taking these assumptions to remove the nonlinear terms in equation 2.25, the following is obtain:

$$\begin{bmatrix} m + A_{11}^{3\times3} & mL_2(x_G') + A_{12}^{3\times3} \\ mL_1(x_G') + A_{21}^{3\times3} & I + mL_1(x_G')L_2(x_G') + A_{22}^{3\times3} \end{bmatrix} \begin{Bmatrix} \ddot{\xi} \\ \ddot{\alpha} \end{Bmatrix} = \begin{Bmatrix} F \\ M \end{Bmatrix} \qquad (2.28)$$

Note that the terms containing $L_1(x_G')$ and $L_2(x_G')$ convert momentum of inertia from the center of gravity to the origin of the LCS in the linear model, (0, 0, 0). This is the typical linear equation of motion. From equation 2.28, the linear inertia forces and moments can be calculated.

Using equations 2.26 and 2.28, the inertia forces in the forced motion tests (i.e., the time series of the motions, velocities, and accelerations are given) can be obtained. Note that the moments are given in the GCS from equations 2.26 and 2.28; therefore, the inertia moments from the blended time domain method should be transformed to the instantaneous origin of the body coordinate system, $(\xi_1, \xi_2, \xi_3)$, to be compared with those from the linear time-domain method.

In the forced motion tests, the translational motions were set to zero to reveal the nonlinear effects due to the rotation. The second set of forced motions of the FPS are quite mild, referred to as $M2$ (see Figure 2.8). $M2$ is specified to show the inertia force

differences (between the two options), so the relative phases of the rotations are not necessarily realistic.
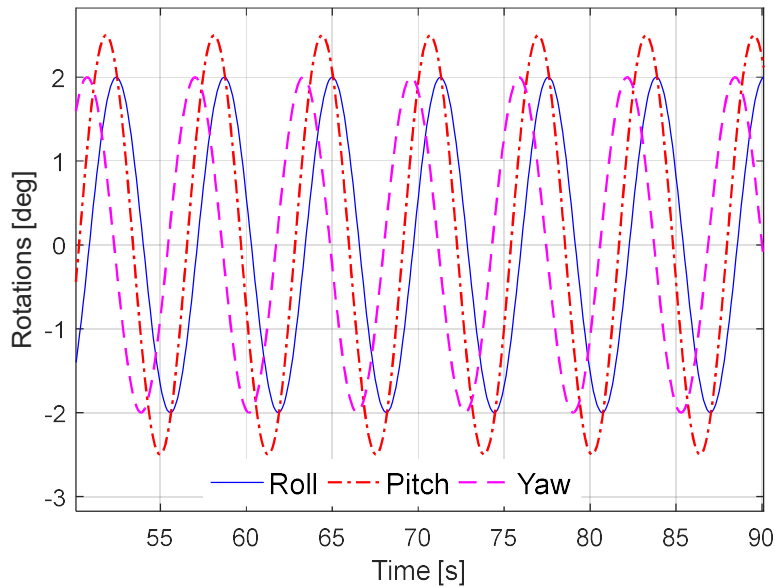


**Figure 2.9** Reference forced motions $M2$

The inertia forces corresponding to 10 times the reference motions, $10 \times M2$, are plotted in Figure 2.9. The surge and sway forces from the two methods are slightly different, indicating that the nonlinearity due to rotation is not significant for these rotation amplitudes.

The heave force from the blended model looks very different from the linear model, but bear in mind that when the actual heave motion is in place, the contribution from the heave motion itself is much greater (>1,000 times) than that from the rotations.
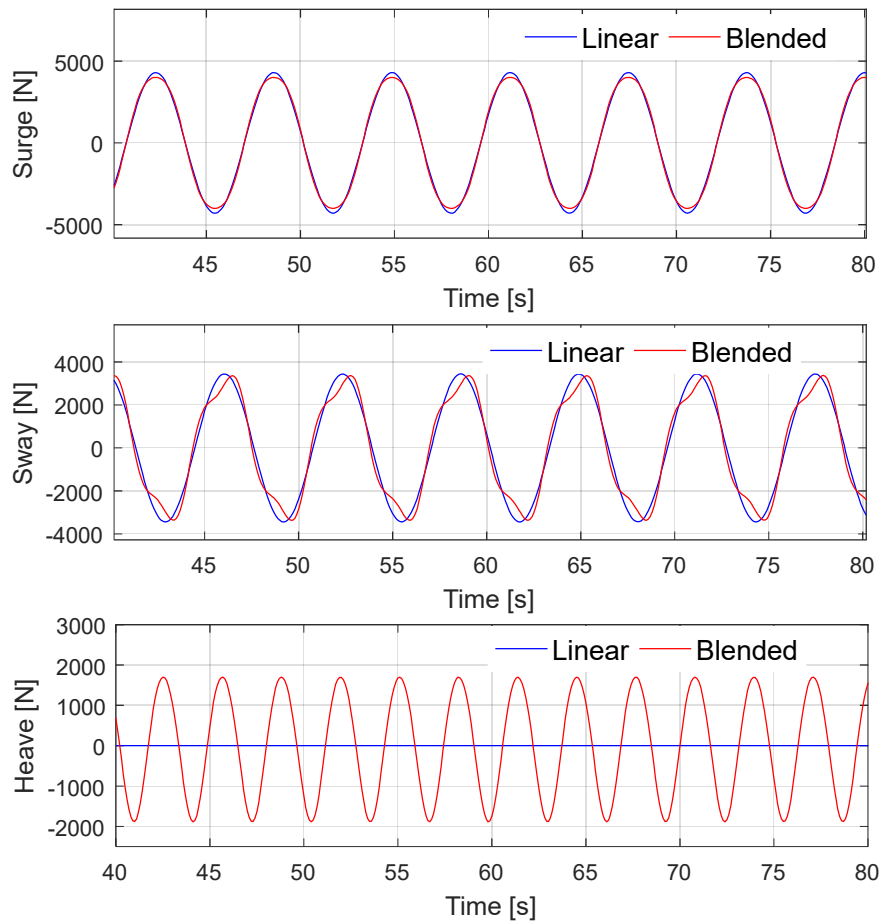
**Figure 2.10** Translation inertia forces corresponding to forced motion $10 \times M2$

Under the forced rotations, $10 \times M2$, the differences in roll and pitch moments between the linear model and the blended model are noticeable (see Figure 2.10). The significant difference of the yaw moments indicates that for yaw, in this case, the linear model is no longer valid.
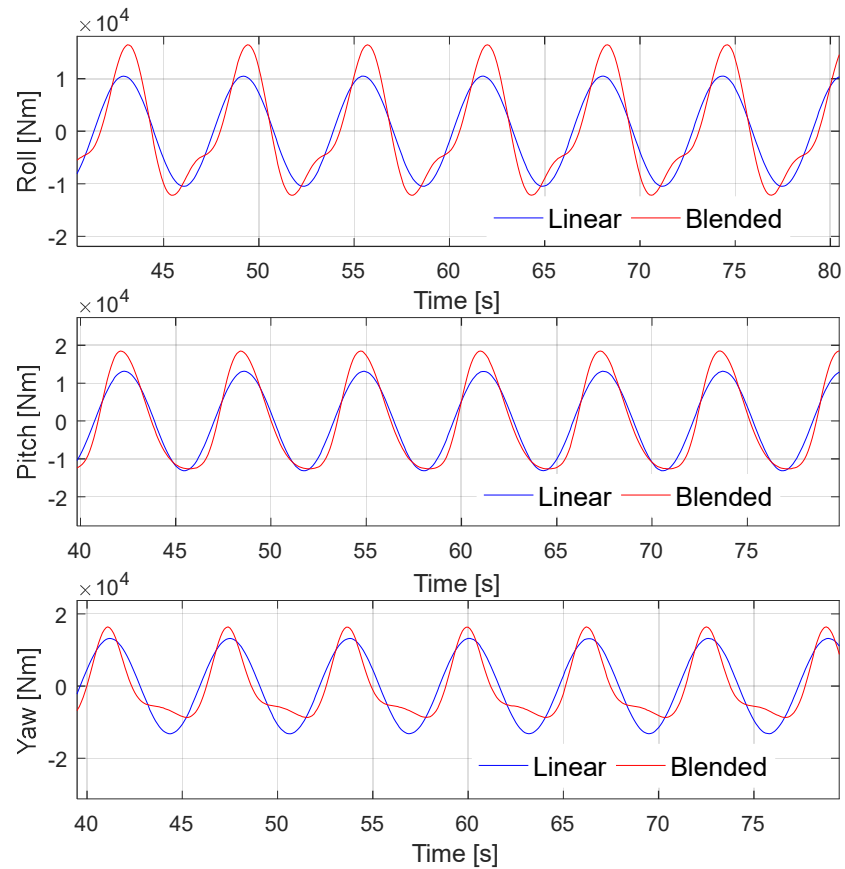
**Figure 2.11** Rotation inertia moments corresponding to forced motions $10 \times$
$M2$

The blended results contain higher (mostly double) frequency components in sway, heave, yaw and roll. They are the superharmonic components contributed by the nonlinear terms in the equation of motion. For example, in a case with zero yaw accelerations (an axisymmetric buoy), the combination of roll and pitch rotations will provide a nonlinear contribution to the yaw inertial forces using the nonlinear model.

## 2.5. Model Test Correlations

## 2.5.1. Model test setup and inputs

The blended time-domain program SIMDYN was examined using correlations with a series of 1:25-scale model tests (Bosma et al., 2014) performed by Beaufort Research/HMRC in Ireland. In these model tests, the incident wave headings included 0°, 30°, and 60°. The 0° wave heading test was selected as it consists of more sea states. The 0° wave test configuration is shown in Figure 2.11.
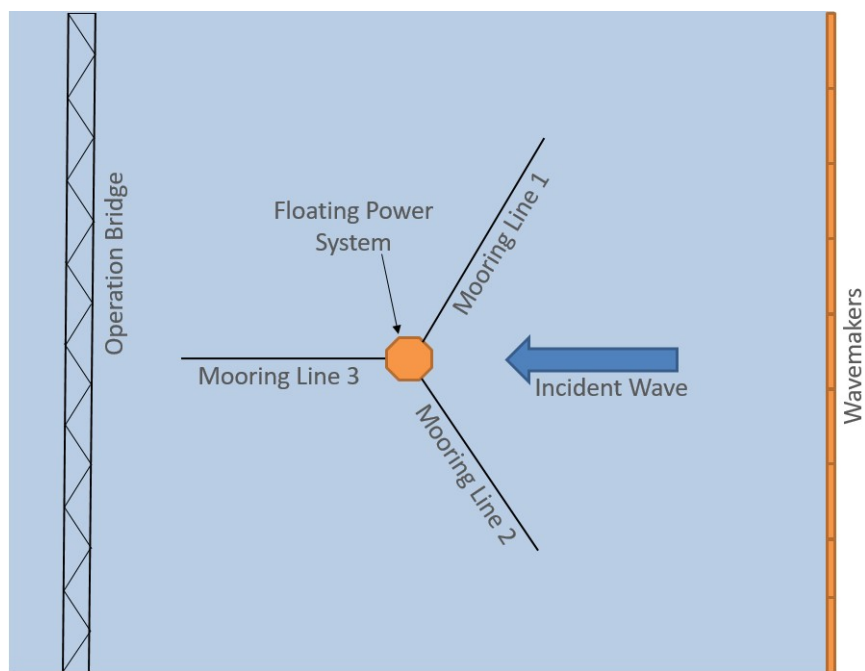


**Figure 2.12** 0° wave test by Bosma et al. (2014), adapted with permission

The 0° wave heading tests consisted of 34 regular wave cases. Some cases were skipped given indications of incomplete measurements or unexpectedly large roll and yaw measurements (which should not be the case, as the configuration is symmetric about the x-axis). The unexpectedly large roll and yaw measurements may be partially attributed to parametric instabilities, which many WECs suffer from (see Tarrant and Meskell 2016,

Babarit et al., 2009, Giorgi, and Ringwood 2018, Kurniawan et al., 2019, Palm et al., 2018, Gomes et al., 2017, Orszaghova et al., 2019). These dynamic instabilities deserve systematic studies in the future. The correlated sea states are plotted in Figure 2.12.
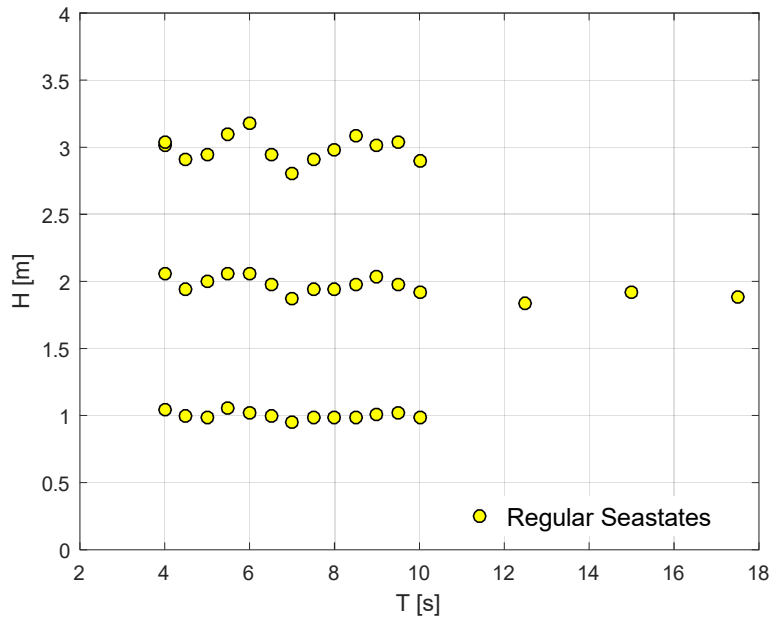


**Figure 2.13** Correlated sea states

MDL-HYDROD performed the frequency domain analysis. The added masses, the radiation dampings, the diffraction forces, and the QTFs necessary for the blended time-domain analysis were obtained. More details about MDL- HYDROD can be found in previous work (Guha 2016, Liu and Falzarano 2017).
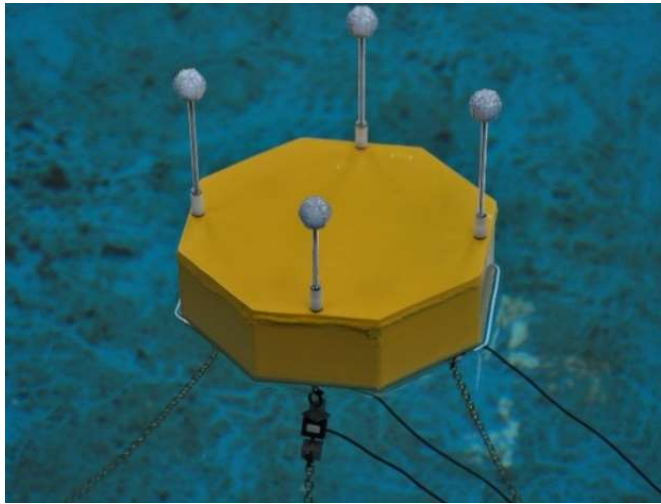
(a) floating power system tested by Bosma et al. (2014), reprinted with permission
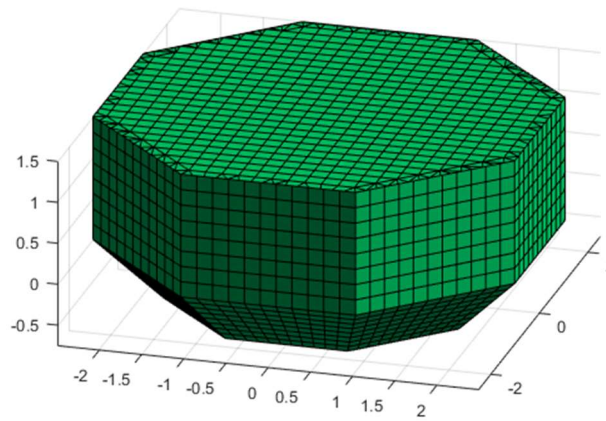


(b) floating power system (panel model) analyzed by the Marine Dynamic
Laboratory

**Figure 2.14** Floating power system models: (a) floating power system tested in
the wave basin (photo by the Beaufort Research/HMRC, with permission); (b)
floating power system (panel model) analyzed by the Marine Dynamic
Laboratory

Figure 2.13 (a) shows the 1:25-scale FPS model used in the wave basin (Bosma et

al., 2014). The FPS panel model in Figure 2.13 (b) was used in SIMDYN (for integration

of instantaneous pressure). The FPS has octagon cross section with decreasing cross section area below the calm water line. It consisted of 2,396 panels and the wetted surface was not re-meshed during the simulations. A panel is either fully submerged or fully emerged (by determining whether the instantaneous centroid of the panel is above/below the free surface). The FPS is positioned by a 3-leg catenary mooring system with 120-degree azimuth difference between each mooring leg.

Table 2.2 lists the inputs used in the model test correlations. *VCG* is the vertical center of gravity and it is measured from the calm water plane (instead of from the bottom of the body). *Kxx*, *Kyy* and *Kzz* are the gyration radius, around the center of gravity. *EA* is the mooring element axial stiffness.

**Table 2.3** Floating power system information

| Characteristic | Value | Characteristic | Value |
|---|---|---|---|
| Mass *M* (kg) | 11,337.9 | Anchor Ver. Position (m) | –25.0 |
| Length *Lpp* (m) | 5.00 | Anchor Hor. Position (m) | 65.0 |
| Breadth *B* (m) | 5.00 | Mooring Line Length (m) | 75.0 |
| Height *D* (m) | 2.25 | Mass/Unit Length (kg/m) | 28.438 |
| *VCG* (m) | 0.64 | Mooring Line Diameter (m) | 0.15 |
| *Kxx* (m) | 1.386 | Added Mass Coefficient | 1.0 |
| *Kyy* (m) | 1.386 | Trans. Drag Coefficient | 1.0 |
| *Kzz* (m) | 1.821 | Longi. Drag Coefficient | 0.025 |
| Draft *T* (m) | 0.75 | *EA* (N/m) | $1.0 \times 10^8$ |

**Table 2.4** Continued

| Characteristic | Value | Characteristic | Value |
|---|---|---|---|
| Water Depth $h$ (m) | 25.0 | Maximum Tension (kN) | 100.0 |
| Fairlead Ver. Position (m) | −0.75 | Number of Mooring Lines | 3 |
| Fairlead Hor. Position (m) | 1.5 | Line Azimuth Difference (°) | 120 |

### 2.5.2. Correlations of the regular wave cases

The FPS geometry and mooring system configuration were symmetric about the x-axis, so relatively small sway, roll, and yaw motions were expected. The dominant surge, heave, and pitch motions from the time-domain (the linear and the blended) analysis were compared with the model test results.

34 cases were analyzed successfully with reasonable time series patterns. Typical cases are of the form similar to sinusoidal time history (as plotted in Figure 2.14 and Figure 2.15). From the plots, both the linear model and the blended model yield reasonable comparisons with the model tests (for surge and pitch). Motion amplitudes from the blended option look closer (than the linear model) to those from the model test. The heave plots were omitted because the simulated heaves were very close to the model test (with noticeable difference).
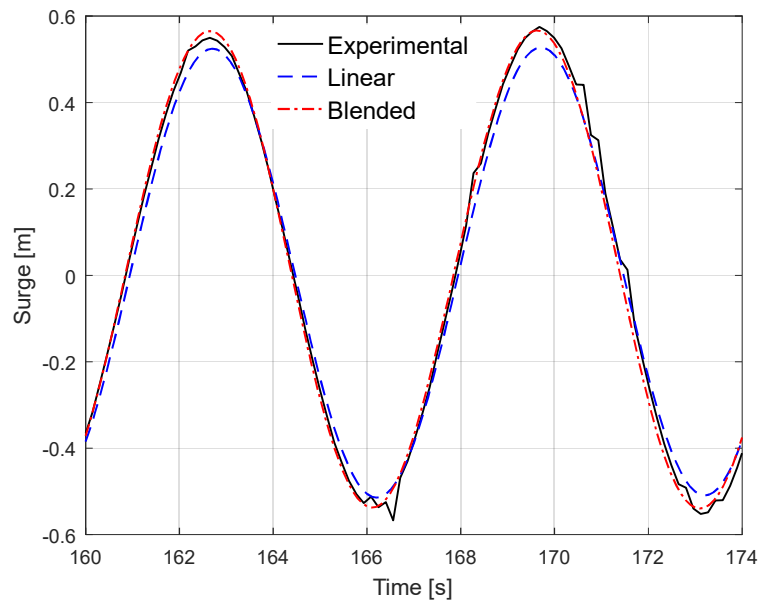
(a) surge
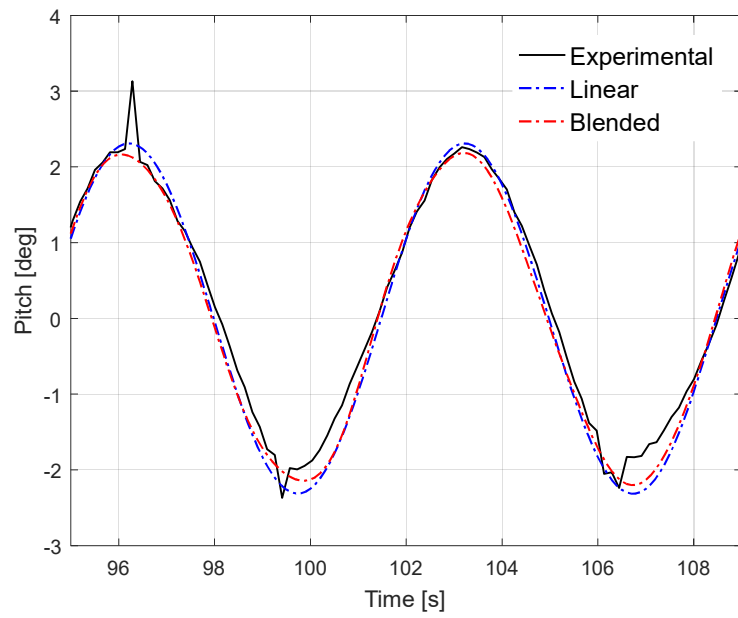


(b) pitch

**Figure 2.15** Motion comparisons for H = 1.0 m, T = 7.0 s: (a) surge; (b) pitch
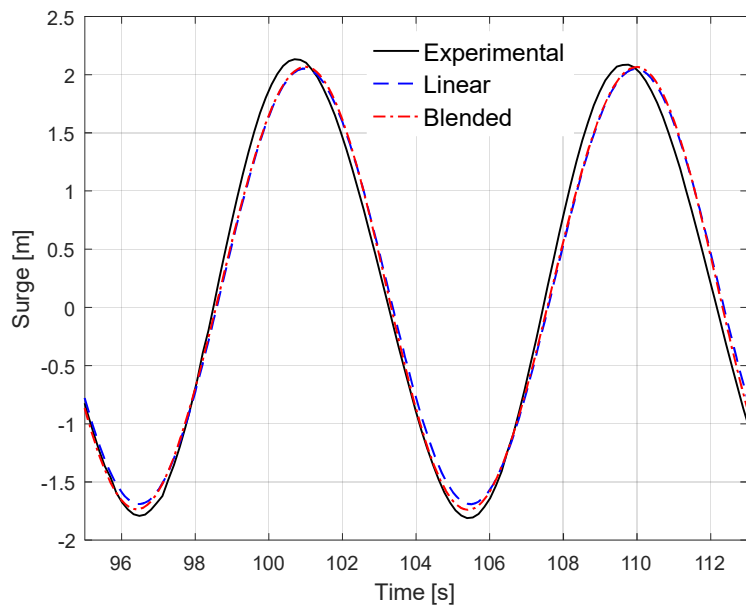
(a) surge
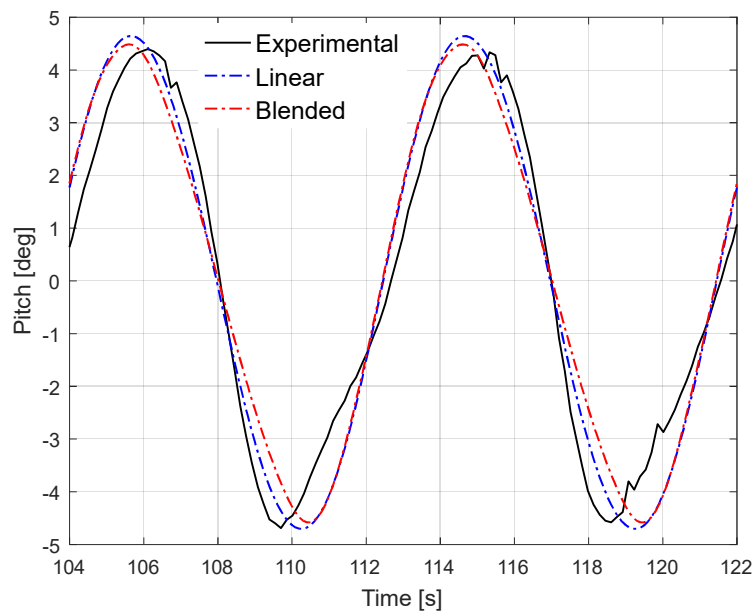


(b) pitch

**Figure 2.16** Motion comparisons for H = 3.0 m, T = 9.0 s: (a) surge; (b) pitch

For the motion time series (longer than 10 min), their standard deviations represent the motion magnitudes. Therefore, the simulation errors are as follows:

$$Error = (std_{sim} - std_{exp})/std_{exp} \times 100\% \qquad (2.29)$$

$std_{sim}$ and $std_{exp}$ are the standard deviations from the simulations and experiments, respectively. Figure 2.16 compares the errors for surge, heave, and pitch.
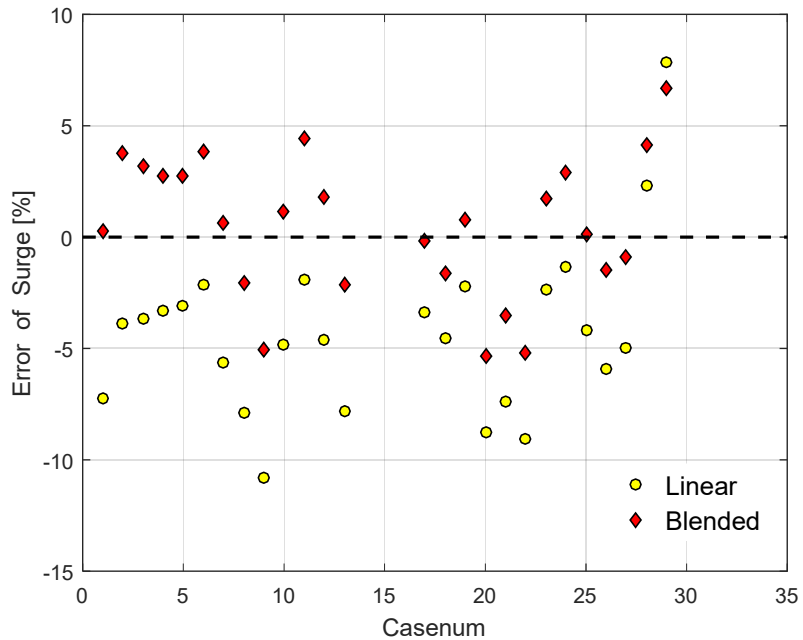


(a) surge

**Figure 2.17** Regular wave case errors: (a) surge; (b) heave; (c) pitch
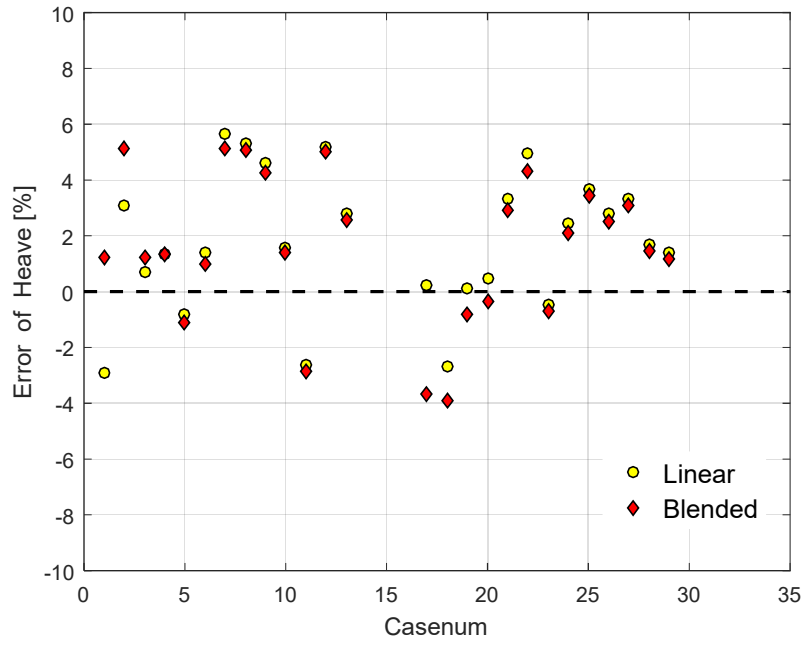
(b) heave
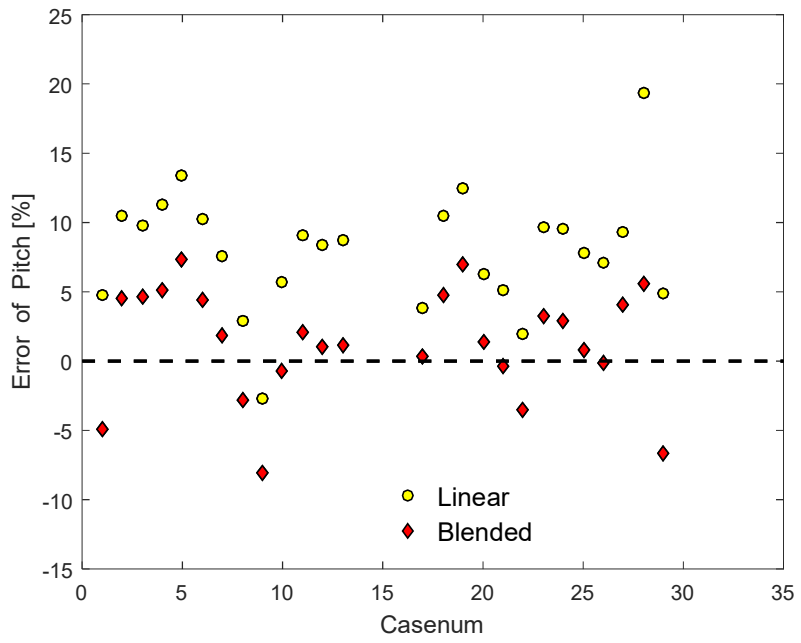


(c) pitch

**Figure 2.18** Continued

Figure 2.16 compares the errors for surge, heave, and pitch. The range [–10%, 15%] bounds 95% of the error dots, meaning that both the linear model and the blended model were found to yield an acceptable error level. While the heave errors from the two model are similar, the blended model was found to yield lower surge and pitch errors compared with the linear model. The statistics in Table 2.3 also reflect this.

**Table 2.5** Comparisons of error for regular wave cases (34 cases)

| Item | | Surge | Heave | Pitch |
|---|---|---|---|---|
| Mean | Linear | –4.0% | 2.0% | 8.2% |
| | Blended | 0.0% | 1.6% | 1.9% |
| Mean of | Linear | 4.8% | 2.6% | 8.3% |
| Abs | Blended | 2.9% | 2.6% | 3.5% |

As listed in Table 2.3, the mean errors of the 34 regular wave cases using the blended method are consistently lower than the mean errors from the linear method for surge, heave, and pitch (consistently).

In the case that the large positive errors cancelled out the large negative errors (meaning the mean errors did not represent the actual error levels), mean absolute errors are listed in Table 2.3 to reflect the level of error in another way. The mean absolute errors from the blended model also were shown to be lower than the mean absolute errors from the linear model, except for heave (which was very close).

Table 2.3 indicates that the blended time-domain method has a considerable advantage in accuracy. The advantage of the blended method can be credited to its capability to account for the nonlinearity in Froude-Krylov, hydrostatic, and inertia forces.

Depending on the computer's CPU capability, the absolute calculation time of the two methods are subject to change. However, the relative speed is meaningful. For a simulation of 3 minute in real time, using step of 0.1s, there should be 1800 steps (number of steps should be the criteria here as the step itself is flexible). Under this setting, the blended method spends 19 times simulation time of that spent by the linear method.

Some factors will influence the relative speed (e.g. the panel number, inclusion of the drift forces, ramp time setting etc.). While the algorithm of the linear SIMDYN is quite mature, the algorithm of the blended SIMDYN has room for more optimization. In general, a fair estimation is that blended time domain method is about 10 times (order of magnitude) slower than the linear time domain method. Please recall that the next higher fidelity model (nonlinear time domain method) is about $10^2$ times (order of magnitude) slower than the linear time domain method (see Yu 2017):

Although in this subsection, using the two modelling approaches, the model test correlations show no significant differences, this happens when the linear results are already fairly close to the model test results, leaving limited room for improvement. Under more severe sea states, the improvements using the blended method are likely to be more significant.

An uncertainty that needs to be pointed out is the mooring modelling. Sensitivities of the motion predictions to the mooring modelling (quasi-static or dynamic) have been

studied by Hall and Goupee (2015) and Yang et al. (2012). While the motion predictions under regular waves are shown to be not sensitive to the mooring modelling in the cases studied, it's necessary to enhance the time domain program by coupling with the dynamic mooring program in the future studies.

For all the regular wave cases, the general trend of the response amplitude ratio (blended/linear) (including surge, heave, and pitch) is plotted in Figure 2.17.
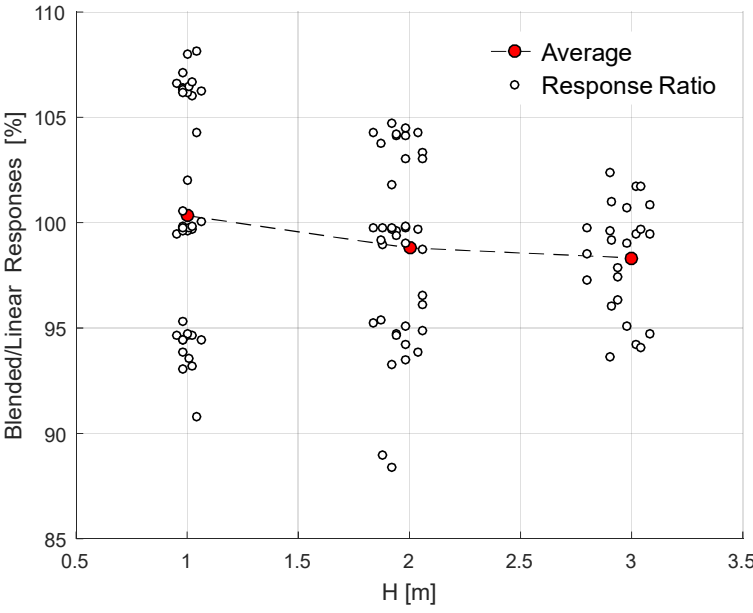


(a) Blended/linear

**Figure 2.19** Response ratio: (a) Blended/linear; (b) Blended/experimental
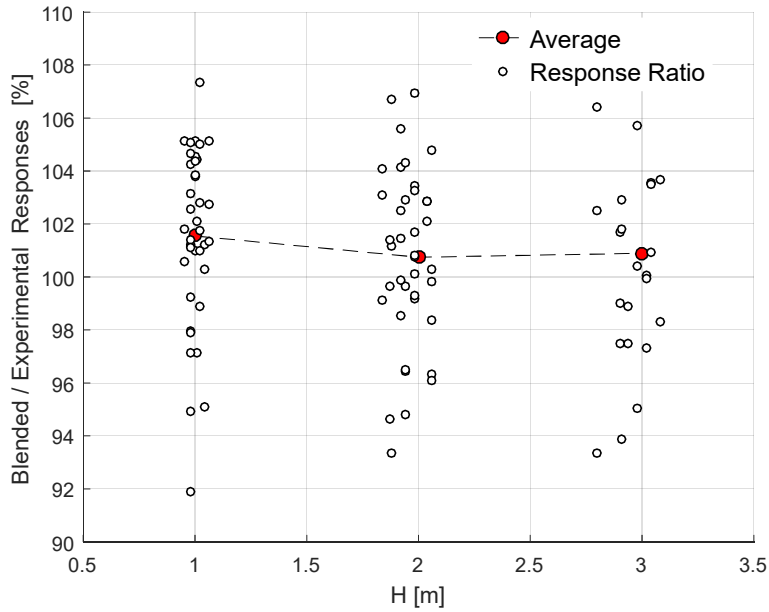
(b) Blended/experimental

**Figure 2.20** Continued

From Figure 2.17 (a), it can be observed that when the wave amplitude and motion amplitude are small, the blended method and the linear method are statistically very close. As the wave and motion amplitude increase, the results from the linear method exceed the results from the blended method. The gradual loss of accuracy of the linear assumptions with the increase of wave and motion amplitude leads to overprediction of the motions from the linear method. In addition, Figure 2.17 (b) indicates that the accuracy of the blend method is quite consistent as the wave height changes.

**2.6. Discussions**

In this section, the blended time domain method was implemented to predict WES motions. This method calculates the important external forces by directly integrating the

instantaneous pressure on the wetted panels of the floating structures. The method also accounts for nonlinearity in the equations of motion (i.e., inertia forces) due to rotations of the rigid body. Correlations with the model test results indicate that the blended time domain method is more accurate than the widely used linear time domain method as it reduces the error of the motion responses.

This study discussed the nonlinear effects of Froude-Krylov, hydrostatic, and inertia forces. The (forced) motion time series were input to the both the linear model and the blended model to compare the corresponding Froude-Krylov, hydrostatic, and inertia forces. As in the forced motion tests, the method used (linear or blended) was the only variable, so the differences between the two methods under certain motion and wave amplitudes could be compared. In general, the gap between the blended method and the linear method widens as the motion amplitude and wave amplitude increases. While the model tests compares generally well with both the linear and blended time domain methods under the examined sea states, it can be reasonably deduced from the forced motion test results that under larger wave amplitudes, the advantages of the blended method may increase substantially.

In this work, a floating power system (FPS) was used in model test correlations. The FPS's geometry was selected from very limited suitable model test data accessible to us. Though not an actual wave energy converter, the FPS is of dimensions and geometry similar to the typical point absorber type wave energy converter. At this stage, the focus of this study is to make sure that the motion predictions from the numerical modelling are accurate (and robust). Even with an actual WEC, for examining the modelling method

51

under different sea states, it is preferable that the power take-off is deactivated. Therefore, as far as simulation is concerned, the floating power system similar to the point absorber. Actually, the improvements of SIMDYN and the confidences/benchmarks gained in this study are the foundation for further study.

# 3. APPLICATION OF SYSTEM IDENTIFICATION TECHNIQUE IN MODEL TEST CORRELATIONS FOR A FLOATING POWER SYSTEM

## 3.1. Reverse Multiple Input Single Output Method

Viscous damping is a "grey" area of uncertainty for modelling tools based on the potential flow theory. Viscous damping plays such an important role in simulating the motions accurately and that is why it needs to be correctly estimated. For typical ships and offshore platforms, the viscous damping corrections can be achieved through empirical methods or through free decay tests. As WESs are relatively novel design, the empirical ship shaped equations for the typical geometry may not be applicable. On the other hand, sometimes the model tests for WESs are inadequate: for the FPS, the free decay test was not available. Moreover, free decay tests are only capable of determining the model scale damping the natural frequency. As an alternative method, the viscous damping can be evaluated through the system identification technique. It can directly deal with cases under random sea states, which is the most common situations as the actual sea states are random.

System identification is not just the choice when other alternatives are absent, it is superior to other methods in that it reveals the variation of transfer functions with frequency, which cannot be effectively done otherwise. Popular system identification techniques include Restoring Force Surface (RFS), Nonlinear Auto-Regressive Moving

Average with eXogenous inputs (NARMAX), Hilbert transform and Reverse-Multiple Input Single Output (R-MISO). After reviewing the advantages and limitations of these techniques, R-MISO is found to be the most desirable method for marine structures. In this subsection, derivations of the Reverse Multiple Input Single Output (R-MISO) method follows the convention of Somayajula and Falzarano (2017).



(a) $m$ original inputs $p_i(t)$ and one output $q(t)$.

(b) $m$ conditioned inputs $p_{i.(i-1)!}(t)$ and one output $q(t)$.
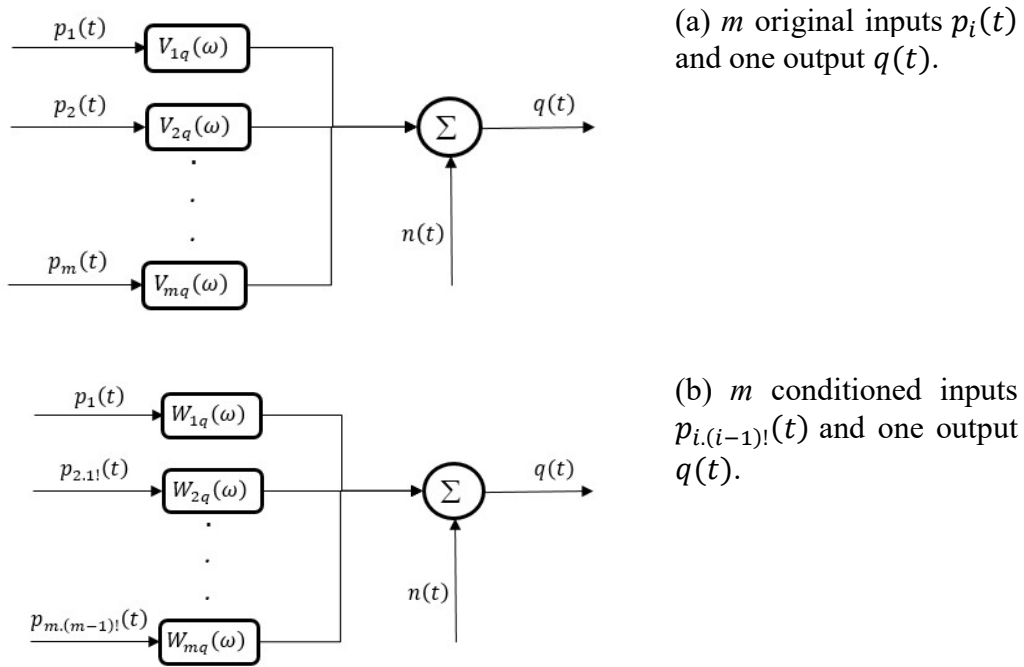
**Figure 3.1** MISO model with unconditioned inputs and conditioned inputs

Figure 3.1 (a) shows a multiple input single output (MISO) system, which consists of m inputs $p_i(t)$, $i = 1, 2, \ldots, m$ and one output $q(t)$. System identification identifies the transfer function from $p_i$ to $q$, $V_{iq}(\omega)$, such that the noise $n(t)$ is minimized. The original inputs $x_i(t)$ can be converted into uncorrelated signals in Figure 3.1 (b) by conditioning an input with the previous inputs:

$$p_i(t) = p_{i:(i-1)!}(t) + p_{i.(i-1)!}(t) \tag{3.1}$$

54

$p_{i:(i-1)!}$ is the part of $p_i$ correlated with $p_1$, $p_2$,..., $p_{i-1}$ and $p_{i.(i-1)!}$ is the part uncorrelated with $p_1$, $p_2$,..., $p_{i-1}$. $W_{ij}(\omega)$ is the transfer function from $p_{i:(i-1)!}$ to $q$. After taking Fourier transform of inputs, output and noise, the system can be expressed in the frequency domain:

$$Q(\omega) = \sum_{i=1}^{m} W_{iq}(\omega)P_{i.(i-1)!}(\omega) + N(\omega) \tag{3.2}$$

Multiply both sides by $\frac{2}{T}P^*_{j.(j-1)!}$ and get the expected value while $T \to \infty$:

$$S_{jq.(j-1)} = W_{jq}S_{jj.(j-1)!} \tag{3.3}$$

In equation 3.3, "*" denotes the complex conjugate and "$E$" denotes the expected value. Each of the conditioned inputs $P_{i.(i-1)!}(\omega)$ and noise $N(\omega)$ are uncorrelated (zero cross spectra), and the conditioned inputs are internally uncorrelated. $S_{jq.(j-1)}$ is the conditional cross spectrum density and $S_{jj.(j-1)}$ is the conditional auto spectrum density. Similar to 3.3, the transfer functions $W_{rj}(\omega)$ between the conditioned inputs $p_{i.(i-1)!}$ and one output $q$ are:

$$S_{rj.(r-1)!} = W_{rj}S_{rr.(r-1)!} \tag{3.4}$$

To be more general, for $P_j(\omega)$, if $P_{j.r!}(\omega)$ represents the part of $P_j(\omega)$ that is uncorrelated with $P_1$, $P_2$, ... , $P_r$, then:

$$\sum_{i=1}^{r} W_{ij}(\omega)P_{i.(i-1)!}(\omega) + P_{j.r!}(\omega) = \sum_{i=1}^{r-1} W_{ij}(\omega)P_{i.(i-1)!}(\omega) + P_{j.(r-1)!}(\omega) \tag{3.5}$$

Taking the difference between the two sides of 3.5:

$$P_{j.r!}(\omega) = P_{j.(r-1)!}(\omega) - W_{rj}P_{r.(r-1)!} \tag{3.6}$$

Multiply both sides by $\frac{2}{T}P^*_{i.r!}$ and get the expected value under the limit $T \to \infty$:

$$S_{ij.r!} = S_{ij.(r-1)!} - \frac{S_{rj.(r-1)!}}{S_{rr.(r-1)!}}S_{ir.(r-1)!} \tag{3.7}$$

This is the recursion relation to calculate the conditioned cross spectrum $S_{ij.r!}$.

### 3.1.1. Transfer function

For the original (unconditioned) system, the frequency domain output $Q(\omega)$ is:

$$Q(\omega) = \sum_{i=1}^{m} V_{iq}(\omega)P_i(\omega) + N(\omega) \tag{3.8}$$

Multiply 3.8 by $\frac{2}{T}P^*_{j.(j-1)!}$ and take the expected value while $T \to \infty$:

$$S_{jq.(j-1)!} = \sum_{i=j}^{m} H_{iq}\,S_{ji.(j-1)!} \tag{3.9}$$

Divide both sides by $S_{jj.(j-1)!}$ and substitute using 3.3 and 3.4:

$$W_{iq} = \sum_{i=j}^{m} V_{iq}\,W_{ji} \qquad i = 1, 2, \dots, m \tag{3.10}$$

Equation 3.10 can be used to calculate $V_{jq}$ from $W_{jq}$ by subtracting backwards:

$$\begin{cases} V_{mq} = W_{mq} \\ V_{jq} = W_{jq} - \displaystyle\sum_{i=j+1}^{m} W_{ji}\,V_{iq} \qquad j = m-1, m-2, \dots, 2, 1. \end{cases} \tag{3.11}$$

### 3.1.2. Partial coherence function

With the conditioning approach, the partial coherence functions, $\gamma^2_{iq.(i-1)}$, reveal the contribution of the conditioned inputs $p_{i.i-1}$ to the output $q$:

$$\gamma_{iq.(i-1)}^2(\omega) = \frac{|S_{iq.(i-1)}(\omega)|^2}{S_{ii.(i-1)}(\omega)S_{qq}(\omega)} \tag{3.12}$$

The sum of the first n (n ≤ m) partial coherence functions is the cumulative coherence function. The contribution from all the (m) inputs to the cumulative coherence function should always be less than equal to 1.

## 3.2. Model Test Setup and Time Domain Analysis
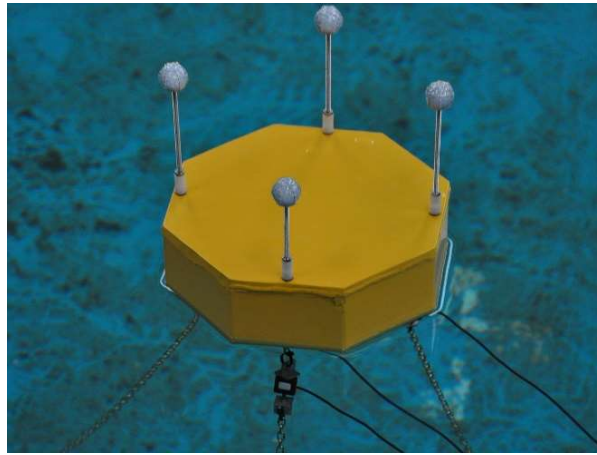


**Figure 3.2** Floating Power System tested by Bosma et al. (2014), reprinted with permission

The model tests of the floating power device (see Figure 3.2) were performed at Beaufort Research/HMRC, Ireland (Bosma et al., 2014). The floating power system is a necessary unit in the wave energy conversion system. It was selected because:

(1) Fully public model test data of wave energy structures is rare and very valuable. The data used in this study is open access. All the necessary information for simulation is complete.

(2) The system identification method is general enough. Actually, the dimensions and geometry of the device are similar to a point absorber type wave energy converter (which is believed to be the most typical form).

An additional advantage makes the selected model tests more attractive:

(3) Many other open model test data of wave energy device measured the information of generated electricity (voltage, current) but the motion and time history (that is most relevant) is not accessible. This study intentionally selected the tests without power take off, which reduces uncertainties (the power take off is another nonlinear damping, which is difficult to be simulated accurately without more details).
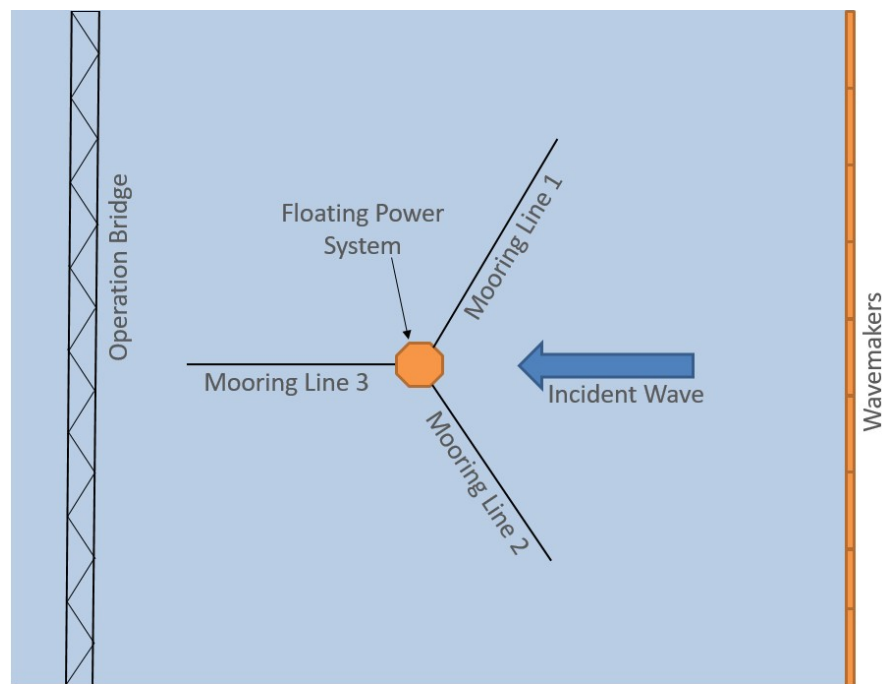


**Figure 3.3** 0° wave test by Bosma et al. (2014), adapted with permission

The 0-degree wave heading series are selected for verification of SIMDYN and R-MISO analysis. The model test configuration (Bosma et al., 2014) is shown in Figure 3.3. The configuration (FPS geometry and mooring system configuration) is symmetric about the x axis.

From the 1:25 scale model tests, the calibrated incident wave at the FPS positions, the motions of the FPS in six degrees of freedom, and the mooring line tensions at the three fairleads were measured by Beaufort Research/HMRC (Bosma et al., 2014). Wave was measured using two wire resistive type wave probes. The motion time series were output by the Qualisys track manager software. The mooring line forces were measured using Futek load cells.

The 0-degree wave heading tests consisted of regular incident wave tests with wave height ranging from 1.0 m ~ 3.0 m and wave period ranging from 4.0 s ~ 17.5 s. In the regular wave cases, for surge, heave and pitch (the three dominant motions, the average error between SIMDYN and the model tests is -4.0%, 2.0% and 8.2%, respectively. The simulation errors are defined as follows:

$$Error = (std_{sim} - std_{exp})/std_{exp} \times 100\% \qquad (3.13)$$

$std_{sim}$ and $std_{exp}$ are the standard deviations from the simulations and experiments, respectively. Considering these errors are before the damping correction is applied in the simulations, it means that SIMDYN yields relatively good accuracy in predicting the motions (for regular incident waves). There are 9 irregular (random wave) cases selected for system identification analysis. Detailed model test correlation will be demonstrated in the next subsection.

The time domain simulations were conducted with SIMDYN (Wang et al., 2020) using the linear option for the inertia forces, the Froude Krylov forces and the hydrostatic forces. The governing equation (see ANSYS Inc. 2011) is:

$$[M + MA(\infty)]\ddot{x}(t) + Kx(t) + \int_0^t h(t - \tau)\ddot{x}(\tau) = F_e(t) \qquad (3.14)$$

$M$ is the mass matrix, $MA(\infty)$ is the added mass matrix at infinite frequency;

$K$ is the hydrostatic stiffness;

$h(t)$ is the acceleration convolution integral function;

$F_e(t)$ are the total external forces. $F_e(t)$ includes Froude Krylov forces, scattering forces, mooring forces and slowly varying wave drift forces.
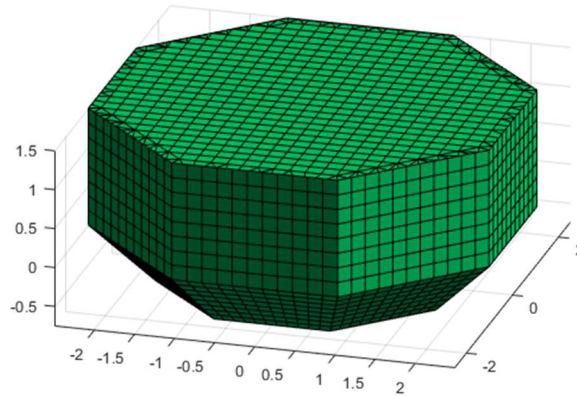


**Figure 3.4** Panel model of the FPS used in MDL-HYDROD

The Froude Krylov forces and scattering forces are obtained from the in-house frequency domain hydrodynamics analysis program MDL-HYDROD (see Guha 2012; Liu and Falzarano, 2017). Figure 3.4 shows the panel model used in MDL-HYDROD.

The origin (0, 0, 0) to define six degrees of freedom body motion is located on the calm water level of the central axis. The 3-leg mooring system is modeled by coupling SIMDYN with the open-source Mooring Analysis Program (MAP++). The simulations and the experiments used the same mooring parameters (as listed in Table 2.2) to be as accurate as possible.

For the irregular wave cases, the motion responses (surge, heave and pitch) are compared in Table 3.1. The comparisons of the motion responses are given by the ratio of the standard deviations from SIMDYN to those from the model tests.

**Table 3.1** Motion responses ratio (SIMDYN/model test)

| Sea state | Hs | Tp | Surge | Heave | Pitch |
|---|---|---|---|---|---|
| 1 | 3.00 | 6.0 | 77.5% | 101.8% | 121.1% |
| 2 | 3.00 | 7.5 | 76.6% | 102.8% | 125.1% |
| 3 | 3.00 | 8.5 | 78.3% | 102.7% | 121.6% |
| 4 | 1.75 | 7.5 | 77.6% | 101.2% | 109.5% |
| 5 | 1.75 | 8.5 | 84.2% | 100.9% | 106.6% |
| 6 | 1.75 | 10.0 | 91.1% | 101.0% | 100.4% |
| 7 | 1.75 | 12.5 | 97.7% | 101.2% | 102.7% |
| 8 | 1.75 | 15.0 | 93.0% | 101.9% | 107.5% |
| 9 | 1.75 | 17.5 | 99.6% | 102.1% | 108.3% |
| Average | | | 86.2% | 101.7% | 111.4% |

From Table 3.1, it can be found that the surge motion is about 13.8% lower than the model tests. This may be explained by the inevitable discrepancy in modelling the mooring system and that the surge motion is relatively more sensitive to the mooring modelling.

The slowly varying wave drift forces may also account for part of the discrepancy. Even though the slowly varying wave drift forces are calculated using the full quadratic transfer function (QTF) evaluated by Xie et al. (2019) using Pinkster's approximation (see Pinkster 1980), the drift forces remain to be examined further.

Considering the uncertainties in the drift forces and mooring system modelling that significantly affect the surge motion more than the heave and the pitch, the surge motion will be studied but no damping or viscous drag correction will be implemented.

In addition, since it can be observed that cases 1~3, cases 4~6 and cases 7~9 are similar in significant wave heights and standard deviations, they are put into 3 groups.

## 3.3. Coherence Analysis

The coherence analysis aims to reveal the most relevant input variables for a given degree of freedom. If the partial coherence function for an input variable is not significant (always smaller than 0.1 or greater than 0.1 in frequency range where the motion power spectrum density, PSD, is very small), it means that the contribution from that input variable may be removed from the R-MISO analysis. In this way, the partial coherence functions can help us determine which input variables are suitable for R-MISO. In actual practice, it seems that sometimes R-SISO is good enough (e.g. for the heave) in getting good correlation between simulations and model tests.

In addition, the cumulative coherence functions are plotted to show the goodness for coherence analysis (presenting how much percentage of the output variable is contributed by all the selected input variables combined). The motion power spectrum density (PSD) from the model tests is also plotted for the investigated degree of freedom. This is very helpful because the frequency range with little energy distribution (e.g. for pitch, frequency greater than 2.2 rad/s) is not important.

From the mass matrix in calculating the motion RAO, it is known that the surge and the pitch is coupled (through the non-zero vertical center of gravity) while the heave due to fore and aft symmetry is relatively independent. Consequently, for surge: the input variables are surge motion $x_1$, quadratic surge velocity $v_1|v_1|$ and pitch motion $x_5$ while the output variable is surge diffraction (incident and scattering) excitation force (note that the drift force is not included in the R-MISO). Similarly, for the heave: the input variables are heave motion $x_3$ and quadratic heave velocity $v_3|v_3|$ while the output variable is the heave diffraction (incident and scattering) excitation force. For pitch: the input variables are pitch motion $x_5$, quadratic pitch velocity $v_5|v_5|$ and surge motion $x_1$ while the output variable is the pitch diffraction (incident and scattering) excitation moment.

### 3.3.1. Coherence function for surge

Figure 3.5 and Figure 3.6 show the coherence analysis for the surge under sea state 3 and sea state 7, respectively. They are quite representative of the coherence functions for surge.
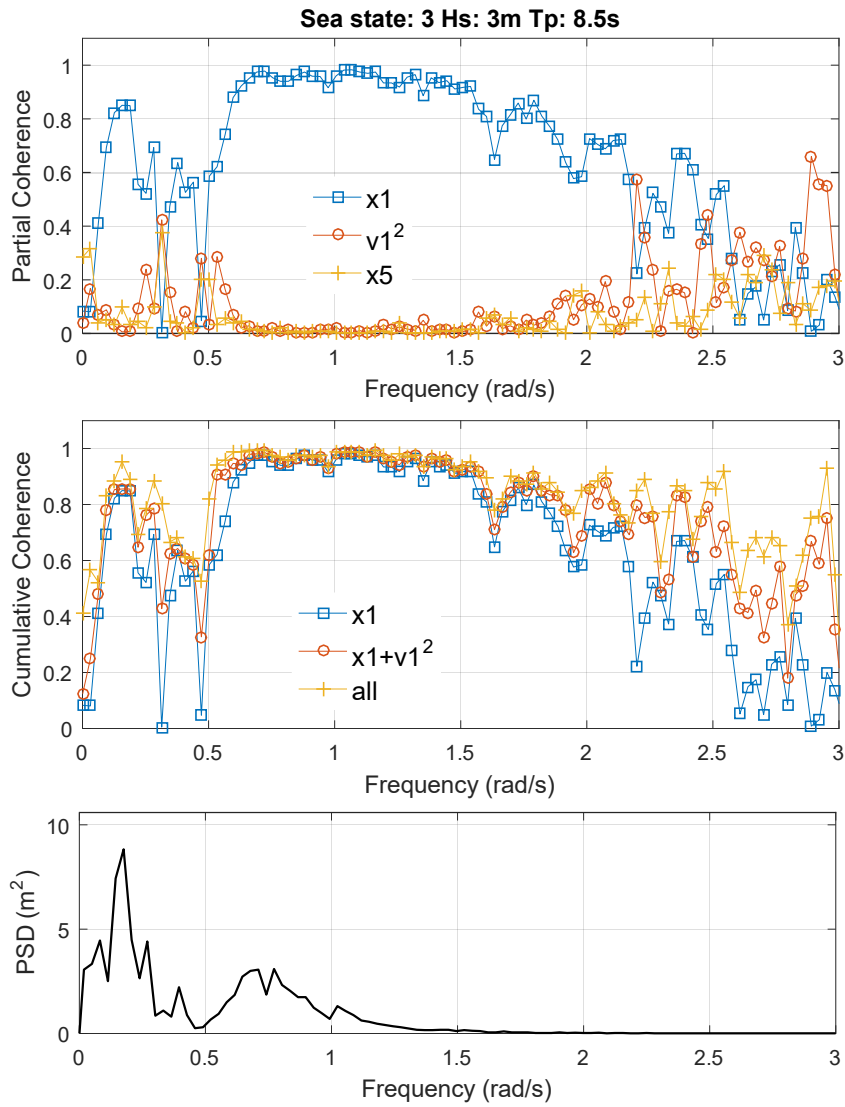
**Figure 3.5** Surge coherence analysis for sea state 3
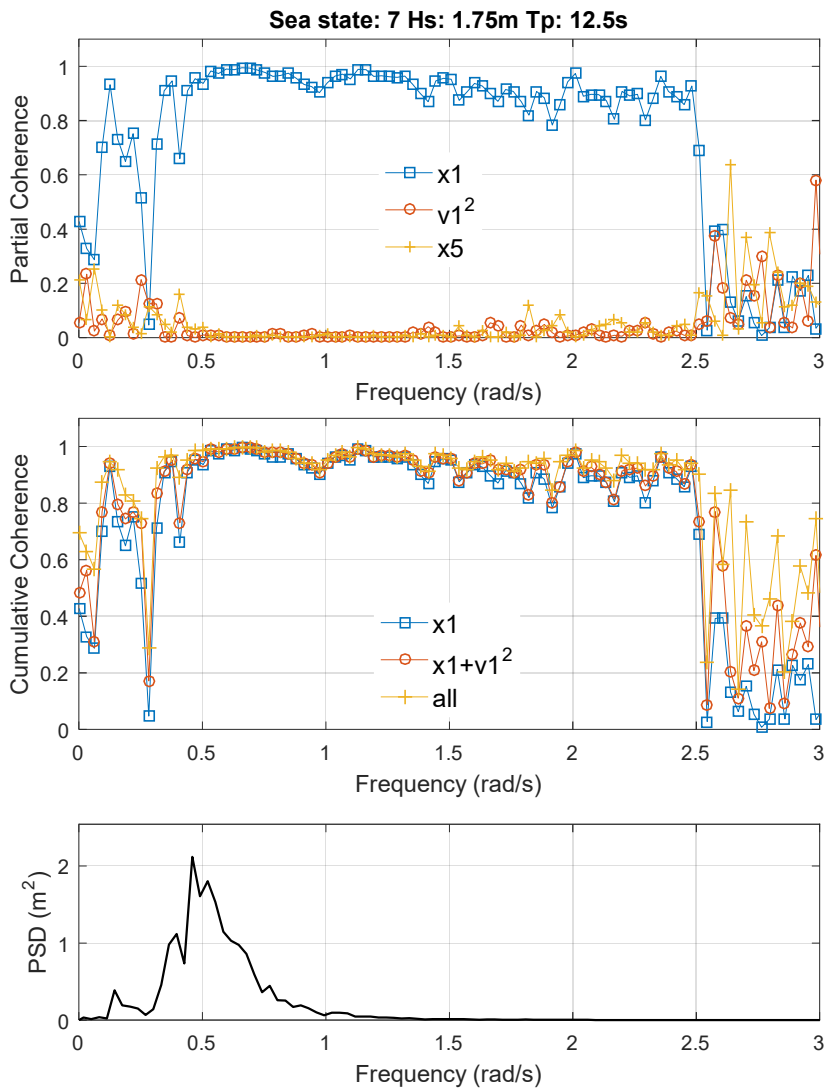
**Figure 3.6** Surge coherence analysis for sea state 7

It can be found that the first input variable surge motion $x_1$ contributes above 80% while the quadratic surge velocity $v_1^2$ and pitch motion $x_5$ are usually small within important surge PSD range. It should be noted that surge under sea state 3 is different from that under sea state 7 in that it has significant low frequency (largely drift contribution) but due to surge drift force assessment in SIMDYN and MDL-HYDROD, that part may

65

not be captured well by the R-MISO technique at this moment. The R-SISO technique (the only input variable is the surge motion $x_1$) is therefore adopted for surge to help understand the linear damping in surge.

### 3.3.2. Coherence function for heave

Figure 3.7 and 3.8 show coherence analysis for the heave in sea state 3 and 9, respectively. They are quite representative of the coherence functions for the heave.

**Sea state: 3 Hs: 3m Tp: 8.5s**
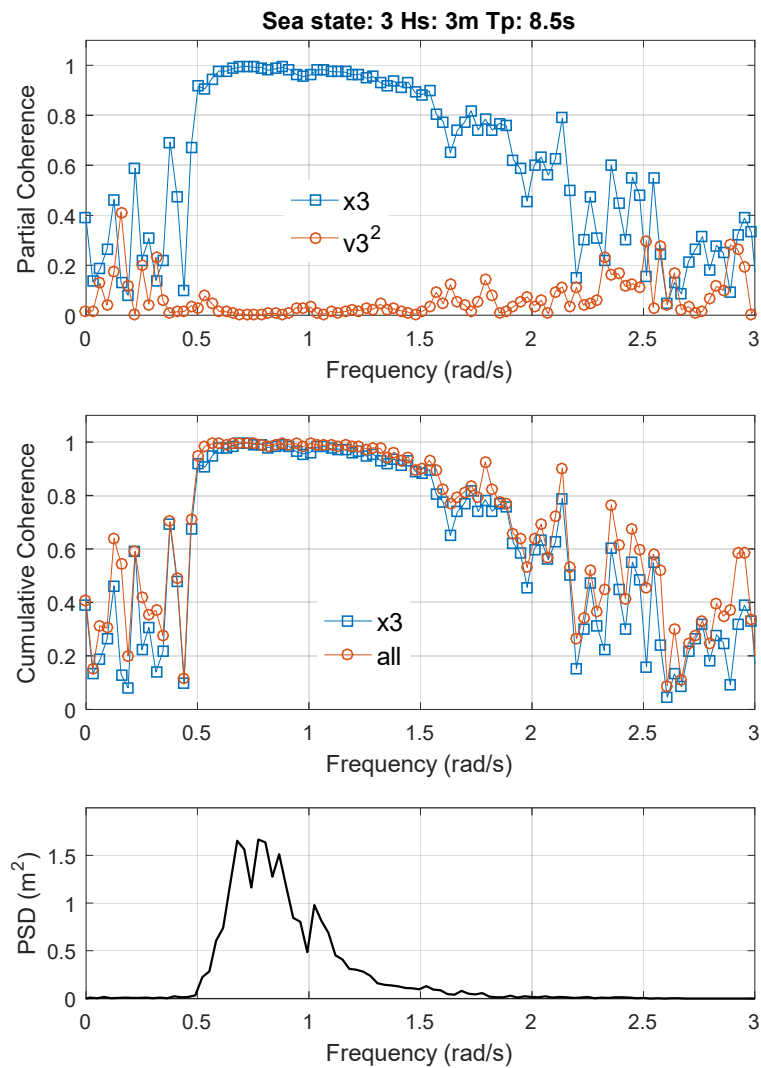


**Figure 3.7** Heave coherence analysis for sea state 3
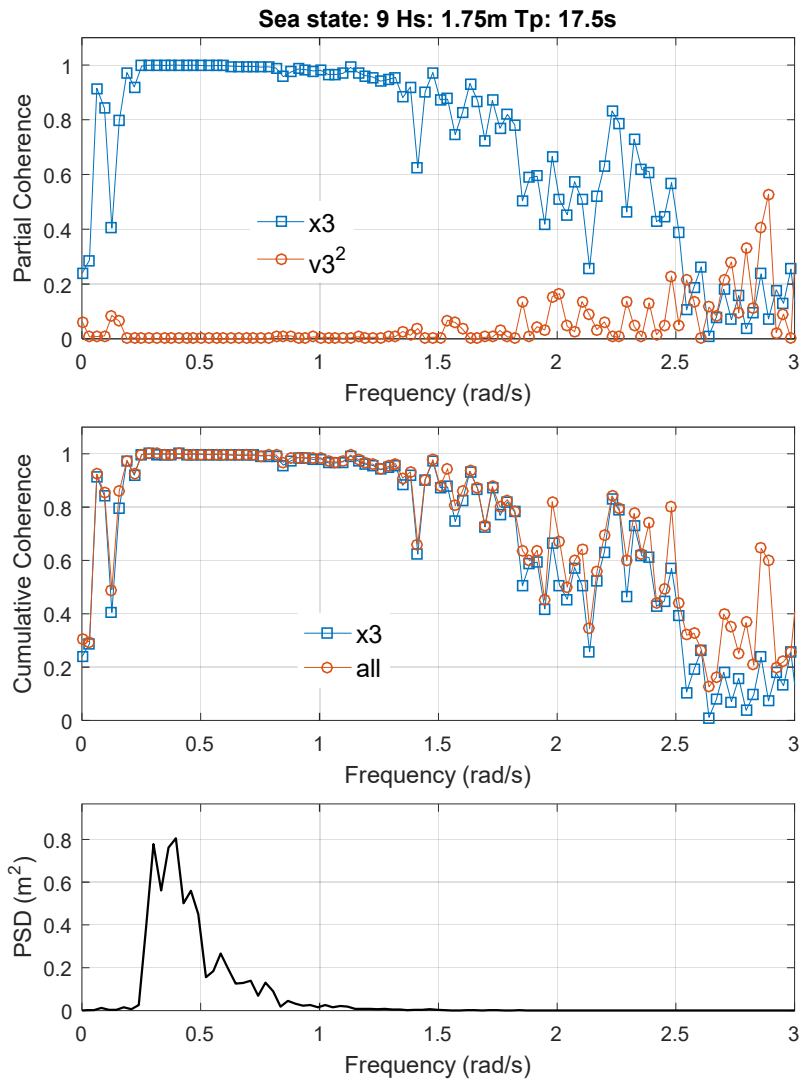
**Figure 3.8** Heave coherence analysis for sea state 9

It can be found that the first input variable heave motion $x_3$ contributes above 95% (the dominant effect) while the quadratic heave velocity $v_3^2$ contribution is small within important heave PSD range for the heave (0.4 rad/s ~ 1.6 rad/s). Therefore the transfer

function analysis of the heave is performed using the R-SISO technique and the only input variable is the heave motion $x_3$.

### 3.3.3. Coherence function for pitch

Figure 3.9 and 3.10 show coherence analysis for the pitch in sea state 2 and 9, respectively. They are quite representative of the coherence functions for pitch.
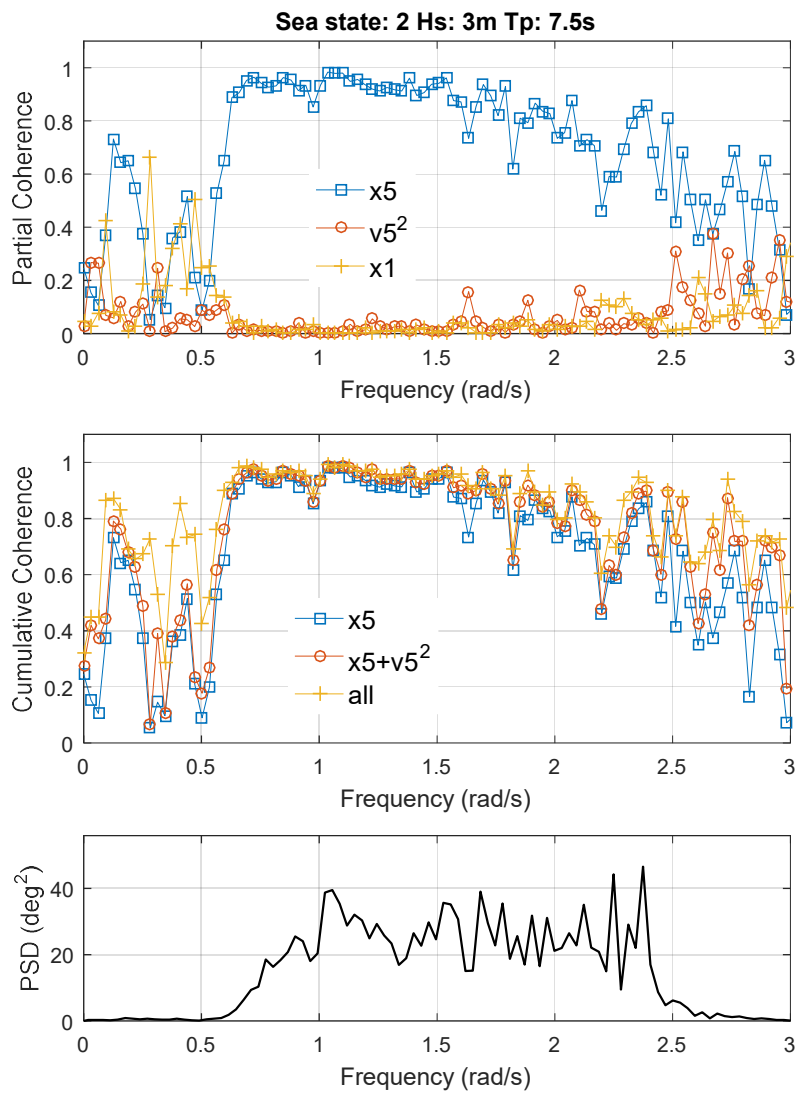


**Figure 3.9** Pitch coherence analysis for sea state 2
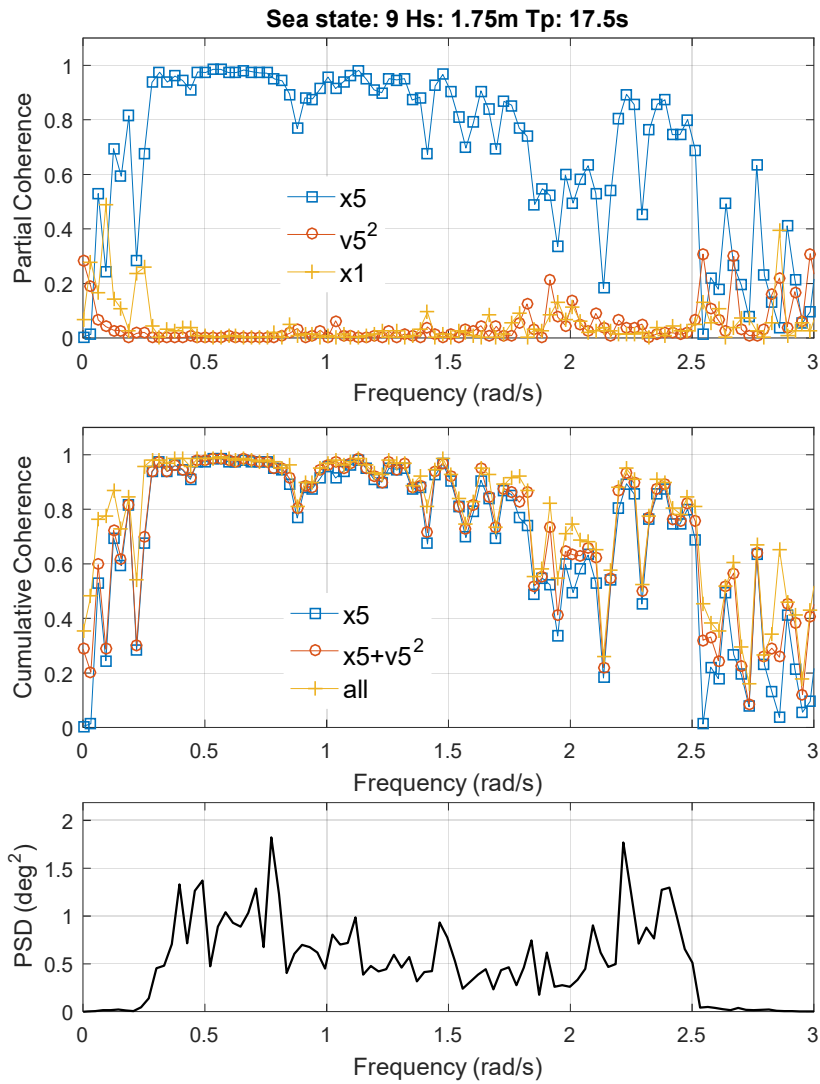
**Figure 3.10** Pitch coherence analysis for sea state 9

It can be found that the first input variable pitch motion $x_5$ contributes above 60% and contribution from the quadratic pitch velocity $v_5^2$ is not negligible within important pitch PSD range (0.5 rad/s ~ 2.5 rad/s). The surge motion $x_1$ should also be included in R-MISO transfer function analysis after the surge motion (i.e. surge drift) can be modeled

better. In the current R-MISO transfer function analysis for the pitch, the first input is the pitch motion $x_5$ and the other input is the quadratic pitch velocity $v_5|v_5|$.

The generic transfer function from the motion $x_i$ to the diffraction excitation $F_i$ is:

$$H_{ii}(\omega) = K_{ii} - \omega^2[M + MA_{ii}(\omega)] + i\omega[D(\omega) + D_a(\omega)] \qquad (3.14)$$

Besides the terms that have been declared in equation 3.13, $D(\omega)$ is the (linear) radiation damping, which corresponds to energy dissipation in the radiated waves (excited by the oscillation of the structure).

$D_a(\omega)$ is the additional linear damping due to viscous effects. The additional linear damping (and the additional quadratic damping) needs to be implemented because our (time domain) simulations are based on the potential flow theory. In the potential flow theory, viscosity of the fluid is not taken into consideration. $D_a(\omega)$ can be evaluated by several different methods (including free decay tests, system identifications). If no linear damping correction is made, $D_a(\omega)$ will be zero, which neglects the (linear) viscous effects.

Before an oscillatory flow separates from the surface of the body, the viscous damping force can be modeled well as a linear function of velocity. After an oscillatory flow separates from the surface of the body, the viscous damping force can be modeled more reasonably as a quadratic function of velocity.

The quadratic damping is also induced by viscosity. While the linear viscous damping is mainly attributed to the frictional force between the fluid and the submerged body (within the boundary layer), the quadratic damping is mainly induced by the flow

70

separation as well as the vortex shedding. Actually, the two forms of the viscous damping are usually used together to better approximate the real viscous effects.

## 3.4. Transfer Function Analysis

### 3.4.1. Transfer function for surge

As discussed in subsection 3.3.1, R-SISO analysis is applied to the surge equation of motion. The surge transfer function shown in Figure 3.11 is typical for the 9 irregular sea states. In the R-SISO analysis, the input is the surge motion time series (from the experiments and from the SIMDYN simulations, respectively) while the output is the surge force time series. The derived system identification technique in subsection 3.1.1 is used to calculate the transfer function from the time series.
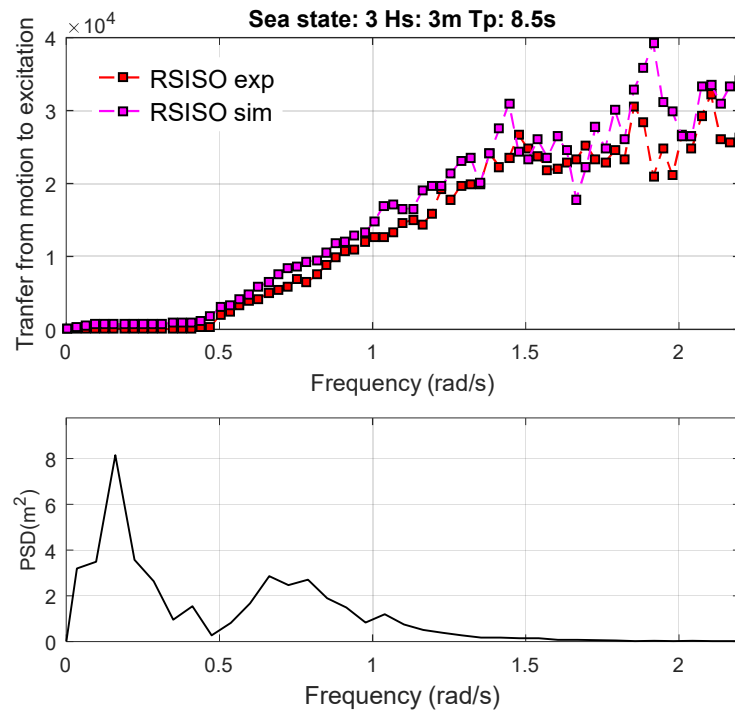


**Figure 3.11** Typical surge R-SISO results

In general, the transfer function for the wave frequency is modeled correctly. As much of the surge variance exists in the low frequency region that is closely related to the slowly varying surge drift force, modelling remains to be improved by better evaluation for the drift force.

### 3.4.2. Transfer function for heave

As discussed in subsection 3.3, R-SISO analysis is applied to the heave motion. Figure 3.12 shows the typical heave transfer functions. In general, R-SISO analysis shows that the heave motion is modeled very accurately without any damping correction.
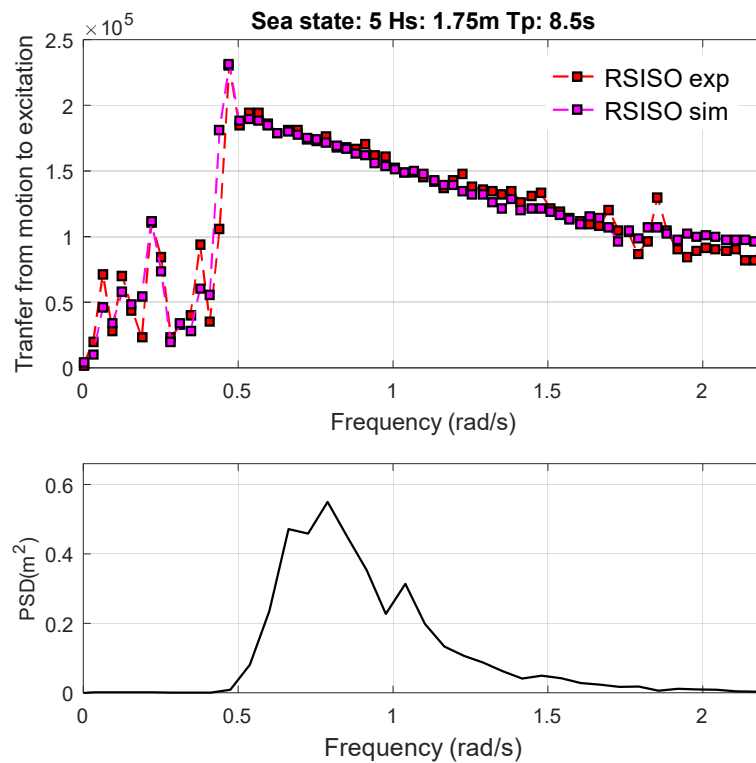


**Figure 3.12** Sea state 5 heave transfer function from the R-SISO

Considering that the heave standard deviation difference between the model tests and the SIMDYN results are already within 0.9% (on an average 1.7% error only), it's believed that additional damping correction is not necessary.

Figure 3.13 is a typical heave time series comparison with the model test. The simulation program directly takes the calibrated wave time history at the FPS's moored position (provided by the Beaufort Research/HMRC, Ireland) for the corresponding sea states. The calibrated waves are repeatable. Therefore, when the FPS is in place, the incident wave is identical to the calibrated wave. This confirms that for the heave the R-SISO method is good enough.
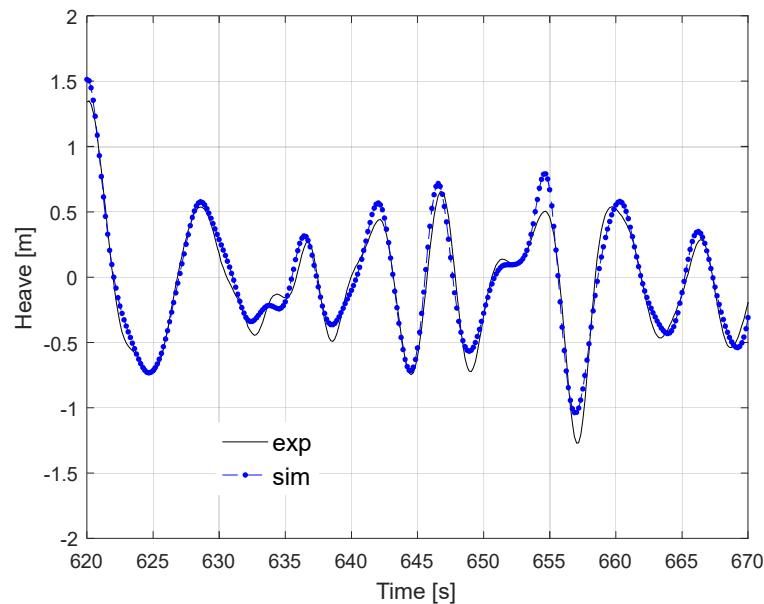


**Figure 3.13** Sea state 5 heave correlation with model test

### 3.4.3. Transfer function for pitch

The R-MISO technique turns out to be more valuable for pitch in this study. The first transfer function between the pitch motion and the pitch moment is the equation 3.14 while the second transfer function $V_q$ satisfies the equation 3.15 below (ANSYS Inc. 2011 and Orcina Ltd. 2019):

$$V_q \cdot (v_i|v_i|) = F_q \tag{3.15}$$

$F_q$ is the quadratic damping force. $V_q$, the second transfer function is usually determined from the model test. Recall that the typical formula for the drag force is:

$$\frac{1}{2}\rho C_D A \cdot (v_i|v_i|) = F_q \tag{3.16}$$

By comparing equation 3.15 with equation 3.16, it is reasonable to assume that the second transfer function $V_q$ (i.e. the quadratic damping) is a coefficient.

Using the R-MISO technique, we can assess how much linear damping in the equation 3.14 and quadratic damping in the equation 3.15 that needs to be added into the simulation. Based on the transfer function, damping corrections can be made in the time domain simulations.

Sea state 9 is a typical case that the linear damping needs to be compensated. The square of transfer function error is the indicator for deciding upon the damping corrections. The procedure is as follows (take sea state 9 as an example):

(1) Perform the system identification analysis to get the transfer functions from the experiments and simulations;

Figure 3.14 shows the pitch transfer function from R-MISO for sea state 9.
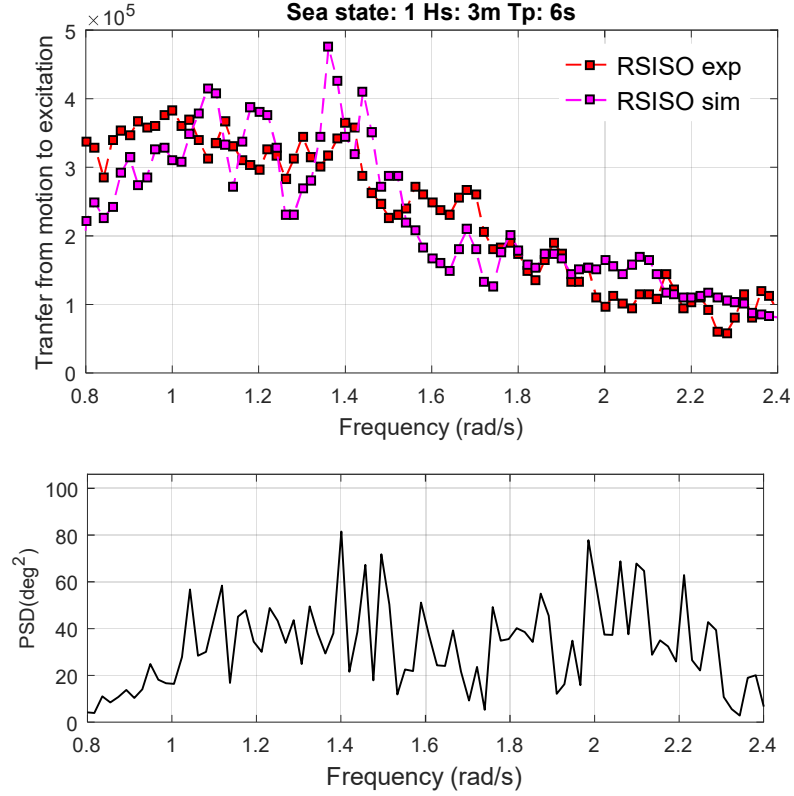
**Figure 3.14** Sea state 1 pitch transfer function from R-MISO

(2) Within the estimated damping correction range, ($[0, 4\times10^4]$, using the step of $1\times10^3$), calculate the error indicator $SE$ (sum of the spectrum weighted error of the transfer functions):

$$SE = \sum_{i=1}^{nf} |(|V_{sim\_c}(\omega_i)| - |V_{exp}(\omega_i)|) \cdot \sqrt{S(\omega_i)}| \qquad (3.17)$$

$V_{sim\_c}$ represents the transfer function of simulation after proposed damping corrections. $S(\omega_i)$ is the PSD at the frequency $\omega_i$. $nf$ is the number of frequencies. Equation 3.17 can efficiently address the optimal damping correction, $D_{opt}$, that

75

minimizes the difference between $V_{sim\_c}$ and $V_{exp}$. Making this damping correction will best fit the transfer function in the simulation to the transfer function in the model test:
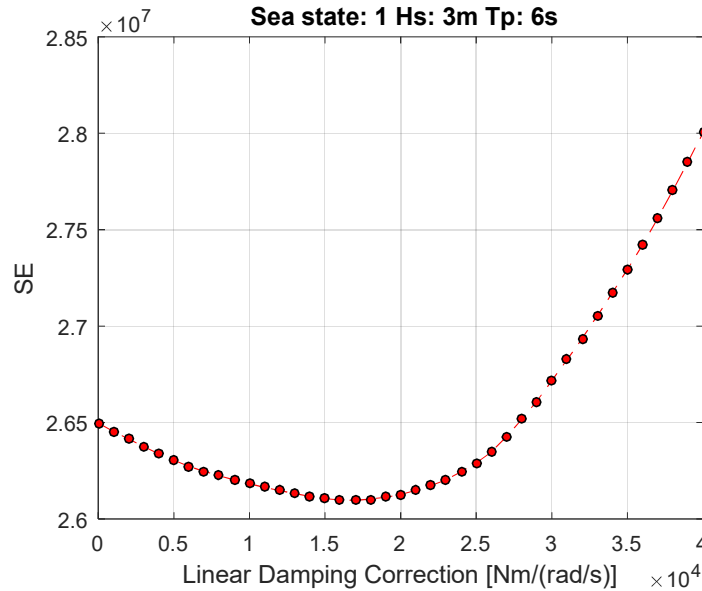


**Figure 3.15** Determining sea state 1 linear damping correction

Figure 3.15 shows how the optimal linear damping correction is determined for sea state 1. Based on Figure 3.15, additional $1.7{\times}10^4 \; N \cdot m/(rad/s)$ linear damping is estimated and should be implemented into the time domain simulation.

(3) Run the time domain simulation with the optimal damping correction, $D_{opt}$. Repeat steps (1) and (2) on the simulation after the damping correction. This procedure will show that no damping correction is necessary, which means the current damping correction is the optimal one.

Figure 3.16 shows the pitch transfer function from R-MISO after the damping correction. In general, the comparison improved over the frequency range 0.8 rad/s ~ 2.4 rad/s (from the pitch PSD).
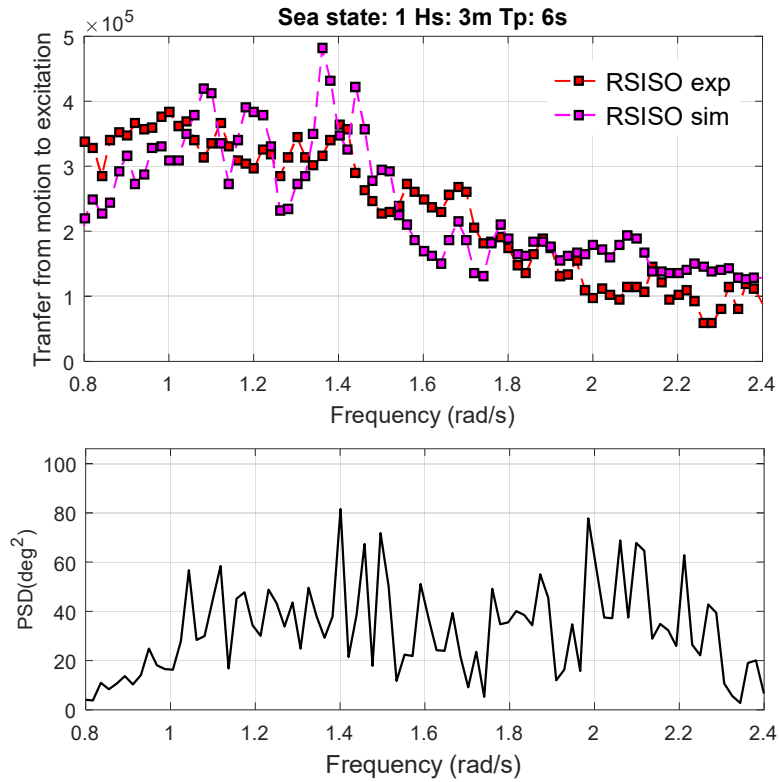


**Figure 3.16** Sea state 1 (after the linear damping correction) pitch transfer function

Figure 3.17 shows that any additional (on top of $1.7\times10^4\ N \cdot m/(rad/s)$ that has been implemented in the simulation) linear damping correction is not necessary for sea state 9. This verifies that the damping correction $D_{opt}$ is the stable optimal correction.
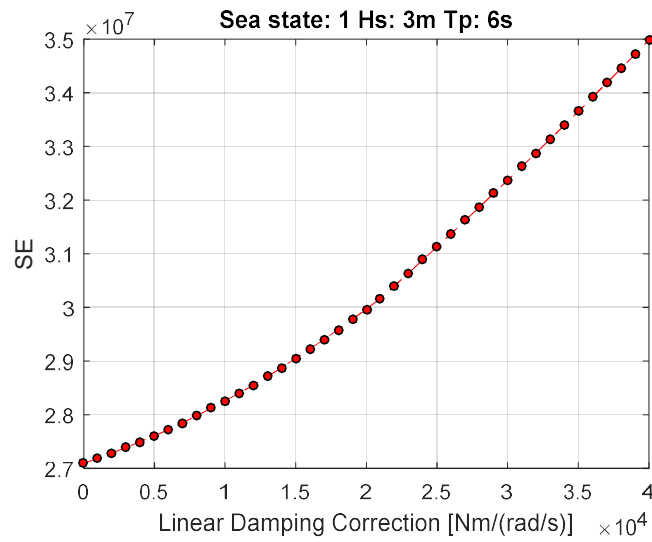
**Figure 3.17** Verfying sea state 9 linear damping correction

Correspondingly, in the time domain simulation, the standard deviation error drops

significantly from 21.1% to -1.5%. The better correlation is also observed in Figure 3.18.
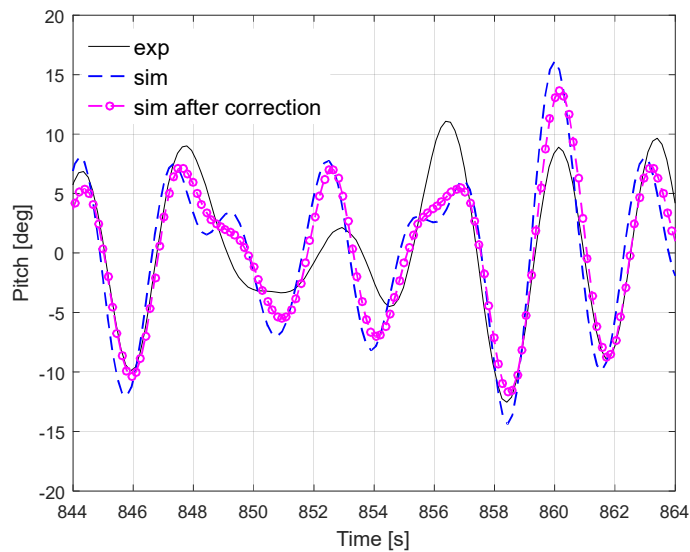


**Figure 3.18** Sea state 1 pitch time series comparison

Using similar method, the quadratic damping corrections can also be evaluated. Sea state 4 is a typical case where the quadratic damping needs to be compensated for. Figure 3.19 shows the second transfer function from R-MISO.
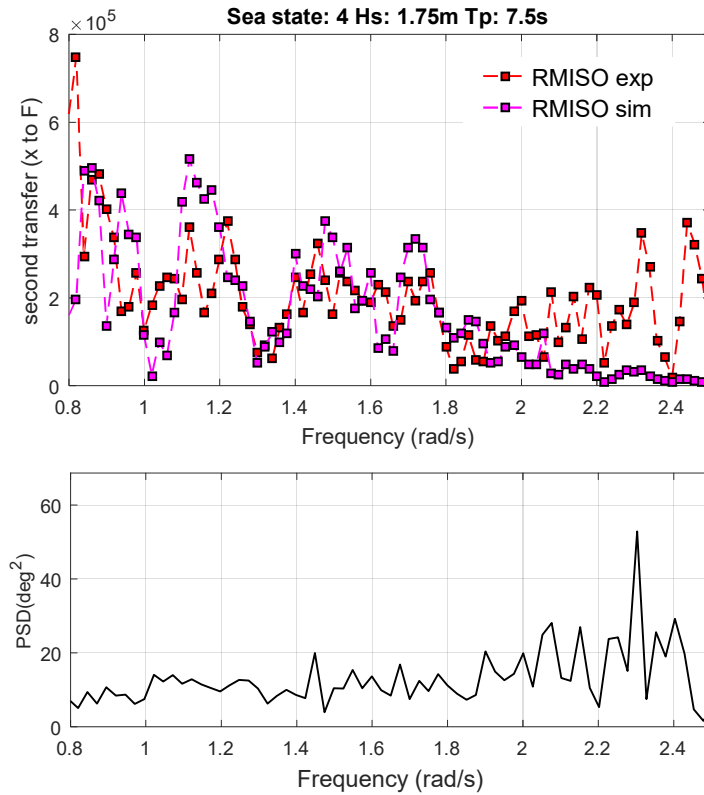


**Figure 3.19** Sea state 4 pitch second transfer function before correction

Figure 3.20 shows how the optimal quadratic damping correction is determined for sea state 4. Based on Figure 3.20 and the equation 3.15, additional $3.5 \times 10^4 \ N \cdot m/(rad/s)^2$ quadratic damping is estimated and is implemented into the time domain simulation.
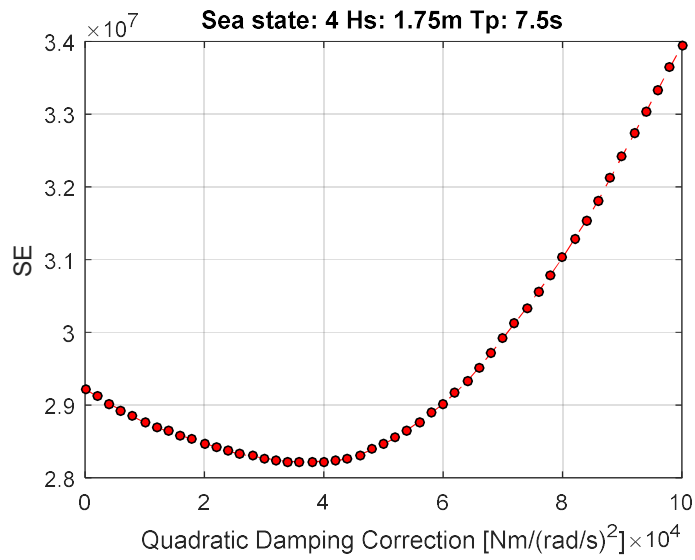
**Figure 3.20** Determining sea state 4 quadratic damping correction
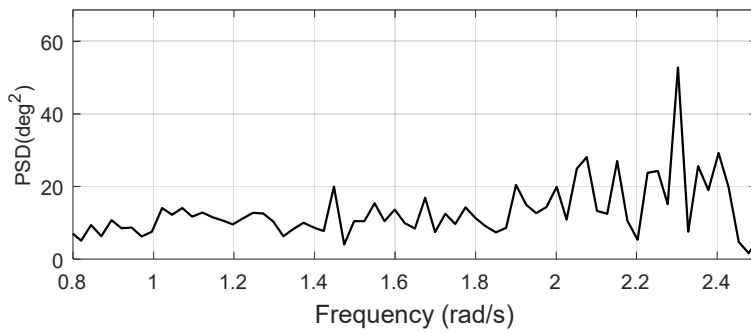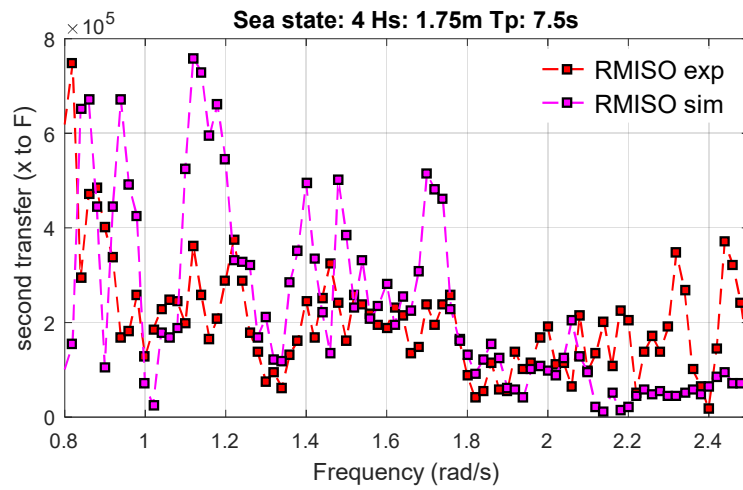


**Figure 3.21** Sea state 4 pitch second transfer functions after correction

Figure 3.21 shows the second transfer function (the corresponding input is the quadratic pitch velocity) from R-MISO after the damping correction. In general, the comparison improved over the frequency range 0.8 rad/s ~ 2.5 rad/s (from the pitch PSD).

Figure 3.22 shows that any additional (on top of $3.5 \times 10^4 \ N \cdot m/(rad/s)^2$ that has been implemented in the simulation) quadratic damping correction is not necessary for sea state 4. This verifies that the quadratic damping correction $V_q$ is the optimal correction.
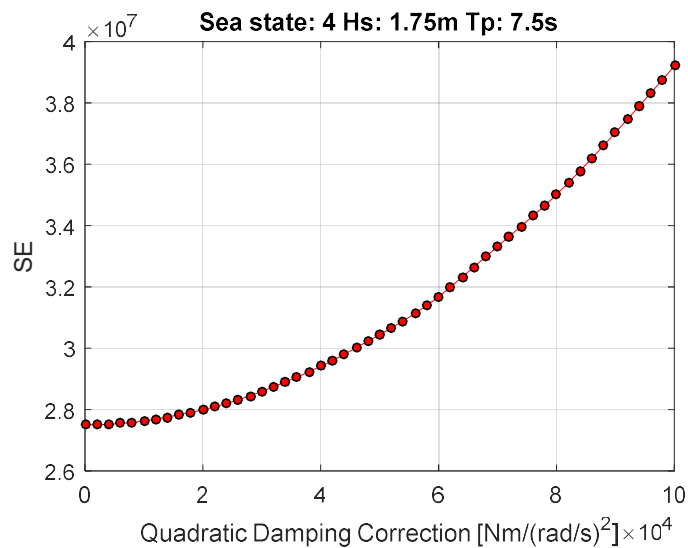


**Figure 3.22** Verfying sea state 4 quadratic damping correction

Correspondingly, in the time domain simulation, the standard deviation error drops from 9.5% to -1.6%. The improved correlation can also be observed in Figure 3.23.
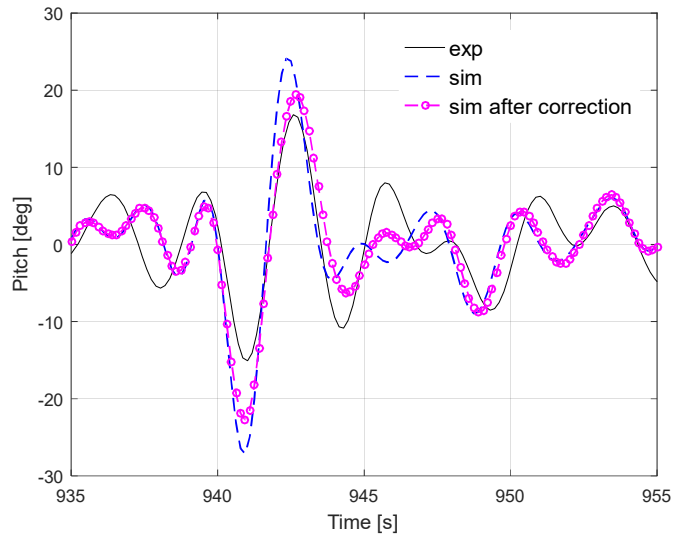
**Figure 3.23** Sea state 4 pitch time series comparison

Similar corrections are made for the other irregular sea states. The damping corrections and the standard deviation improvements are listed in Table 3.2. On the average, the absolute error of standard deviation is reduced from 11.4% to 2.3%.

**Table 3.2** Motion responses ratio (SIMDYN/model test) after damping corrections

| Sea state | Linear correction | Quadratic correction | Pitch w/o correction) | Pitch w. correction) |
|:---:|:---:|:---:|:---:|:---:|
| 1 | $1.7 \times 10^4$ | | 121.1% | 98.5% |
| 2 | | $4.8 \times 10^4$ | 125.1% | 102.2% |
| 3 | | $4.0 \times 10^4$ | 121.6% | 103.8% |
| 4 | | $3.5 \times 10^4$ | 109.5% | 98.4% |
| 5 | $0.9 \times 10^4$ | | 106.6% | 97.8% |

| 6 | | | 100.4% | 100.4% |
|---|---|---|---|---|
| 7 | $1.0\times10^4$ | | 102.7% | 96.9% |
| 8 | | $9.6\times10^4$ | 107.5% | 101.8% |
| 9 | $2.1\times10^4$ | | 108.3% | 95.9% |
| Average of absolute error | | | 11.4% | 2.3% |

The dimensional damping values can be better benchmarked after conversion to the non-dimensional damping ratio, which equals the dimensional damping divided by the critical damping, $B_{55c}$. The pitch critical damping (for small angle) is:

$$B_{55} = 2\sqrt{(I_{55} + A_{55}) \cdot C_{55}} \tag{3.18}$$

$C_{55}$ is the hydrostatic stiffness for pitch. The critical pitch damping value for this FPS is $2.025\times10^5$ N·m/(rad/s). To provide a uniform percentage of

When necessary, a quadratic viscous damping value derived from the irregular wave model tests can be linearized to an "equivalent viscous damping", which is linear. If the stochastic linearization (Falzarano et al., 2015) is applied:

$$D_e = \frac{8}{\pi} V_q \cdot std\_v_i \tag{3.19}$$

$D_e$ is the equivalent (linear) viscous damping. $V_q$ is the quadratic damping coefficient defined in equation 3.15. $std\_v_i$ is the standard deviation of the response (velocity). In this way, all damping corrections from system identification can be compared (as linear terms). Table 3.3 lists the pitch damping corrections (linear or quadratic) and the linearized (equivalent) damping values.

**Table 3.3** Linearized pitch damping and the damping ratio

| Sea state | Hs | Tp | Linear correction | Quadratic correction | Linearized values | Damping ratio |
|---|---|---|---|---|---|---|
| 1 | 3 | 6 | $1.7 \times 10^4$ | | $1.7 \times 10^4$ | 8.4% |
| 2 | 3 | 7.5 | | $4.8 \times 10^4$ | $2.5 \times 10^4$ | 12.3% |
| 3 | 3 | 8.5 | | $4.0 \times 10^4$ | $1.9 \times 10^4$ | 9.4% |
| 4 | 1.75 | 7.5 | | $3.5 \times 10^4$ | $1.3 \times 10^4$ | 6.4% |
| 5 | 1.75 | 8.5 | $0.9 \times 10^4$ | | $0.9 \times 10^4$ | 4.4% |
| 6 | 1.75 | 10 | | | | 0.0% |
| 7 | 1.75 | 12.5 | $1.0 \times 10^4$ | | $1.0 \times 10^4$ | 4.9% |
| 8 | 1.75 | 15 | | $9.6 \times 10^4$ | $1.1 \times 10^4$ | 5.4% |
| 9 | 1.75 | 17.5 | $2.1 \times 10^4$ | | $2.1 \times 10^4$ | 10.4% |
| Average | | | | | $1.4 \times 10^4$ | 6.9% |

It can be observed that all equivalent damping corrections are in the order of $10^4$ N·m/(rad/s) and that they vary around the average level of $1.4 \times 10^4$ N·m/(rad/s). The damping ratio is around 6.9% but in certain cases, it can get as high as 12.3%.

Though there is no available pitch damping ratio data from a geometry close enough to this FPS, it can be benchmarked by previous pitch damping studies for different geometries (see Table 3.4 and Figure 3.24 below).

**Table 3.4** Pitch damping ratio from different studies (no strakes)

| Geometry | Function | Damping Ratio | Method | Researcher |
|---|---|---|---|---|
| Bare cylinder | Spar | 2% | Free decay tests | Haslum (2000) |
| Multi-cylinder | Spar | 1.9%~3.1% | Free decay tests | Li et al. (2011) |
| Modified cylinder | Spar | 1.3%~4.9% | Free decay tests | Nallayarasu & Mathai (2017) |
| Water-drop | WEC | 9.6%~10.0% | Free decay tests, CFD | Poguluri et al. (2019) |
| Modified cylinder | Spar | 4.6%~11.3% | Free decay tests, CFD | Nallayarasu & Mathai (2016) |
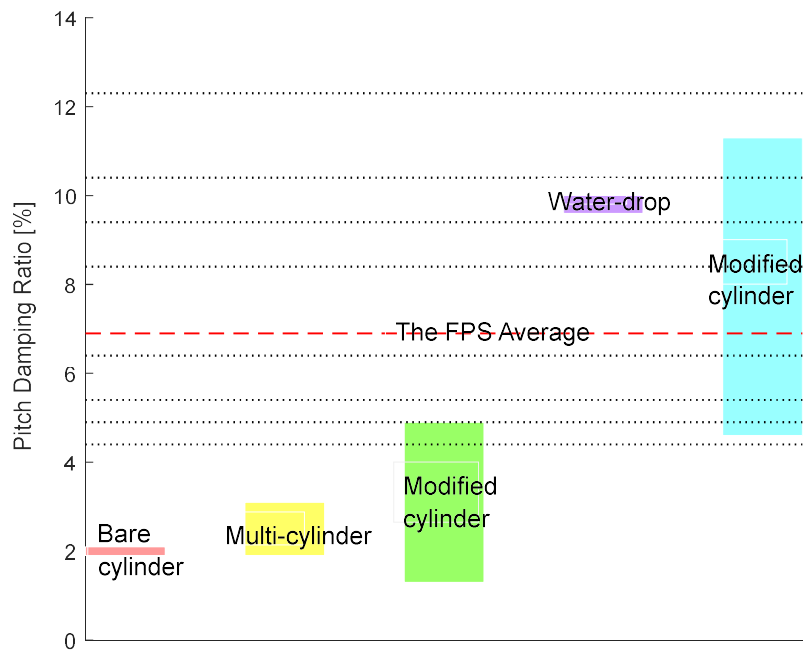


**Figure 3.24** Pitch damping ratio from different studies (no strakes)

It can be found that the pitch damping ratio from previous peer studies for different geometries varies within the range 1.3%~11.3% with an average of about 5.1%. This is a primary benchmark indicating that the damping ratio obtained for the FPS using the system identification method is quite reasonable.

## 3.5. Discussions

Coherence analysis through system identification provides a frequency domain perspective of the simulation. For this wave energy device, it reveals that the heave degree of freedom can be modeled well even without damping corrections as a single input (heave motion) single output (heave force) system. Both linear damping and quadratic damping contribute considerably to the pitch motion in the multiple inputs (pitch motion and quadratic pitch velocity) single output (pitch moment) system. Coherence analysis shows that the surge motion is more sensitive to the low frequency drift forces. Further improvements of the simulation program are needed to better carry out the R-MISO analysis on the surge motion.

System identification has corrected the pitch damping effectively for various sea states in this study. Conventionally, the viscous damping can be estimated by: a) empirical formula: which gives (rough) estimates of the damping but the accuracy varies significantly; b) free decay tests: only provide the damping at the natural frequency; c) forced oscillation tests: they are generally limited to model scale and test facilities are very expensive.

In the model tests of the FPS (by Beaufort Research/HMRC), free decay tests or forced oscillation tests were not performed. There is no empirical formula appropriate for this geometry (as it is a relatively novel form of a floating device). System identification is not just the choice when other methods are nonapplicable, it (i.e. R-MISO in this study) is superior to other methods. It reveals the variation of transfer functions with frequency, which cannot effectively be done otherwise. It can directly deal with cases under random sea states, which is the most meaningful situations, as the actual sea states in nature are random.

In fact, the viscous damping itself under different sea states varies considerably (in this study, the wave height ranges from 1.75 m to 3.0 m and peak period ranges from 6.0 s to 17.5 s). Using Reverse-MISO, not only a constant additional quadratic damping at the natural frequency can be obtained such as from free decay tests (no incident wave involved) but that the effective ("effective" means that incident waves are present, and it is therefore more realistic) damping can be obtained.

# 4. THE PITCH VULNERABILITY OF A TYPICAL WAVE ENERGY CONVERTER GEOMETRY BASED ON MELNIKOV AND MARKOV APPROACHES

## 4.1. Generic Study Object

While the performance under the "normal" operational mode largely determine whether the design is economically efficient, the performances under the "survival" mode largely determine whether the design is physically feasible. Important quantities for the "survival" mode include:

• Local accelerations: may lead to structure failure and fatigue;

• Mooring loads: may lead to mooring lines breakage;

• Roll and pitch: may lead to capsizing.

Compared with the local accelerations and the mooring loads, which are analyzed extensively in the typical global performance analysis, the dynamic stability is given relatively less attention. Actually, several model tests of point absorber type WECs (Payne et al., 2008; Sheng et al., 2012; Gomes et al., 2012) have observed instability phenomenon, which can induce unexpected roll/pitch capsizing. As for a WES, the "head seas" situation is usually what is of most concern, since WESs have no forward speed. In head seas, the first concern, as for its dynamic stability, is the pitchpoling due to the direct wave excitation. In this study, the most common WES form: a moored floating cylindrical geometry is used as a generic model, for which the modelling and analysis are representative of the majority of WES designs.

The content of the section is organized as follows. Subsection 4.1 describes the details of the generic hull form of the study: i.e., a floating cylindrical structure with alternative mooring systems. Subsection 4.2 discusses the application of the Melnikov approach to the hull form described in subsection 4.1. Subsection 4.3 discusses the application of the Markov approach to the hull form described in subsection 4.1. Subsection 4.4 compares the Melnikov approach and the Markov approach and compares their sensitivities to parameters (e.g. the damping).

Table 4.1 shows the general dimensions of a generic floating cylinder. Its cylindrical geometry is selected based on the fact that majority of WECs are basically, cylindrical. The dimensional parameters are not determined according to any particular design, but determined to represent a generalized floating cylindrical WEC.

**Table 4.1** Floating cylinder information

| Characteristic | Value |
| --- | --- |
| Mass $M$ (kg) | 12554.6 |
| Length $Lpp$ (m) | 4.00 |
| Breadth $B$ (m) | 4.00 |
| Height $D$ (m) | 3.00 |
| $VCG$ (m) from water line | 0.20 |
| $Kxx$ (m) | 1.338 |
| $Kyy$ (m) | 1.338 |
| $Kzz$ (m) | 1.414 |

| | |
|---|---|
| Draft $T$ (m) | 1.00 |
| Water Depth $h$ (m) | 20.0 |

*VCG* is the vertical center of gravity and it is measured from the calm water plane. *Kxx*, *Kyy* and *Kzz* are the radii of gyration, around the center of gravity of the floating cylinder. Figure 4.1 (a) depicts the geometry of the floating cylinder defined in Table 4.1 (note that a single mooring line is attached). Figure 4.1 (b) shows the original (without mooring and viscous damping) pitch response amplitude operator (RAO) calculated by the frequency domain hydrodynamic analysis program MDL-HYDROD (Guha, 2012). It can be observed that the natural frequency is around 1.13 rad/s.
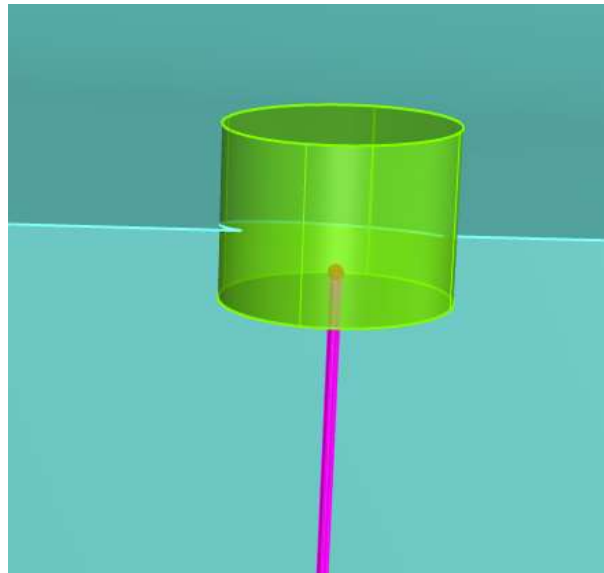


(a) Geometry of the floating cylinder

**Figure 4.1** Geometry of the floating cylinder
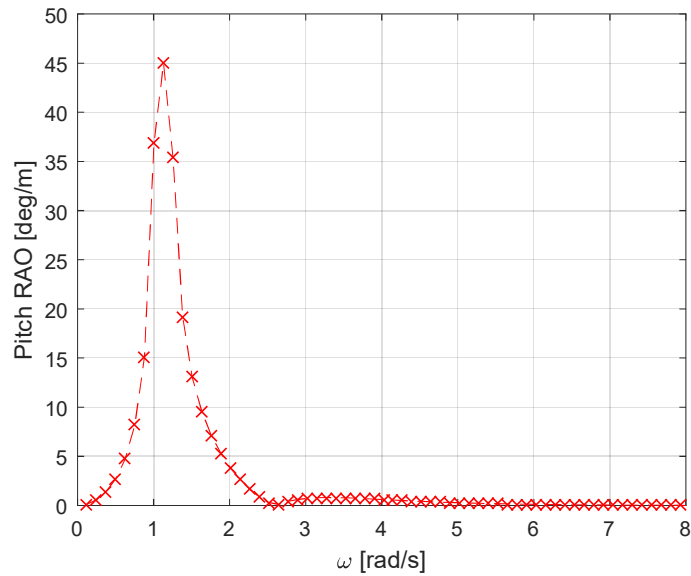
(b) Original pitch RAO of the floating cylinder

**Figure 4.2** Conitnued

The influences from the mooring system are the fundamental differences between a positioned floating system and a ship. For the generic floating cylinder in this study, two common mooring systems are considered: i.e., a single line mooring system and a multiple (three) leg mooring system. Figure 4.2 shows the three alternative mooring configurations (a: no mooring; b: a single mooring leg; c: three mooring legs). The detailed information of these (sample) mooring systems is listed in Table 4.2.
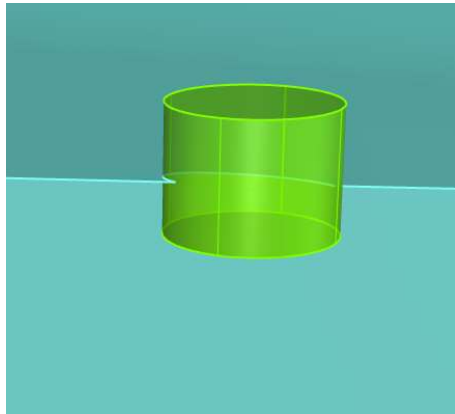
(a) No mooring leg
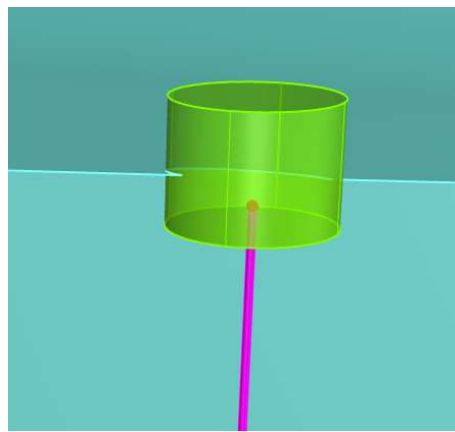


(b) Single mooring leg
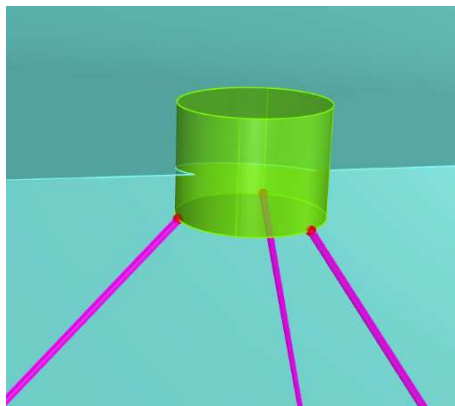


(c) 3 mooring legs

**Figure 4.3** Mooring system configurations

**Table 4.2** Mooring system information

| Characteristic | Value | Characteristic | Value |
|---|---|---|---|
| Single mooring leg | | 3 mooring legs | |
| Fairlead Ver. Position (m) | –1.0 | Fairlead Ver. Position (m) | –1.0 |
| Fairlead Hor. Position (m) | 0.0 | Fairlead Hor. Position (m) | 2.0 |
| Anchor Ver. Position (m) | –20.0 | Anchor Ver. Position (m) | –20.0 |
| Anchor Hor. Position (m) | 0.0 | Anchor Hor. Position (m) | 65.0 |
| Mooring Line Length (m) | 19.0 | Mooring Line Length (m) | 75.0 |
| Mass/Unit Length (kg/m) | 28.4 | Mass/Unit Length (kg/m) | 28.4 |
| Mooring Line Diameter (m) | 0.15 | Mooring Line Diameter (m) | 0.15 |
| Added Mass Coefficient | 1.0 | Added Mass Coefficient | 1.0 |
| Trans. Drag Coefficient | 1.0 | Trans. Drag Coefficient | 1.0 |
| Longi. Drag Coefficient | 0.025 | Longi. Drag Coefficient | 0.025 |
| EA (N/m) | $4.0\times 10^5$ | EA (N/m) | $1.0\times10^8$ |
| Maximum Tension (kN) | 100.0 | Maximum Tension (kN) | 100.0 |
| Number of Mooring Lines | 1 | Number of Mooring Lines | 3 |
| Line Azimuth Difference (°) | 0 | Line Azimuth Difference (°) | 120 |

The mooring system is modelled by implementing the open-source mooring program MAP++ into SIMDYN. Figure 4.3 shows how MAP++ works within SIMDYN.
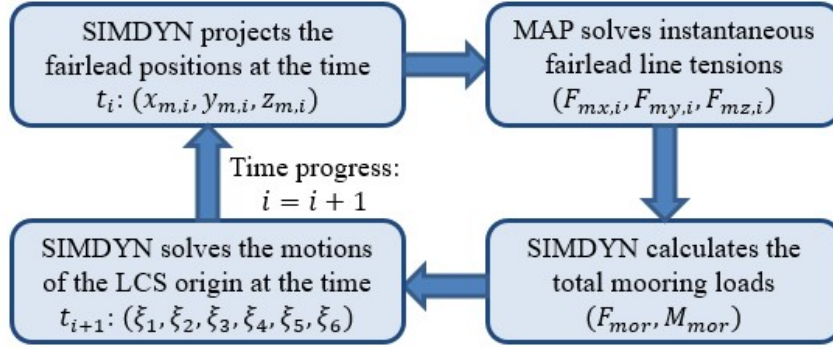
**Figure 4.4** Coupling of SIMDYN and MAP++

$(F_{mx,i}, F_{my,i}, F_{mz,i})$ denotes the instantaneous fairlead forces on the mooring line No. $i$ and $x_{m,i}$ denotes the fairlead position of the mooring line No. $i$. The fairlead positions under certain rotation angle are projected from the origin $(\xi_1, \xi_2, \xi_3)$ of the body coordinate system:

$$x_{m,i} = \xi + R^T x'_{m,i} \qquad (4.1)$$

$x'_{m,i}$ are the fairlead positions in the body coordinate system. For the rotational motions, the contributions from the mooring system can be represented by the mooring restoring arm. The quasi-static mooring modelling in MAP++ neglects the dynamics of the mooring lines (Masciola et al., 2013, Hall and Goupee 2015). Under this assumption, the mooring restoring curves can be calculated from the forced rotation tests. The forced rotation tests use the specified (forced) rotation time history to study the mooring moments at the specified rotation angles. Figure 4.4 shows the pitch motion time history and the mooring pitch moment time history in the forced rotation tests. The total mooring moments $M_{mor}$ are calculated as:

$$M_{mor} = \sum_{i=1}^{NL} x_{m,i} \times F_{m,i} \tag{4.2}$$
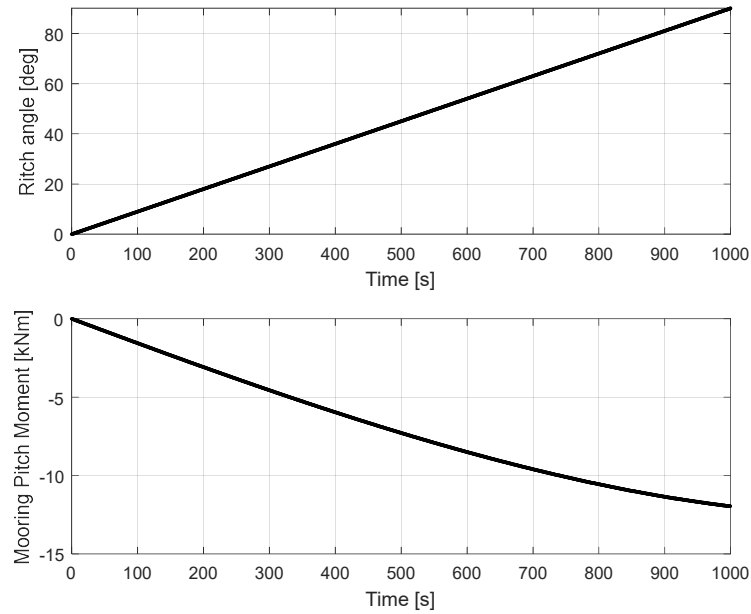


**Figure 4.5** Forced rotation tests

The restoring arm (unit: m) is defined as the ratio between the restoring moment (unit: N·m) to the displacement (unit: N). Therefore, the mooring restoring arm is:

$$L_{mor} = M_{mor}/(Mg) \tag{4.3}$$

Through the forced rotation tests in SIMDYN and MAP++, the mooring restoring arm can be approximated (see Figure 4.5). The mooring restoring arm (if applicable) will be added to the original (without the mooring system) restoring arm of the floating structure.
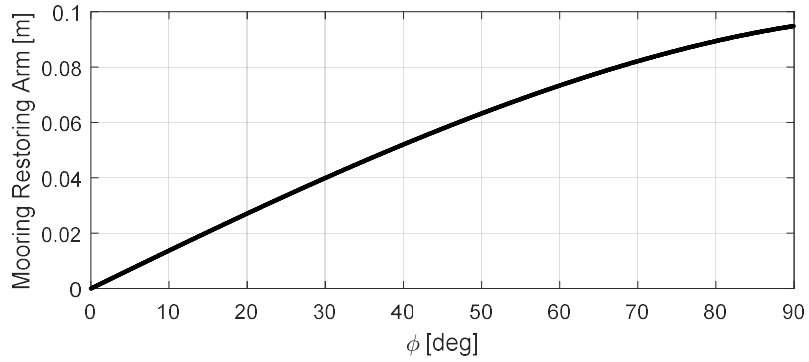
**Figure 4.6** Mooring restoring arm

The original restoring arm (the black line in Figure 4.6) comes from the hydrostatic moment and can be calculated using the various methods in traditional naval architecture. In Figure 4.6, the circle dot line represents the total restoring arm with the single line mooring system and the square dot line represents the total restoring arm with the 3-leg mooring system.
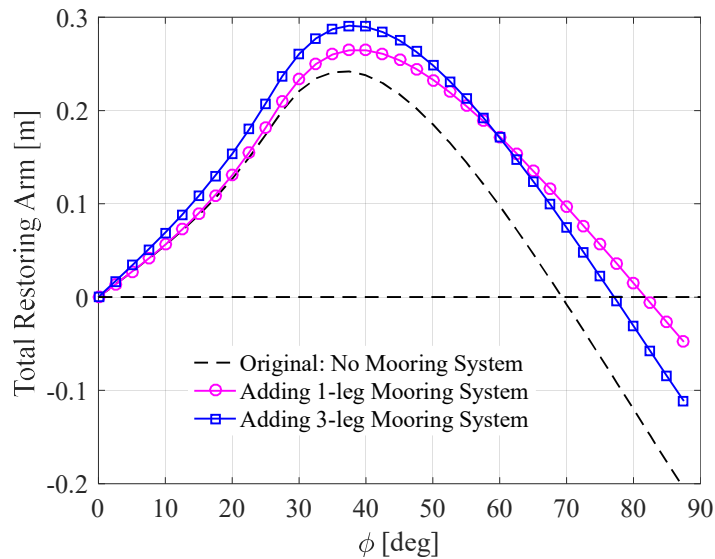


**Figure 4.7** Restoring arm of the floating cylinder

The total restoring arms can be fitted using the least square method using polynomials of different orders. In practice, the eleventh-order polynomial fitting yields the reasonable accuracy required (see Figure 4.7). The eleventh-order polynomial used to fit the restoring arms is:

$$RA\_fit(x) = C_1 \cdot x + C_3 \cdot x^3 + C_5 \cdot x^5 + C_7 \cdot x^7 + C_9 \cdot x^9 + C_{11} \cdot x^{11} \quad (4.4)$$
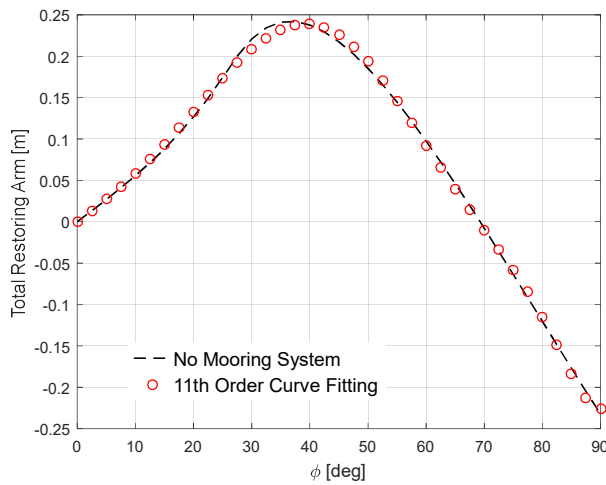


(a) No mooring leg

(95% confidence bounds):

$C_1 = 0.3108 \ (0.283, 0.339)$

$C_3 = 0.8476 \ (0.664, 1.031)$

$C_5 = -2.437 \ (-2.833, -2.042)$

$C_7 = 2.047 \ (1.681, 2.412)$

$C_9 = -0.7471 \ (-0.898, -0.597)$

$C_{11} = 0.101 \ (0.0783, 0.124)$
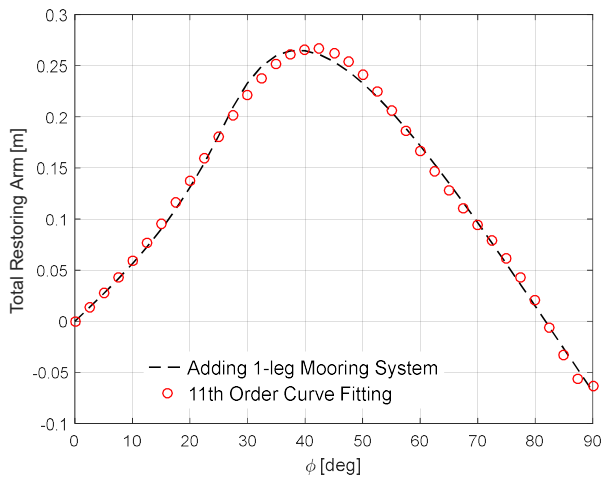


(b) single mooring leg (95% confidence bounds):

$C_1 = 0.3125 \ (0.284, 0.341)$

$C_3 = 0.9344 \ (0.751, 1.118)$

$C_5 = -2.461 \ (-2.857, -2.065)$

$C_7 = 2.048 \ (1.682, 2.414)$

$C_9 = -0.7466 \ (-0.897, -0.596)$

$C_{11} = 0.1009 \ (0.0782, 0.124)$

**Figure 4.8** Curve fitting of the restoring arms
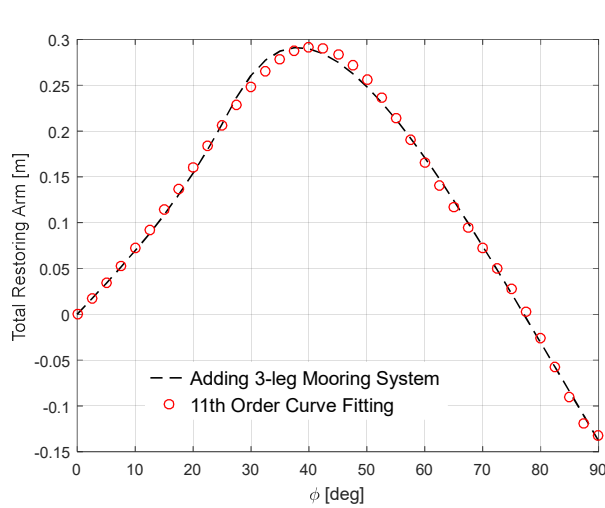
(c) three mooring legs

(95% confidence bounds):

$C_1 = 0.3896 \ (0.361, 0.418)$

$C_3 = 0.8383 \ (0.655, 1.022)$

$C_5 = -2.436 \ (-2.832, -2.039)$

$C_7 = 2.046 \ (1.68, 2.413)$

$C_9 = -0.7473 \ (-0.899, -0.596)$

$C_{11} = 0.1011 \ (0.0782, 0.124)$

**Figure 4.9** Continued

The fitting coefficients obtained are required for both the Melnikov approach in subsection 4.2 and the Markov approach in subsection 4.3.

## 4.2. The Melnikov Approach

The Melnikov method was originally introduced for regular wave excitation (Falzarano, 1990) and subsequently extended to random excitation (Su 2012, Somayajula 2017). Using this approach, capsizing can be related to an escaping trajectory from the safe region (of the phase space plane) to the unsafe region (of the phase space plane). Therefore, the phase flux rate can be used as a criterion for capsizing risks. The moored floating cylindrical system in this study is a new scenario for the Melnikov approach. It is different from the ship in that the mooring system contributes additional restoring arm and that the forward speed effects are no longer concerned. The following is the essential derivation of the Melnikov approach for the floating structure with its total restoring moment (arm) described by an 11th-order polynomial.

The original, decoupled pitching equation is:

$$[I_{55} + A_{55}(\omega)]\ddot{\xi}_5 + B_{55}(\omega)\dot{\xi}_5 + B_{55q}(\omega)\dot{\xi}_5|\dot{\xi}_5|$$
$$+\Delta\left(C_1\xi_5 + C_3\xi_5{}^3 + C_5\xi_5{}^5 + C_7\xi_5{}^7 + C_9\xi_5{}^9 + C_{11}\xi_5{}^{11}\right) = f_5(t) \tag{4.5}$$

$\xi_5$ denotes the pitching angle. $I_{55}$ and $A_{55}(\omega)$ denote the pitch moment of inertia

and added moment of inertia, respectively. $B_{55}(\omega)$ and $B_{55q}(\omega)$ denote the linear and

quadratic damping, respectively. $\Delta$ denotes the displacement. $C_1$ through $C_{11}$ are the

coefficients for the pitch restoring moment (arm). $f_5(t)$ is the external excitation force.

Equation 4.5 can be non-dimensionalized to (Roberts, 1986):

$$\ddot{x} + b_1\dot{x} + b_2\dot{x}|\dot{x}| + \left(x + \frac{C_3}{C_1}x^3 + \frac{C_5}{C_1}x^5 + \frac{C_7}{C_1}x^7 + \frac{C_9}{C_1}x^9 + \frac{C_{11}}{C_1}x^{11}\right) = F_5(\tau) \tag{4.6}$$

Where the following non-dimensionalized coefficients are used:

$$x = \xi_5, \qquad \tau = \omega_n t, \qquad \omega_n = \sqrt{\frac{\Delta C_1}{I_{55} + A_{55}(\omega)}}$$
$$b_1 = \frac{B_{55}(\omega)}{\Delta C_1}\omega_n, \qquad b_2 = \frac{B_{55}}{I_{55} + A_{55}(\omega)}, \qquad F_5(\tau) = \frac{f_5(t)}{\Delta C_1} \tag{4.7}$$

Compared with the stiffness coefficients, the pitch damping coefficients are small

(Haslum, 2000). Equation 4.6 can be rescaled using the perturbation parameter $\varepsilon$, but that

does not mean that the absolute amplitude of the excitation is small. For the convenience

of perturbation analysis, $b_1$ is set as $\varepsilon b_{1\varepsilon}$, $b_2$ is set as $\varepsilon b_{2\varepsilon}$, $F_5$ is set as $\varepsilon F_{5\varepsilon}$. Equation 4.6

can be written in the state space format:

$$\begin{cases} \dot{x}(\tau) = y(\tau) \\ \dot{y}(\tau) = -x(\tau) - \frac{C_3}{C_1}x^3(\tau) - \frac{C_5}{C_1}x^5(\tau) - \frac{C_7}{C_1}x^7(\tau) - \frac{C_9}{C_1}x^9(\tau) - \frac{C_{11}}{C_1}x^{11}(\tau) \\ \quad +\varepsilon[-b_{1\varepsilon}y(\tau) - b_{2\varepsilon}y(\tau)|y(\tau)| + F_{5\varepsilon}(\tau)] \end{cases} \tag{4.8}$$

The solution for equation 4.8 can be given numerically. When no damping and no excitation is applied, $\varepsilon = 0$.
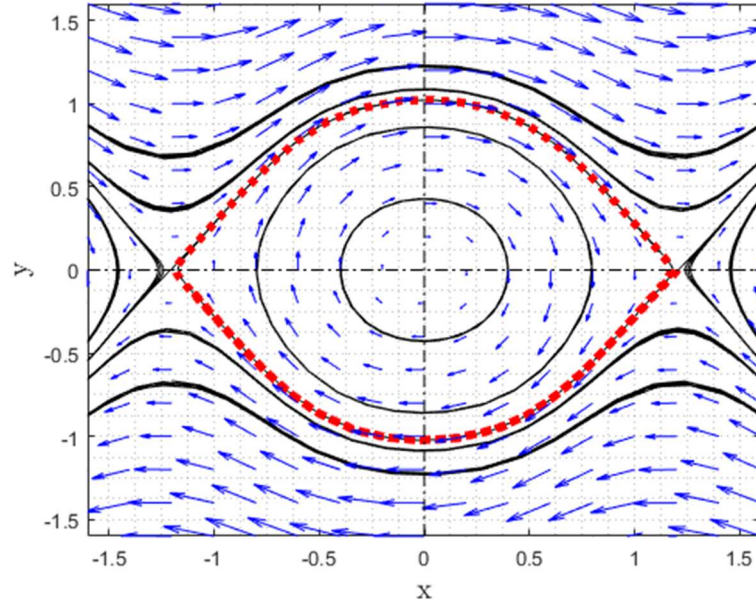


**Figure 4.10** Phase plane for undamped and unforced system

Figure 4.8 shows the phase plane for an undamped and unforced system with the 11-order restoring curve. The phase plane in Figure 4.8 is formed by a center at the origin and two saddles connected by heteroclinic orbits. The stable region is bounded by the dotted curve. If $x_0(\tau)$ and $y_0(\tau)$ denote the separatrices of the system in absence of damping or excitation, based on the definition by Wiggins (2003), the Melnikov function for the damped and forced system is:

$$\overline{M} + \widetilde{M}(\tau_0) = \int_{-\infty}^{\infty} y_0(\tau)[-b_{1\varepsilon}y_0(\tau) - b_{2\varepsilon}y_0(\tau)|y_0(\tau)| + F_{5\varepsilon}(\tau + \tau_0)]\, d\tau \quad (4.9)$$

$\overline{M}$ is the constant component of the Melnikov function, which corresponds to the damping contribution:

$$\overline{M} = \int_{-\infty}^{\infty} y_0(\tau)[-b_{1\varepsilon}y_0(\tau)-b_{2\varepsilon}y_0(\tau)|y_0(\tau)|]\, d\tau \qquad (4.10)$$

$\widetilde{M}(\tau_0)$ is the oscillating component of the Melnikov function, which corresponds to the excitation contribution.

$$\widetilde{M}(\tau_0) = \int_{-\infty}^{\infty} y_0(\tau)F_{5\varepsilon}(\tau + \tau_0)\, d\tau = \int_{-\infty}^{\infty} y_0(\tau_0 - \tau)F_{5\varepsilon}(\tau)\, d\tau \qquad (4.11)$$

The Melnikov function describes the phase space flux corresponding to a trajectory "escaping" from the safe region (bound) to the unsafe (unbounded-capsizing) region. The amount of phase space flux is related to the area of "lobes" formed where the safe region is inside the unsafe region (Jiang et al., 2000). According to Hsieh et al. (1994), the (two period average) rate of phase space flux is:

$$\Phi = \lim_{T\to\infty} \frac{1}{2T} \int_{-T}^{T} M^+ d\tau_0 \qquad (4.12)$$

$\Phi$ is the average rate of the phase space flux through both bounds of the heteroclinic orbits. $M^+(\tau_0)$ represents the positive part of the Melnikov function, which transfers the phase space out of the safe region. Figure 4.9 highlights the positive part of Melnikov function (shaded). When the Melnikov function is constantly negative, the stable manifold will always enclose the unstable manifold. Under this condition, if the system starts from inside of safe region, it will stay stable (inside the safe region).

101
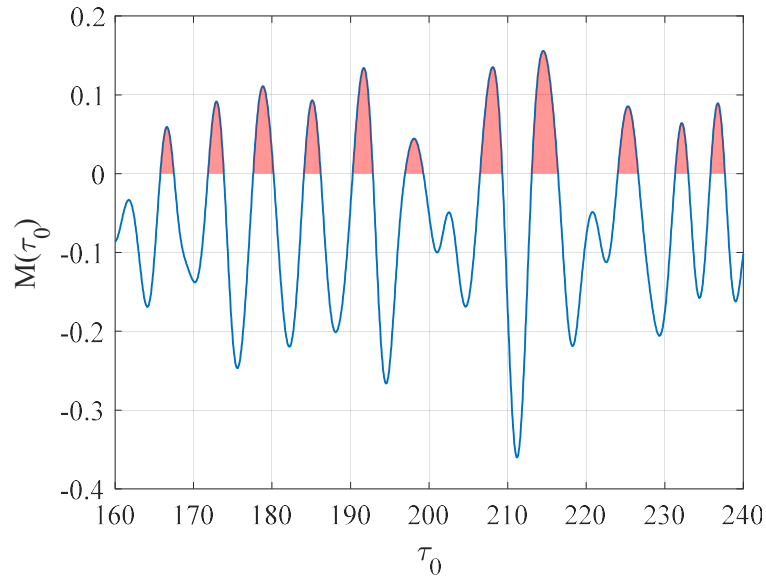
**Figure 4.11** Melnikov function time series

Figure 4.10 shows two representative situations of the Melnikov function. When the excitation force is small ($H_S = 1.0m$), the Melnikov function is below zero as shown in Figure 4.10 (a). This means that there is no phase space transport from the safe region. When the excitation force is higher ($Hs = 3.0m$), considerable phase transport flux is produced as shown in Figure 4.10 (b). Under this condition, even if the system starts from the safe region, it is subjected to significant probability of capsizing.
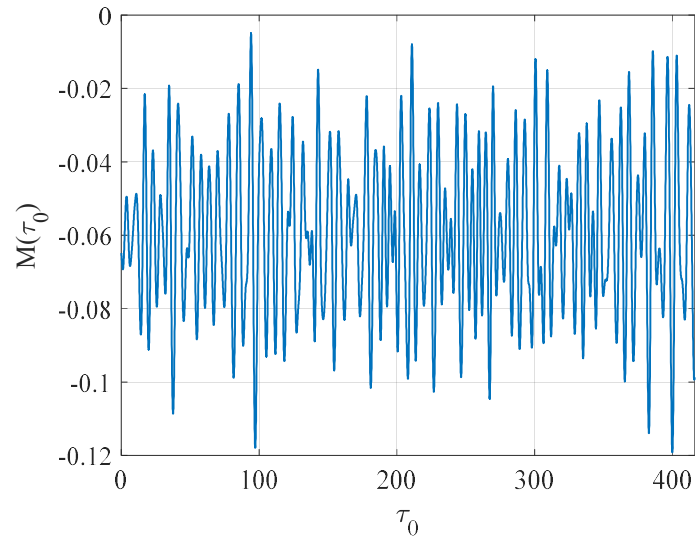
(a) $H_S=0.5m$, $Tp=7.0s$
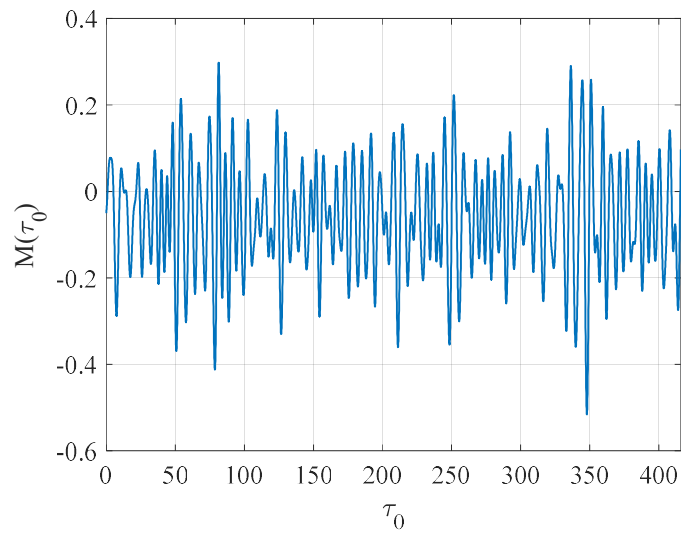


(b) $H_S=3.0m$, $Tp=7.0s$

**Figure 4.12** Time series of Melnikov function

The Melnikov process assumes an ergodic and stationary Gaussian process. Therefore, the average phase space flux rate can be calculated as (Somayajula and Falzarano, 2019):

103

$$\Phi = E\left[\left(\overline{M} + \tilde{M}(\tau_0)\right)^+\right] = \int_{-\overline{M}}^{\infty}(x + \overline{M})\,p(x)dx \qquad (4.13)$$

$p(x)$ represents the probability density function of a standard Gaussian distrition and $P(x)$ represents the cumulative distribution function of a standard Gaussian distribution:

$$p(x) = \frac{1}{\sqrt{2\pi}}e^{-\frac{1}{2}x^2} \qquad (4.14)$$

Figure 4.11 shows the variation of the phase space flux rate with significant wave height under different peak periods ($b_1 = 0.02$, $b_2 = 0.02$).
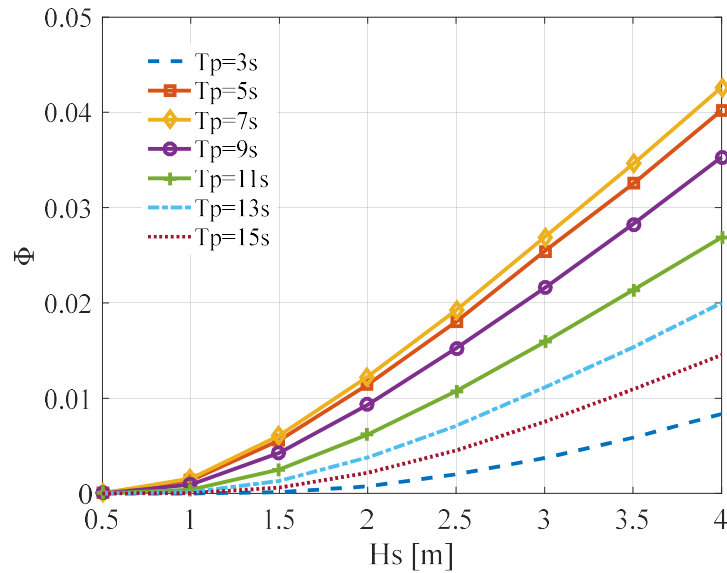


**Figure 4.13** Variation of the phase space flux rate with $H_S$

It is quite natural that the probability of capsizing increases with the significant wave height. The "hardening" behavior of the phase space flux rate indicates considerable increase of capsizing risk as wave height increases.

Figure 4.12 shows the variation of the phase space flux rate with peak period under different significant wave heights ($b_1 = 0.02$, $b_2 = 0.02$). The peak of the phase space flux rate appears around Tp $\approx$ 6.0s (the natural period of pitching is around 5.5s).
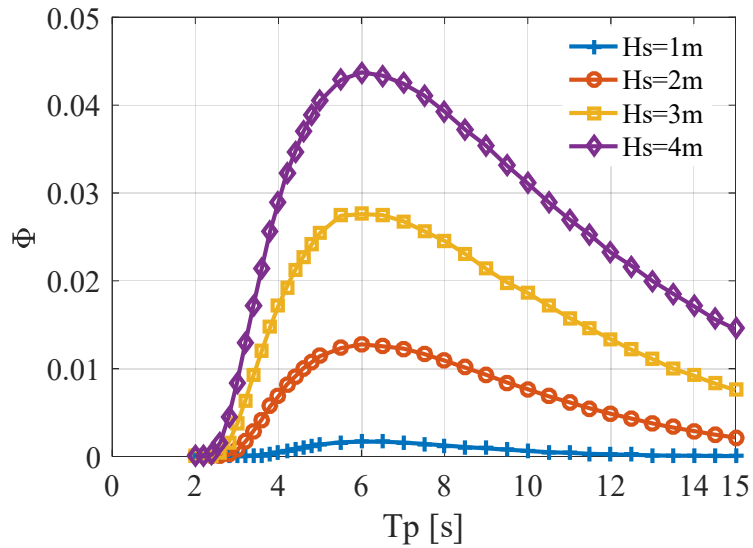


**Figure 4.14** Variation of the phase space flux rate with Tp

Figure 4.13 shows the variation of the phase space flux rate with significant wave height under different linear damping coefficients ($Tp = 7$s, $b_2 = 0.02$). The linear damping coefficient has considerable effect of reducing the probability of capsizing.
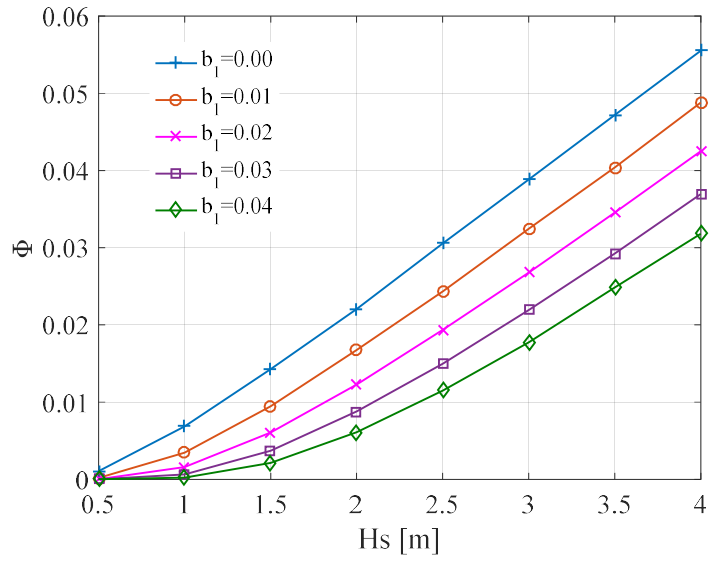
**Figure 4.15** Variation of the phase space flux rate under different $b_1$

Figure 4.14 shows the variation of the phase space flux rate with significant wave height under different quadratic damping coefficients ($Tp = 7$s, $b_1 = 0.02$).
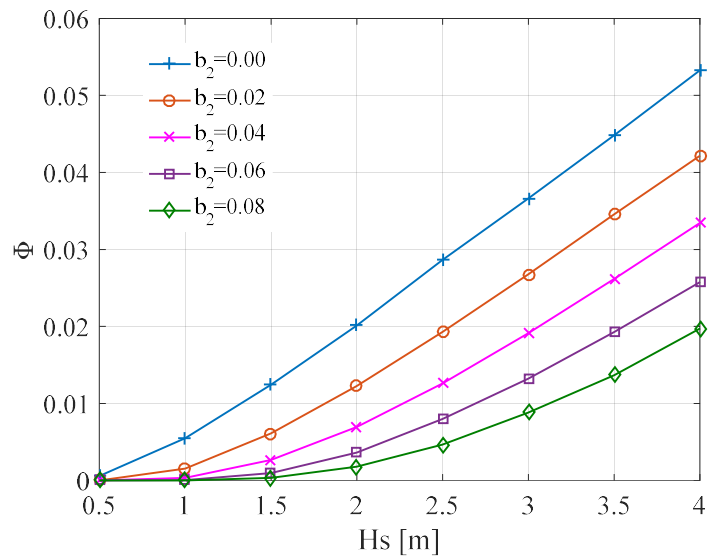


**Figure 4.16** Variation of the phase space flux rate under different $b_2$

The quadratic damping coefficients yield similar (to the linear damping) effect of reducing the probability of capsizing.

Figure 4.15 shows the variation of the phase space flux rate with significant wave height under different mooring systems ($Tp = 7\text{s}, b_1 = 0.02, b_2 = 0.02$). The addition of the mooring system does not seem to influence the probability of capsizing significantly. It seems that the Melnikov approach is not as sensitive to the restoring curves as the Markov approach, which will be shown in the next subsection.
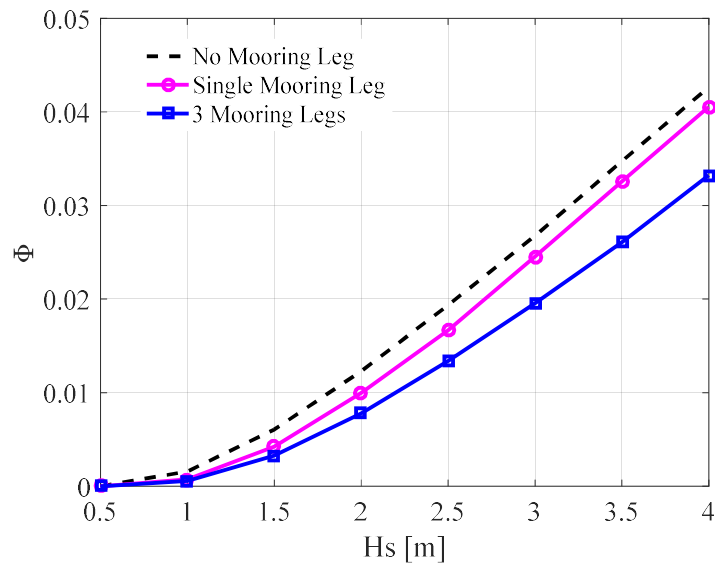


**Figure 4.17** Variation of the phase space flux rate under different mooring systems

## 4.3. The Markov Approach

For decades, the Markov approach has been applied to the nonlinear oscillations (see e.g. Roberts, 1982; Roberts and Spanos, 1986; Roberts and Vasta, 2000; Roberts and

Vasta, 2001; Roberts and Vasta, 2002). Using the stochastic averaging of the system's energy, the two dimensional (motion and velocity) pitching model is reduced to a one dimensional model of energy. This model can be approximated as a Markov process, for which the mean first time to capsize can be solved numerically by solving a Fokker Planck Equation (FPE). The approach works under the assumption that the wave spectrum is narrow-banded.

Recall the non-dimensionalized equation 4.5 in the derivation of the Melnikov approach. Following the derivation (Su 2012) convention, a similar perturbation is conducted using $\varepsilon^2$:

$$
\ddot{x}(\tau) + \varepsilon^2 b_{1\varepsilon^2} \dot{x}(\tau) + \varepsilon^2 b_{2\varepsilon^2} \dot{x}(\tau)|\dot{x}(\tau)| + x(\tau) + \frac{C_3}{C_1} x^3(\tau)
$$
$$
+ \frac{C_5}{C_1} x^5(\tau) + \frac{C_7}{C_1} x^7(\tau) + \frac{C_9}{C_1} x^9(\tau) + \frac{C_{11}}{C_1} x^{11}(\tau) = \varepsilon F_{5\varepsilon}(\tau) \tag{4.15}
$$

The total energy for the system, $E(\tau)$, consists of two parts: the kinetic energy and the potential energy:

$$
E(\tau) = \frac{\dot{x}^2}{2} + U(x) \tag{4.16}
$$

The potential energy, $U(x)$, can be obtained by integrating the restoring arm:

$$
U(x) = \int_0^x (\delta + \frac{C_3}{C_1} \delta^3 + \frac{C_5}{C_1} \delta^5 + \frac{C_7}{C_1} \delta^7 + \frac{C_9}{C_1} \delta^9 + \frac{C_{11}}{C_1} \delta^{11}) d\delta \tag{4.17}
$$

For the floating cylinder defined in Table 4.1, the stability (restoring arm) vanishes at 1.21 rad (69.3 degree, see Figure 4.7 (a)). Therefore, the initial energy ranges in [0, 0.53]. Different initial energy corresponds to different angle of vanishing stability as shown in Figure 4.16.
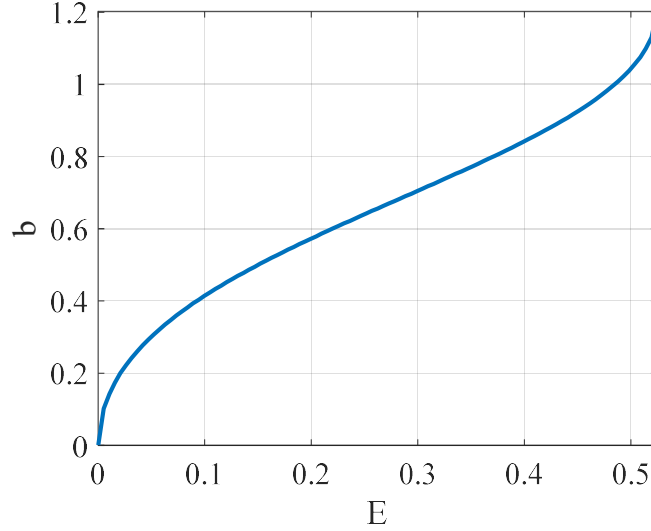
**Figure 4.18** Angle of vanishing stability versus the initial energy

In the absence of excitation and damping, the total energy $E(\tau)$ is conserved. The total energy $E(\tau)$ and phase angle $\varphi(\tau)$ satisfy:

$$sgn(x)\sqrt{U(x)} = \sqrt{E}cos\varphi, \qquad \dot{x} = -\sqrt{2E}sin\varphi \tag{4.18}$$

The Markov process of $E(\tau)$ can be described by a stochastic differential equation:

$$dE(\tau) = m(E)dt + \sqrt{D(E)}dB \tag{4.19}$$

$m(E)$ is the drift coefficient, $D(E)$ is the diffusion coefficient. The drift coefficient and diffusion coefficient can be obtained as (Roberts and Vasta, 2000):

$$m(E) = -\varepsilon^2 \Lambda_1(E) + \frac{1}{2}\pi \sum_{n=1}^{N_f}(s_n^2 + c_n^2)S_{FF}(n\omega(E_0)) \tag{4.20}$$

$$D(E) = -2\pi E_0 \sum_{n=1}^{N_f} s_n^2 \, S_{FF}(n\omega(E_0)) \tag{4.21}$$

109

$\Lambda_1(E)$ is the dissipation term. $S_{FF}$ is the power spectrum density of the excitation force $F_5(\tau)$. $\omega(E_0)$ is the angular frequency corresponding to the period $T(E_0)$ of the unperturbed oscillation. $N_f$ is the number of Fourier coefficients used to expand the solution. Practically, the study used $N_f = 5$, which achieved a reasonable approximation. $s_n$ and $c_n$ are the Fourier coefficients to expand the solution for the phase angle $\varphi_0(\tau)$, which satisfies:

$$\begin{aligned}
sin\varphi_0 &= -\frac{y_0(\tau)}{\sqrt{2E_0}} = \sum_{n=1}^{N_f} s_n \, sin[n\omega(E_0)] \\
cos\varphi_0 &= \frac{sgn(x)\sqrt{U(x)}}{\sqrt{E_0}} = \sum_{n=1}^{N_f} c_n cos[n\omega(E_0)]
\end{aligned} \tag{4.22}$$
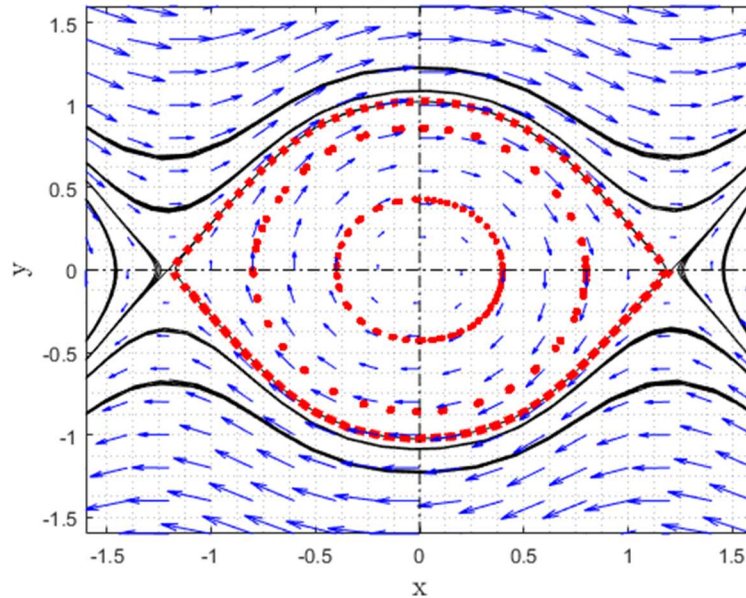


**Figure 4.19** Phase plane for undamped and unforced system

The separatrices of the unperturbed system without damping or excitation have been plotted as the dotted curves (starting with different initial energy $E_0$) in Figure 4.17. The Fourier expansion fitting for the phase angle $\varphi_0(\tau)$ at $E = 0.53$ is plotted in Figure 4.18, showing that using $N_f = 5$ is usually accurate enough.
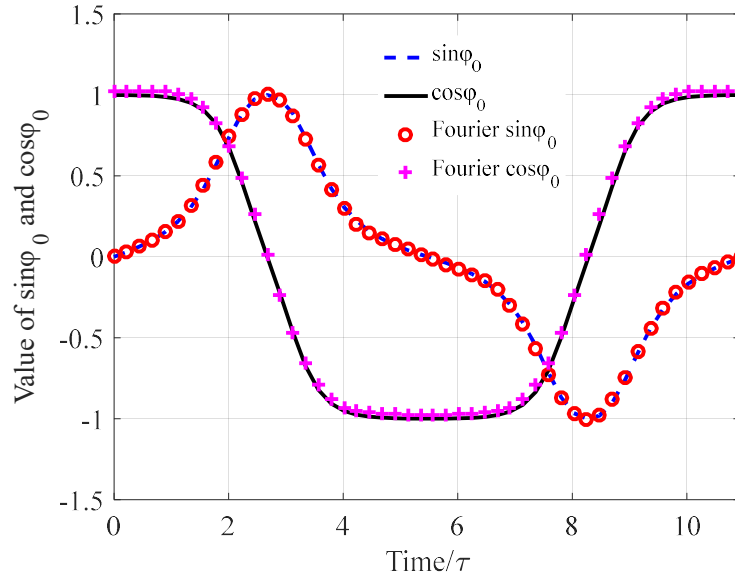


**Figure 4.20** Fourier expansion fitting for the phase angles

$\Lambda_1(E)$ is obtained by averaging over the period $T(E_0)$ of the unperturbed system:

$$\begin{aligned}
\Lambda_1(E) &= \frac{2E}{T(E_0)} \oint (b_{1\varepsilon^2} + b_{2\varepsilon^2}|y_0(\tau)|)sin^2\varphi_0 dt \\
\Lambda_2(E) &= -\frac{1}{T(E_0)} \oint (b_{1\varepsilon^2} + b_{2\varepsilon^2}|y_0(\tau)|)sin\varphi_0 cos\varphi_0 dt
\end{aligned} \tag{4.23}$$

The drift and diffusion coefficients obtained are plotted in Figure 4.19 through Figure 4.23. Parameters including the significant wave height, the peak period, the linear damping, the quadratic damping and the mooring system have been varied to demonstrate

111

their effects on the drift and diffusion coefficients. Neither the linear damping nor the quadratic damping will affect the diffusion coefficients.
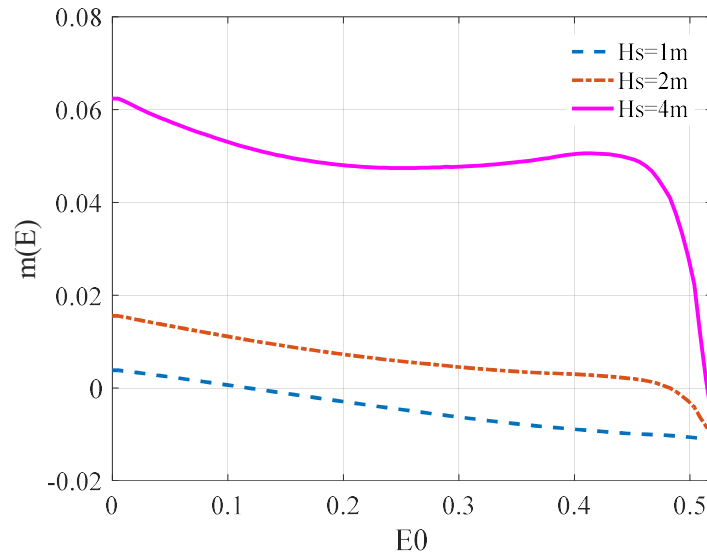


(a) Drift coefficient
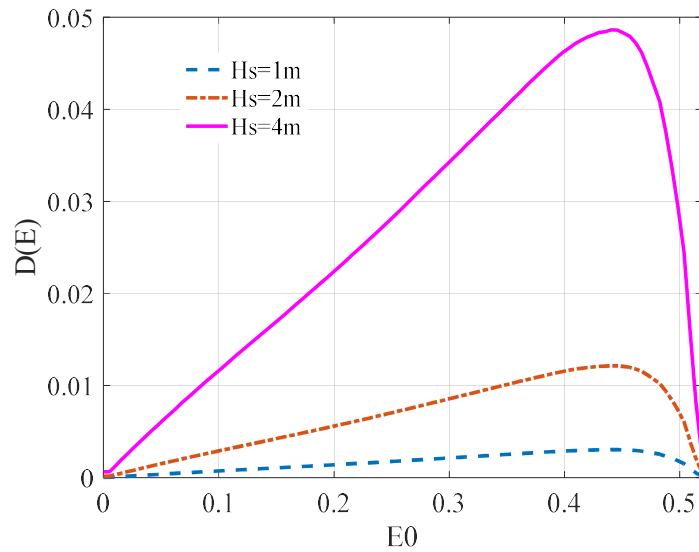


(b) Diffusion coefficient

**Figure 4.21** Drift and diffusion coefficients variation with Hs (Tp=7.0s, $b_1$=0.02, $b_2$=0.02)
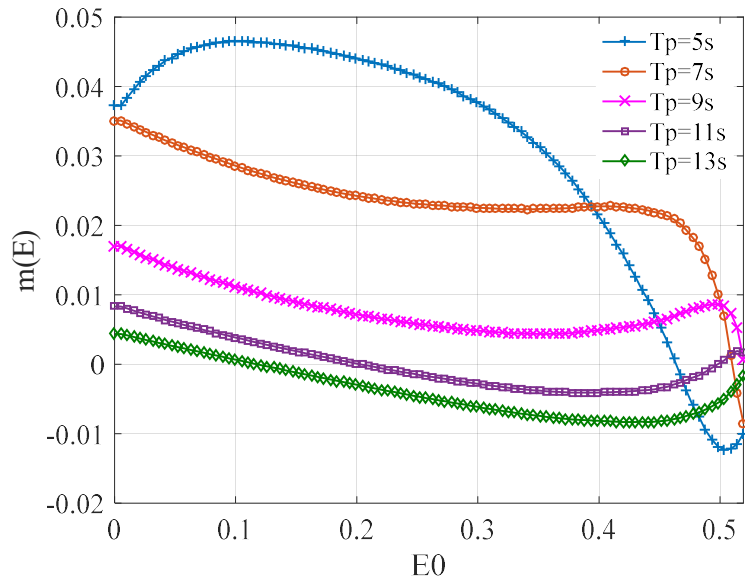
(a) Drift coefficient
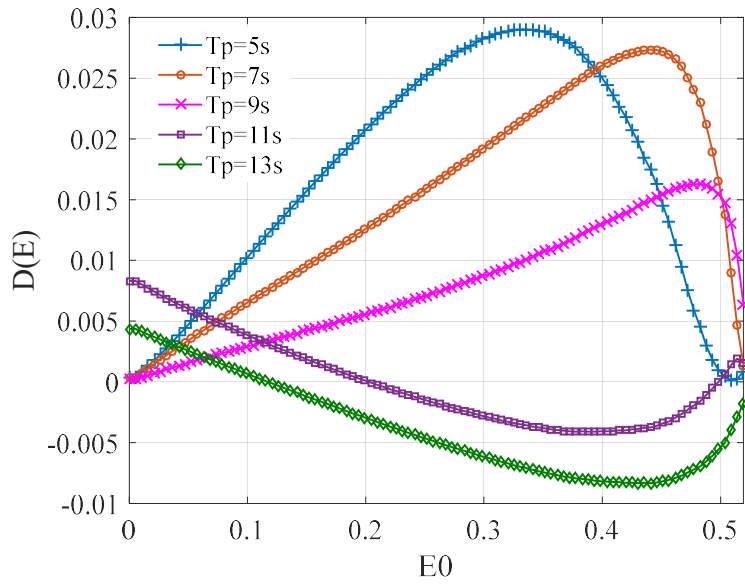


(b) Diffusion coefficient

**Figure 4.22** Drift and diffusion coefficients variation with Tp ($H_S$=3.0m, $b_1$=0.02, $b_2$=0.02)

113
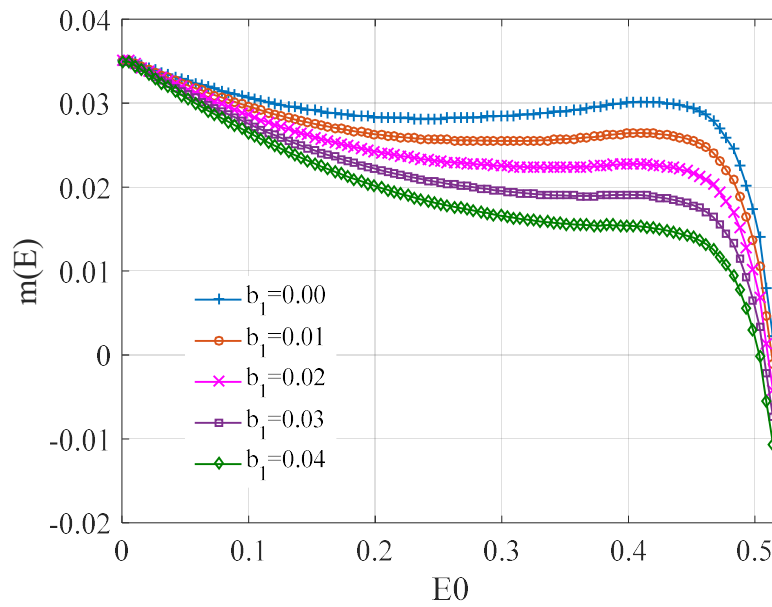
**Figure 4.23** Drift coefficients variation $b_1$ (Hs=3.0m, Tp =7.0s, b2=0.02)
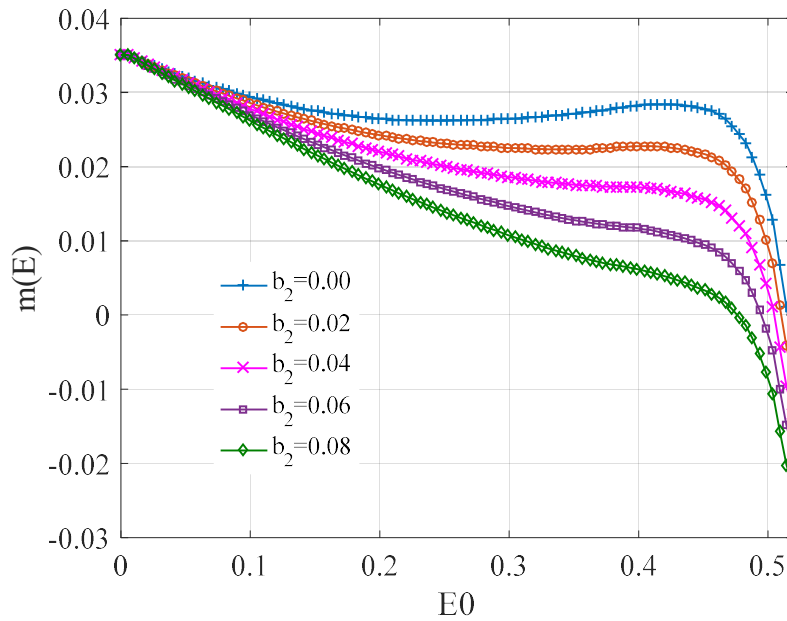


**Figure 4.24** Diffusion coefficients variation with $b_2$ (H$_S$=3.0m, Tp =7.0s, $b_1$=0.02)
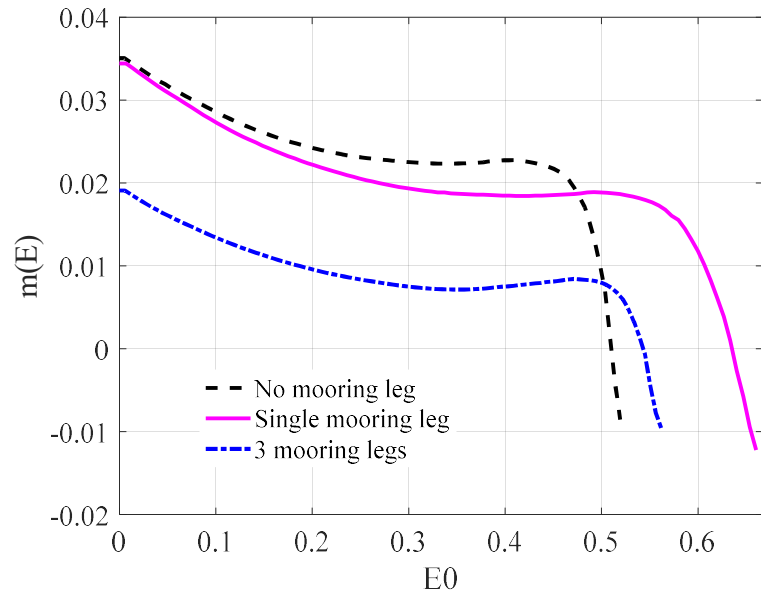
(a) Drift coefficient
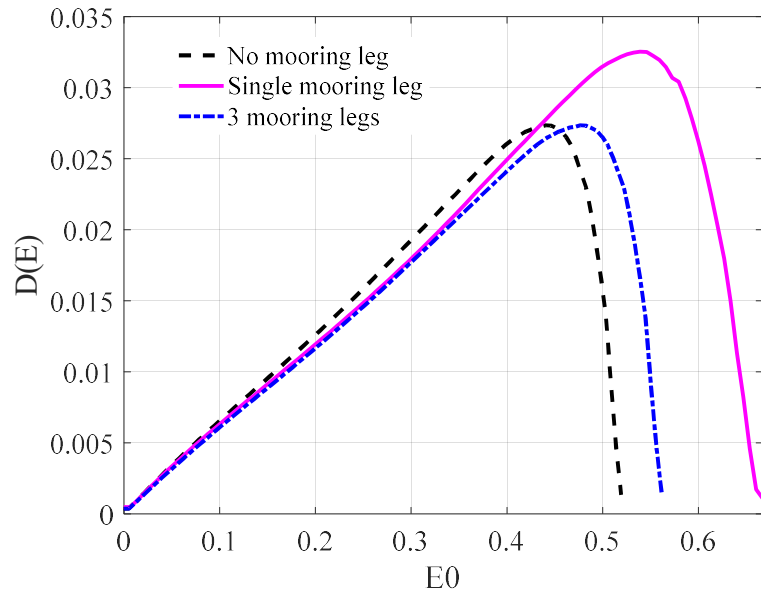


(b) Diffusion coefficient

**Figure 4.25** Drift and diffusion coefficients variation with mooring ($H_S$=3.0m, Tp=7.0s, $b_1$=0.02, $b_2$=0.02)

As the total energy $E(\tau)$ is a Markov process, the mean first passage (to cross the stable boundary with the initial energy $E_0$) time, $M_1(E_0)$, satisfies the generalized Pontryagin equation:

$$1 + m(E_0)\frac{d}{dE_0}M_1(E_0) + \frac{1}{2}D(E_0)\frac{d^2}{dE_0{}^2}M_1(E_0) = 0 \qquad (4.24)$$

In this study, equation 4.24 can be solved with two boundary conditions:

$$\begin{cases} M_1(E_c) = 0 \\ \dfrac{dM_1(0)}{dE_0} = -\dfrac{1}{\pi S_{FF}(\omega_n)} \end{cases} \qquad (4.25)$$

$E_c$ is the maximum initial energy for the system to remain in the safe basin (i.e., the outer-most dotted curve in Figure 4.17. $E_c$ corresponds to immediate capsizing $(M_1(E_c) = 0)$. $\omega_n$ represents the pitch natural frequency.
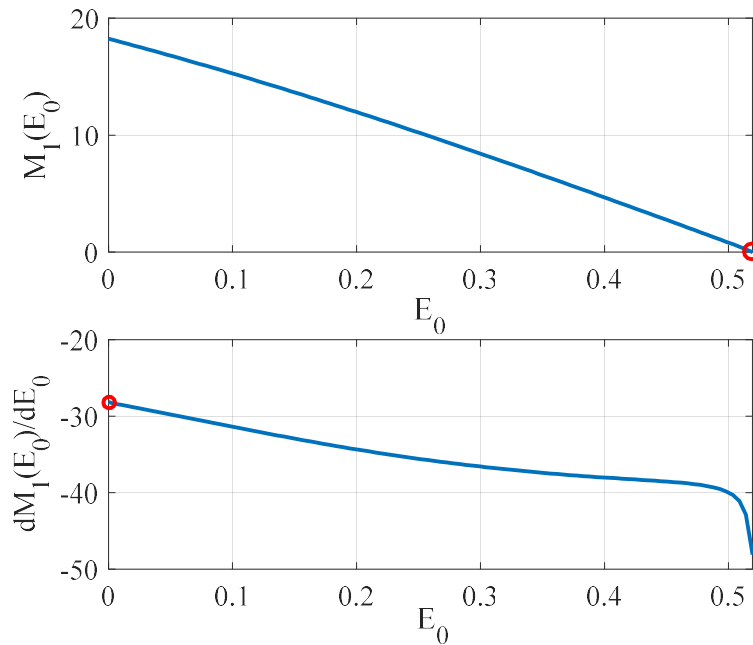


**Figure 4.26** The mean first passage time with initial energy ($H_S$=3.0m, $T_p$=7.0s)

Equation 4.24 can be solved numerically using the shooting method. The variation of $M_1$ and $dM_1(0)/dE_0$ are plotted in Figure 4.24. The mean first passage time $M_1$ decays with the initial energy $E_0$. The inverse of the mean first passage time is $1/M_1(0)$, namely the mean first escape rate. For this case $1/M_1(0)$ is 0.055, which can be compared with the phase space flux rate calculated by the Melnikov approach.
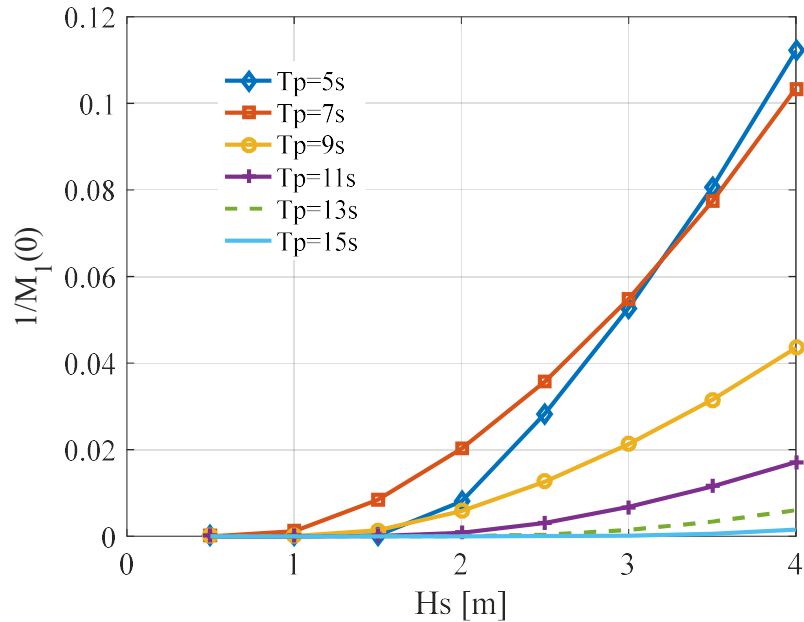


**Figure 4.27** Variation of the mean first escape rate with $H_S$

Figure 4.25 shows the variation of the mean first escape rate with significant wave height under different peak periods ($b_1 = 0.02, b_2 = 0.02$). Compared with the results from the Melnikov approach, the results from the Markov approach yield similar

increasing trend (with the significant wave height) as well as the similar "increasing slope" pattern.

Figure 4.26 shows the variation of the mean first escape rate with peak period under different significant wave heights ($b_1 = 0.02, b_2 = 0.02$). The peak of the mean first escape rate is approximately Tp≈5.5s (the pitch natural period is around 5.5s).
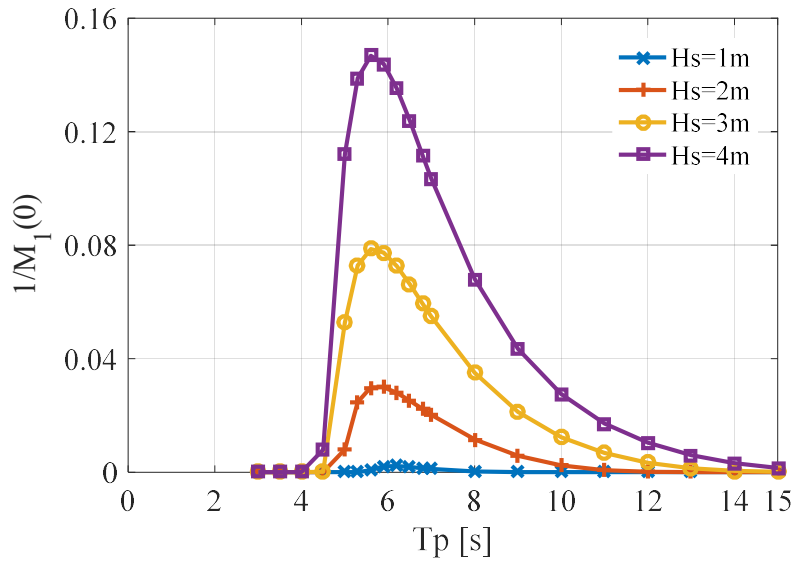


**Figure 4.28** Variation of the mean first escape rate with Tp

Figure 4.27 shows the variation of the mean first escape rate with significant wave height under different linear damping coefficients ($Tp = 7s, b_2 = 0.02$). The results from the Markov approach seem to be less sensitive to the linear damping as compared with the Melnikov approach.
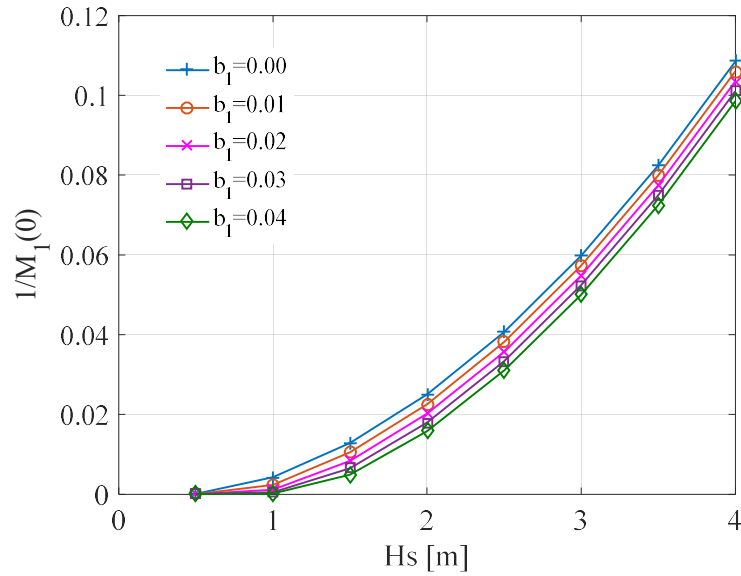
**Figure 4.29** Variation of the mean first escape rate under different $b_1$

Figure 4.28 shows the variation of the mean first escape rate with significant wave height under different quadratic damping coefficients ($Tp = 7$s, $b_1 = 0.02$).
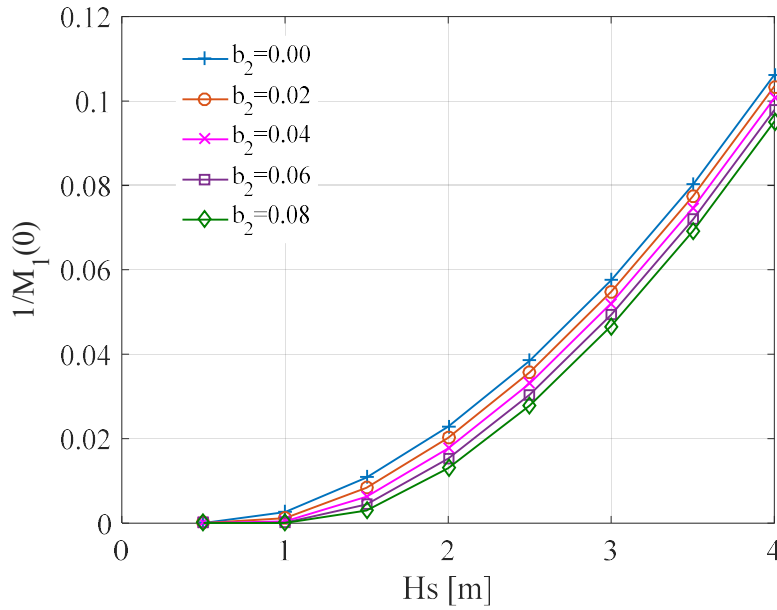


**Figure 4.30** Variation of the mean first escape rate under different $b_2$

The results from the Markov approach (in Figure 4.28) seem to be less sensitive to the quadratic damping compared with the Melnikov approach.
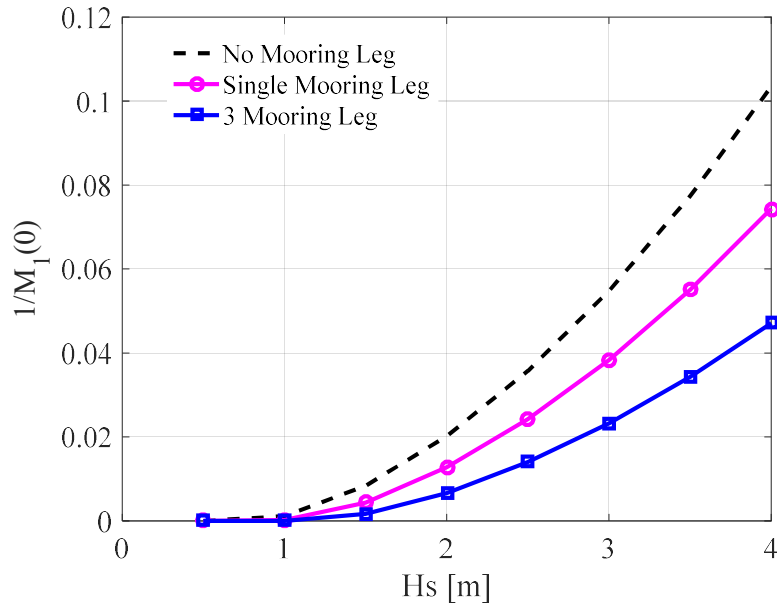


**Figure 4.31** Variation of the mean first escape rate under different mooring systems

Figure 4.29 shows the variation of the mean first escape rate with significant wave height under different mooring systems $(Tp = 7s, b_1 = 0.02, b_2 = 0.02)$ . The implementation of the mooring systems reduces the probability of capsizing, to different extent. Both the Melnikov results and the Markov results show that the specified single mooring leg system is not as helpful as the specified multiple (3) mooring leg system as for reducing the probability of pitchpoling. However, the Markov approach is obviously more sensitive than the Melnikov approach to the variation of the restoring curve.

Observations from the previous comparison seem to show that the Markov approach is more sensitive to the sea state parameters (i.e. significant wave height and

peak period). It is also more sensitive (than the Melnikov approach) to the restoring curves, while it is less sensitive (than the Melnikov approach) to the damping coefficients.

## 4.4. Comparison of Melnikov and Markov Approaches

The Melnikov approach and the Markov approach are valid under different assumptions. As semi-analytical methods, they both provide efficient measurements of the capsizing probability. The phase space flux rate from the Melnikov approach and the mean first escape rate from the Markov approach both indicate how "fast" the system loses its stability. Figure 4.30 shows the comparison between the Melnikov and the Markov approach under different peak periods. Though the magnitude of the metrics from the two approaches are not always close, depending on the input parameters, the phase space flux rate and the mean first escape rate yield similar trends in these sensitivity studies.
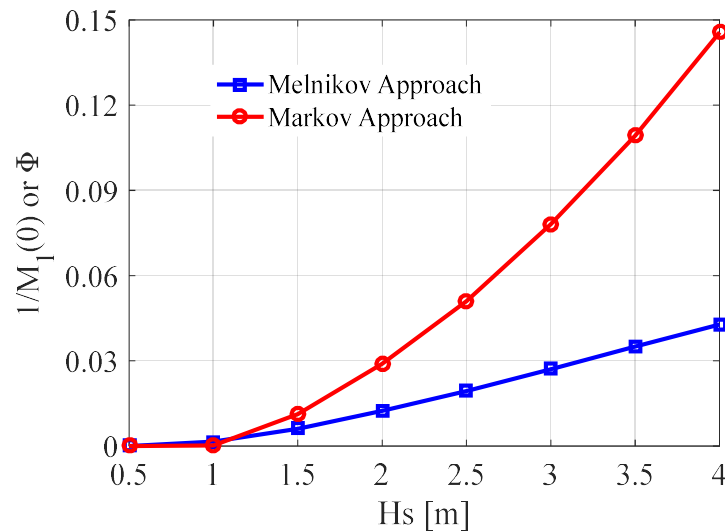


(a) Comparison of Melnikov and Markov approach when Tp=5.5s

**Figure 4.32** Comparison of Melnikov and Markov approach under different peak periods

121
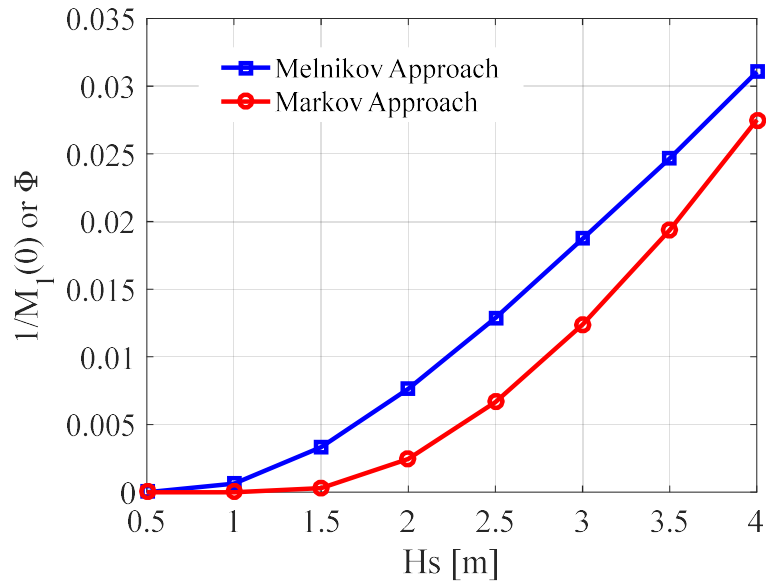
(b) Comparison of Melnikov and Markov approach  when Tp =10.0s

**Figure 4.33** Continued

Since both approaches assume small damping for the perturbation analysis, the effects of linear and quadratic damping coefficients on their correlations are studied. Figure 4.31 shows the relationship between phase space flux rate and the mean escape rate under different linear damping coefficients $b_1$ and nonlinear damping coefficients $b_2$. It can be found that the damping coefficients will affect the slope of the correlations considerably. Based on our previous analysis, the change in slope can be largely attributed to the fact that the Melnikov approach is relatively more sensitive to the damping coefficients.
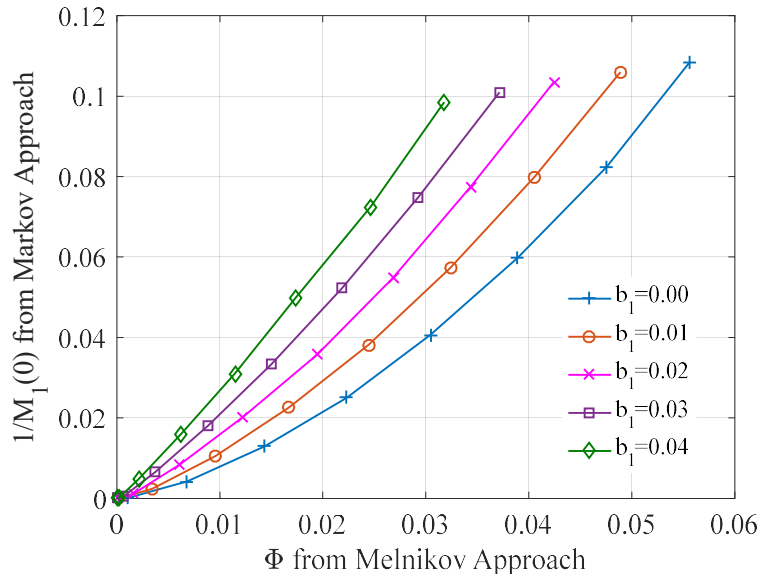
(a) Varied linear damping
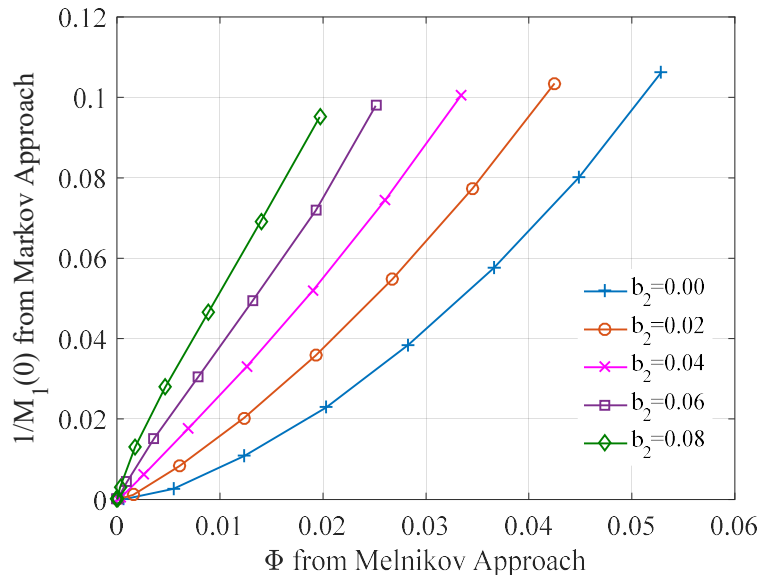


(b) Varied quadratic damping

**Figure 4.34** Relationship between phase space flux rate and the mean escape rate under different damping coefficients

Though the two metrics are not directly correlated, it is reasonable to consider them as "loosely" correlated. Under appropriate conditions (Melnikov: relative small damping and excitation; Markov: relative small bandwidth of the response and damping), either approach should give similar results. The applicability of their corresponding assumptions may also explain their slightly different sensitivity to the peak period.

Essentially, the Melnikov function considers the perturbations (which include the excitation and the damping) along the unperturbed heteroclinic boundary. A positive Melnikov function value means that the system is accumulating energy from the intersected heteroclinic boundary. On the other hand, the Markov approach solves the equation of the mean time for the system (starting from varied initial energy) to accumulate enough energy to exit the boundary of the safe region.
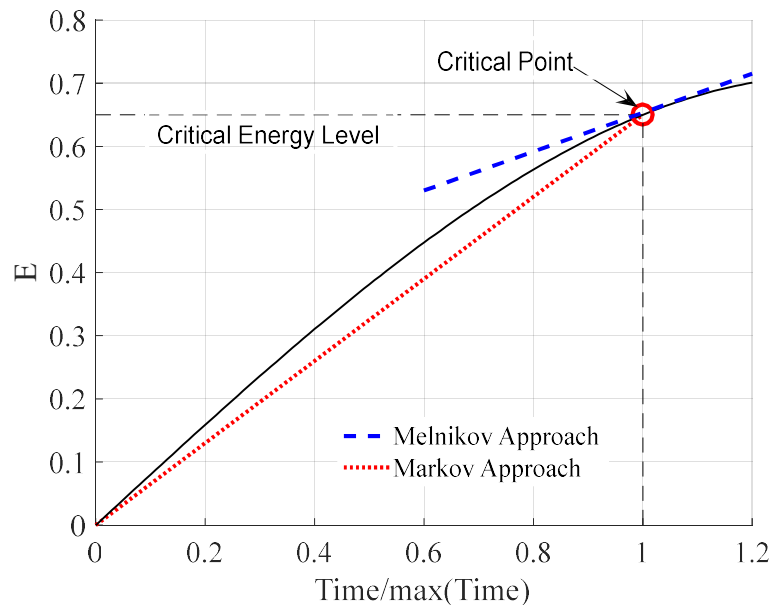


**Figure 4.35** A conceptual understanding of the two approaches

Figure 4.32 will help us understand conceptually (instead of quantitatively) the two approaches: the Markov approach measures the slope from the origin to the critical energy level, while the Melnikov approach measures the slope near/at the critical energy level.

# 5. CONCLUSIONS AND FUTURE EXTENSIONS

## 5.1. Conclusions

In the dissertation, the author explored various approaches to overcome the inadequacies/difficulties of the traditional methods (for typical ships and offshore platforms) in modelling the WES. As pointed out by the ECMW, the most important inadequacy/difficulty is associated with the nonlinear effects and viscous damping effects.

Though inclusion of all nonlinear effects is too aggressive for this dissertation, it's primarily important that the nonlinear effects in the equations of motion are addressed. In section 2, a simulation program, SIMDYN, was developed using both the linear and the blended time domain methods to predict the motions (six degrees of freedom) of the wave energy structure. The nonlinear Froude-Krylov and hydrostatic forces were implemented in SIMDYN. The (dominant) external forces can be calculated more accurately without costing much more calculation time. The nonlinear inertia effects were addressed, which were usually neglected in the time domain analysis. They may prove to be as important as the nonlinear effects from the external forces.

The study also filled the gap in that the blended method has seldom been correlated with WES model tests. The comparisons between the simulations and the model tests were improved by the blended method. The survival mode as well as the working mode (under large sea states) modelling of the (point absorber type) WES will benefit from the blended time domain method's more accurate motion predictions without increasing the

calculation time orders of magnitude of as would occur using a fully nonlinear time-domain program or a CFD program.

The other challenge pointed out by the ECMW is evaluating the important (more important for WES than for typical platforms) viscous damping values. As empirical formula or free decay test for WES are usually unavailable, the author introduced the system identification method to overcome this problem. Section 3 presents the first application of the R-MISO system identification technique to the model test correlation of a wave energy structure (a non-ship-shape geometry) with realistic mooring configurations. Compared to previous studies, the increased complexity of our modelling (6 or 3 degrees of freedom with catenary mooring modelling) is a significant progress in application of the R-MISO system identification as an advanced analysis methodology.

Using directly the model test results under random sea states (the realistic scenario), system identification can reveal the transfer function over the whole frequency range (instead of at just the natural frequency). A fitting between the transfer function from the model tests and the one from the simulations yields the reasonable viscous damping values. Implementing the damping correction obtained from the system identification method effectively improves the accuracy of the time domain simulations. It is shown that R-MISO can be applied to model test correlations of moored floating structures, which categorizes the majority of wave energy structures.

While many quantities of interest (e.g. mooring loads) can be studied through typical engineering design practice, the dynamic stability (capsizing under random excitation) is relatively, overlooked. Actually, increasing instability occurrence observed

in WES model test indicates that the dynamic stability is equivalently important. In section 4, two efficient semi-analytical approaches: the Melnikov approach and the Markov approach, were explored and compared to predict the pitchpoling probability of a generic moored floating cylinder (representative of the form of many WESs). Essentially, the Melnikov approach considers the perturbations along the unperturbed heteroclinic boundary and reveals how fast the system is accumulating energy from the intersected heteroclinic boundary. On the other hand, the Markov approach solves the equation of the mean time for the system (starting from varied initial energy) to accumulate enough energy to exit the boundary of the safe region.

The influence of the parameters, including the sea states, damping and mooring systems on the capsizing probability predictions, was studied. The Markov approach is more sensitive (than the Melnikov approach) to the sea states and the restoring curves, while it is less sensitive (than the Melnikov approach) to the damping coefficients. Though the derivations of the Melnikov approach and the Markov approach have been established previously, they have never been applied to a (non-ship-shape) moored floating structure before. These efforts will prove to be effective in predicting the dynamic instability of the moored floating system and in turn reduce the capsizing risks. By avoiding the otherwise long simulating time, both approaches works efficiently in optimizing the primary designs of hull geometries and mooring systems.

## 5.2. Future Recommendations

In the future studies, the blended time domain program should be benchmarked by more model test results. Influences from the power take off (PTO) forces should be

modelled in SIMDYN in the next phase. Other appealing aspects of possible improvement include simulating the parametric roll and sway accurately (and correlating with the model test measurements) and upgrading the mooring modelling to dynamic modelling. Overall, the blended time domain program has provided a good platform. On top of its realistic modelling capability, studies of improved hydrodynamic control can be implemented.

Future studies should also correlate the Melnikov approach and the Markov approach more closely to dynamically unstable occurrences observed in both model tests and in actual sea operations. On the other hand, the fast turnaround of the two semi-analytical approaches should be fully utilized to obtain more insight in optimizing the design. Such an approach may also be applied in a regulatory framework for both national governments and a classification approach.

# REFERENCES

1. ANSYS Inc., 2011. AQWA-DRFT user manual, Houston, Texas, USA.

2. Astariz, S. and Iglesias, G., 2015. The economics of wave energy: a review, Renew. Sustain. Energy Rev. 45, 397-408.

3. Babarit, A., Mouslim, H., Clément, A., Laporte-Weywada, P., 2009. On the numerical modelling of the nonlinear behavior of a wave energy converter. 28th International Conference on Ocean, Offshore and Arctic Engineering, Honolulu, Hawaii, USA.

4. Beck, R.F., Reed, A.M., 2001. Modern computational methods for ships in a seaway. *SNAME Transaction*, 109, 1-51.

5. Belenky, V.L., Weems, K.M., Lin, W.M., Paulling, J.R., 2003. Probabilistic analysis of roll parametric resonance in head seas. In Proceedings of the 8th International Conference on Stability of Ships and Ocean Vehicles, Madrid, Spain.

6. Bendat, J.S., Piersol, A., 2011. Random Data: Analysis and Measurement Procedures, 4th ed., John Wiley & Sons, New York.

7. Bendat, J.S., Palo, P.A., 1989. Nonlinear System Stochastic Techniques for Ocean Engineering Applications, Tech. Rep., Naval Civil Engineering Laboratory, Port Hueneme, USA.

8. Bendat, J., 1990. Nonlinear System Analysis and Identification from Random Data, 1st ed., John Wiley & Sons, New York.

9.  Bosma, B., Sheng, W., Thiebaut, F., 2014. Performance assessment of a floating power system for the Galway Bay wave energy test site. International Conference on Ocean Energy, Halifax, Canada.

10. CD-adapco, 2014. User Guide STAR-CCM+ Version 9.04.

11. Chen, X., 2002. Studies on Dynamic Interaction between Deep-water Floating Structures and Their Mooring/tendon System. Ph.D. Thesis, Texas A&M University, Texas, USA.

12. Coe, R.G., Neary, V.S., Lawson, M., Yu, Y.H. and Weber, J., 2014. Extreme conditions modelling workshop report, National Renewable Energy Laboratory (NREL), Golden, Colorado, USA.

13. Columbia Power Technologies, 2017. http://columbiapwr.com/why-wave-energy. (Accessed 12 Feb 2018).

14. Cummins, W., 1962. The impulse response function and ship motions. Technical Report, David Taylor Model Basin. Washington D.C., USA.

15. Dietz, J.S., 2004. Application of conditional waves as critical wave episodes for extreme loads on marine structures, PhD thesis, Technical University of Denmark, Denmark.

16. DNV, 2010. Recommended practice: environmental conditions and environmental loads.

17. Drew, B., Plummer, A. and Sahinkaya, M., 2009. A review of wave energy converter technology, Proc. of the Inst. of Mech. Eng., Part A: J. of Power and Energy, 223(8):887-902.

18. Du, S.X., Hudson, D.A., Price, W.G., Temarel, P., 2009. Implicit Expressions of Static and Incident Wave Pressures over the Instantaneous Wetted Surface of Ships. In: Proceedings of the Institution of Mechanical Engineers Part M: Journal of Engineering for the Maritime Environment. 223(3), 239-256.

19. Elhanafi, A., Macfarlane, G., Fleming, A. and Leong, Z., 2017. Experimental and numerical investigations on the intact and damage survivability of a floating-moored oscillating water column device. Appl. Ocean Res., 68, 276-292.

20. Falcão, A.F.de,O., 2010. Wave energy utilization: a review of the technologies, Renew. Sustain. Energy, 14(3):899-918.

21. Falnes, F., 2002. Ocean waves and oscillating systems, Cambridge University Press, Cambridge, UK.

22. Falzarano, J., 1990. Predicting complicated dynamics leading to vessel capsizing. Ph.D. dissertation, University of Michigan.

23. Falzarano, J., Cheng, J. and Rodrigues, W., 2004. Transit draft heave and pitch motion analysis of the mobile offshore base (MOB) using reverse MI/SO techniques, J. Offshore Mech. Arct. Eng. 126 (1), 16-25.

24. Falzarano, J.M., Somayajula, A. and Seah, R., 2015. An overview of the prediction methods for roll damping of ships, Ocean Syst. Eng. 5 (2), 55–76.

25. Feldman, M., 1994. Non-linear system vibration analysis using Hilbert transform: part I free vibration analysis method 'Freevib', Mech. Syst. Signal Process. 8 (2) 119–127.

26. Frey, M., Simiu, E., 1993. Noise-induced chaos and phase space flux. Phys. D Nonlinear Phenom. 63, 321–340.

27. Giorgi, G., Ringwood, J.V., 2017. Relevance of Pressure Field Accuracy for Nonlinear Froude-Krylov Force Calculations for Wave Energy Devices. J. Ocean Eng. Marine Energy 4(1), 57-71.

28. Giorgi, G., Ringwood J.V., 2018. Articulating parametric resonance for an OWC spar buoy in regular and irregular waves. J. Ocean Eng. Mar. Energy, 4, 311–322.

29. Giorgi, G. and Ringwood, J.V. 2019, Analytical representation of nonlinear Froude-Krylov forces for 3-DoF point absorbing wave energy device. Ocean Eng., 164, 749-759.

30. Gomes, R.P.F., Ferreira, J.D.C.M., Silva, S.R., Henriques, J.C.C. and Gato, L.M.C., 2017. An experimental study on the reduction of the dynamic instability in the oscillating water column spar buoy. 12th European Wave and Tidal Energy Conference, Cork, Ireland.

31. Gomes, R. P. F., Henriques, J. C. C., Gato, L. M. C., Falcao, A. F. O., 2012. Testing of a small-scale floating OWC model in a wave flume. 4 th International Conference on Ocean Energy, Dublin, Ireland.

32. Guckenheimer, J., Holmes, P., 1983. Nonlinear Oscillations, Dynamical Systems, and Bifurcations of Vector Fields. Applied Mathematical Sciences. vol. 42, 1st edn. Springer, New York.

33. Guha, A., 2012. Development of a Computer Program for Three Dimensional Frequency Domain Analysis of Zero Speed First Order Wave Body Interaction (Master's thesis), Texas A&M University, College Station, USA.

34. Guha, A., 2016. Development and application of a potential flow computer program: Determining first and second order wave forces at zero and forward speed in deep and intermediate water depth, PhD Thesis, Texas A&M University.

35. Hall, M., Goupee, A., 2015. Validation of a lumped-mass mooring line model with DeepCwind semisubmersible model test data. Ocean Eng. 104, 590-603.

36. Handschel, S., Feder, D.-F., Abdel-Maksoud, M., 2015. Estimation of ship roll damping - a comparison of the decay and the harmonic excited roll motion technique for a post panamax container ship Proc. 12th International Conference on the Stability of Ships and Ocean Vehicles, Glasgow, UK.

37. Haslum, H., 2000. Simplified methods applied to nonlinear motion of spar platforms. Ph.D. dissertation, Norwegian University of Science and Technology.

38. Haslum, H., Olje, U., Faltinsen, O.M., 1999. Alternative shape of spar platforms for use in hostile areas. Proceedings of Offshore Technology Conference, 1–12.

39. Hsieh, S.R., Troesch, A.W., Shaw, S.W., 1994. A nonlinear probabilistic method for predicting vessel capsizing in random beam seas. Transactions of the Royal Society of London Series A-Mathematical and Physical Sciences, 446 (1926), 195-211.

40. Jang, H.K., Kim, M.H., 2019. Mathieu instability of Arctic Spar by nonlinear time-domain simulations. Ocean Eng. 176, 31-45.

41. Jang, H.K., Kim, M.H., 2020. Effects of nonlinear FK (Froude-Krylov) and hydrostatic restoring forces on arctic-spar motions in waves. Int. J. Nav. Archit. Ocean Eng. 12, 297-313.

42. Jiang, C., Troesch, A.W., Shaw, S.W., 2000. Capsize criteria for ship models with memory-dependent hydrodynamics and random excitation. Philos. Trans. R. Soc. London Ser. A Math. Phys. Eng. Sci. 358 (1771), 1761-1791.

43. Koo, B.J., Kim, M.H., Randall, R.E., 2004. Mathieu instability of a spar platform with mooring and risers. Ocean Eng. 31, 2175–2208.

44. Korde, U. and Ringwood, J., 2016. Hydrodynamic control of wave energy devices, Cambridge University Press, Cambridge, UK.

45. Kurniawan, A., Grassow, M. and Ferri, F., 2019. Numerical modelling and wave tank testing of a self-reacting two-body wave energy device. *Ships and Offshore Structures*, 14, 344-356.

46. Lawson, M., Garzon, B.B., Wendt, F., Yu, Y.H. and Michelen, C., 2015. COER hydrodynamic modelling competition: modelling the dynamic response of a floating body using the WEC-Sim and FAST simulation tools. In Proceedings of the ASME 2015 34th International Conference on Ocean, Offshore and Arctic Engineering, St. John's, Newfoundland, Canada.

47. Lawson, M., Yu, Y.H., Nelessen, A., Ruehl, K. and Michelen, C., 2014. Implementing nonlinear buoyancy and excitation forces in the WEC-Sim wave energy converter modelling tool. 33rd International Conference on Ocean, Offshore and Arctic Engineering, San Francisco, California, USA.

48. Lettenmaier, T., Amon, E. and Jouanne, A., 2013. Power converter and control system developed in the ocean sentinel instrumentation buoy for testing wave energy

converters, in: IEEE Energy Conversion Congress and Exposition (ECCE), Denver, USA.

49. Leontaritis, I.J. and Billings, S.A., 1985. Input–output parametric models for non-linear systems: part I. deterministic non-linear systems, Int. J. Control 41 (2), 303–328.

50. Li, B.B., Ou, J.P. and Teng, B., 2011. Numerical investigation of damping effects on coupled heave and pitch motion of an innovative deep draft multi spar, J. Mar. Sci. Technol. 19 (2), 231-244.

51. Liu, Y. and Falzarano, J., 2017. Suppression of irregular frequency effect in hydrodynamic problems and free-surface singularity treatment. J. Offshore Mech. Arct. Eng. 139, 1-16.

52. Lópeza, I., Andreu, J., Ceballos, S., Alegria, I.M. and Kortabarria, I., 2013. Review of wave energy technologies and the necessary power-equipment, Renew. Sustain. Energy 27(0), 413-434.

53. Mao, H., Yang, H., 2016. Parametric pitch instability investigation of deep draft semi-submersible platform in irregular waves. Int. J. Nav. Archit. Ocean Eng. 8, 13–21.

54. MAP++ Documentation Release 1.15. https://map-plus-plus.readthedocs.io/en/latest (accessed on 03 Jan 2019).

55. Masciola, M., 2018. MAP++ Documentation Release 1.15, https://map-plus-plus. Readthedocs.io/en/latest (accessed 12 Feb 2018)

56. Masciola, M., Jonkman, J. and Robertson, A., 2013. Implementation of a multisigmented, quasi-static cable mode. In Proceedings of the 23rd International Offshore and Polar Engineering Conference. Anchorage, Alaska, USA.

57. Masri, S.F., Miller, R.K., Saud, A.F. and Caughey, T.K., 1987. Identification of nonlinear vibrating structures: part I formulation, J. Appl. Mech. 54 (4) 918–922.

58. Melnikov, V., 1963. On the stability of the center for time-periodic perturbations. Trans. Mosc. Math. Soc. 12, 1–57.

59. Nallayarasu, S. and Mathai, T.P., 2016. Effect of Mathieu instability on motion response of Spar hull with heave damping plate, Ships Offshore Struct. 11 (8) 833-846.

60. Nallayarasu, S. and Kumar, N., 2017. Experimental and numerical investigation on hydrodynamic response of buoy form spar under regular waves, Ships Offshore Struct. 12 (1) 19-31.

61. OrcaFlex Documentation. Available online: http://www.orcina.com/Software /Products/OrcaFlex/ Documentation/Help. (accessed 05 Feb 2019)

62. Ogilvie, T., 1983. Second-order hydrodynamic effects on ocean platforms. In: International Workshop on Ship and Platform Motions, Berkley, CA, USA.

63. OpenFOAM Foundation Ltd., 2019. OpenFOAM User Guide.

64. Orszaghova, J., Wolgamot, H., Draper, S., Eatock Taylor, R., Taylor, P.H. and Rafiee, A., 2019. Transverse motion instability of a submerged moored buoy. In Proceedings of the Royal Society A-Mathematical Physical and Engineering Sciences, 475.

65. Palm. J., Eskilsson, C., Bergdahl, L., 2018. Parametric excitation of moored wave energy converters using viscous and non-viscous CFD simulations. 3rd International Conference on Renewable Energies Offshore, Lisbon, Portugal.

66. Palo, P.A., Bendat, J.S., Coppolino, R.N., 1998. Identification of Low-Order Equation of Motion for Nonlinear Stability Studies. In: Stochastically Excited Nonlinear Ocean Structures. World Scientific, Singapore, 266-278.

67. Ransley, E.J., Greaves, D., Raby, A., Simmonds, D. and Hann, M., 2017. Survivability of wave energy converters using CFD. *Renew. Energy* 109, 235-247.

68. Pastoor, L.W., 2002. On the assessment of nonlinear ship motions and loads, PhD thesis, Technical University Delft, Netherland.

69. Payne, G. S., Taylor, J. R. M., Bruce, T., Parkin, P., 2008. Assessment of boundary-element method for modelling a free-floating sloped wave energy device. Part 2: Experimental validation. Ocean Eng. 35 (3-4), 342–357.

70. Reed, A. and Beck, R., 2017. Advances in the predictive capability for ship dynamics in extreme waves, Proceedings of SNAME, Houston, Texas.

71. Penalba, M., Giorgi, G. and Ringwood, J., 2017. Mathematical modelling of wave energy converters: A review of nonlinear approaches. *Renew. Sustain. Energy. Rev.* 78, 1188-1207.

72. Pinkster, J., 1980. Low Frequency Second Order Wave Exciting Forces on Floating Structures (Ph.D. dissertation), Delft University of Technology, Netherlands.

73. Poguluri, S.K., Cho, I.H. and Bae, Y.H., 2019. A study of the hydrodynamic performance of a pitch-type wave energy converter–rotor, Energies 12 (5) 1-16.

74. Ruehl, K., Michelen, C., Bosma, B. and Yu, Y.H., 2016. WEC-Sim Phase 1 validation testing: numerical modelling of experiments. International Conference on Offshore Mechanics and Arctic Engineering, Busan, South Korea.

75. Sagaut, P., 2006. *Large Eddy Simulation for Incompressible Flows: An Introduction*. Springer-Verlag: New York, USA.

76. Sheng, W., Flannery, B., Lewis, A., Alcorn, R., 2012. Experimental studies of a floating cylindrical OWC WEC. 31st International Conference on Ocean, Offshore and Arctic Engineering, Rio de Janeiro, Brazil.

77. Sirnivas, S., Yu, Y.H., Hall, M. and Bosma, B., 2016. Coupled mooring analyses for the WEC-SIM wave energy converter design tool. In Proceedings of the ASME 2016 35th International Conference on Ocean, Offshore and Arctic Engineering, Busan, South Korea.

78. Shami, E., Zhang R., Wang, X., 2018. Point absorber wave energy harvesters: a review of recent developments, Energies, MDPI, Open Access Journal, 12(1), 1-36.

79. Somayajula, A., 2017. Reliability assessment of hull forms susceptible to parametric roll in irregular seas. Ph.D. dissertation, Texas A&M University.

80. Somayajula, A. and Falzarano, J., 2015. Large-amplitude time-domain simulation tool for marine and offshore motion prediction, Mar. Syst. & Ocean Technol., 10(1):1-17.

81. Somayajula, A. and Falzarano, J.M., 2016. Critical assessment of reverse-MISO techniques for system identification of coupled roll motion of ships, J. Mar. Sci. Technol. 1–19.

82. Somayajula, A. and Falzarano, J., 2017. Application of advanced system identification technique to extract roll damping from model tests in order to accurately predict roll motions, Applied Ocean Research, 67:125-135.

83. Somayajula, A. and Falzarano, J., 2017. A comparative assessment of approximate methods to simulate second order roll motion of FPSOs. *Ocean Syst. Eng.* 7, 53–74.

84. Somayajula, A., Falzarano, J., 2019. Parametric roll vulnerability of ships using Markov and Melnikov approaches. Nonlinear Dyn. 97 (4), 1977-2001.

85. Somayajula, A., Falzarano, J., Lutes, L., 2019. An efficient assessment of vulnerability of a ship to parametric roll in irregular seas using first passage statistics. Probab. Eng. Mech. 58, 102998.

86. Stern, F., Carrica, P., Kandasamy, M. and Ooi, S.K. et al., 2008. Computational Hydrodynamic Tools for High-speed Sealift: Phase II Final Report. The University of Iowa, Iowa City, Iowa, USA.

87. Su, Z., 2012. Nonlinear response and stability analysis of vessel rolling motion in random waves using stochastic dynamical systems. Ph.D. dissertation, Texas A&M University.

88. Su, Z., Falzarano, J., 2013. Markov and Melnikov based methods for vessel capsizing criteria. Ocean Eng. 64, 146-152.

89. Tarrant, K. and Meskell, C., 2016. Investigation on parametrically excited motions of point absorbers in regular waves. *Ocean Eng.*, 111, 67-81.

90. The National Renewable Energy Laboratory and Sandia Corporation, 2014. WEC-Sim User Guide Version 1.0.

91. Umeda, N., Hashimoto, H., Tsukamoto, I. and Sogawa, Y., 2012. Estimation of parametric roll in random seaway. In *Parametric Resonance in Dynamical Systems*, Fossen, T.I., Nijmeijer, H., Eds.; Springer, New York, USA, 45-59.

92. WAMIT Inc., 2013. WAMIT User Manual Version 7.0.

93. Wang, H. and Falzarano, J., 2013. Energy extraction from the motion of an oscillating water column, Ocean System Engineering, 3(4):327-348.

94. Wang, H. and Falzarano, J., 2017, Energy balance analysis method in oscillating type wave converter, Journal of Ocean Engineering and Marine Energy, 3(3):193-208.

95. Wang, H., Sitanggang, K. and Falzarano, J. 2017, Exploration of power take off in wave energy converters with two bodies interactions. Ocean System Engineering, 7(2):89-106.

96. Wang, H., Somayajula, A. and Falzarano, J.M., 2020a. Application of system identification technique in efficient model test correlations for a floating power system, Appl. Ocean Res. 98, 102126.

97. Wang, H., Somayajula, A., Falzarano, J.M. and Xie, Z., 2020b. Development of a blended time-domain program for predicting the motions of a wave energy structure. J. Mar. Sci. Eng. 8(1).

98. Water Power Technologies Office, 2016. https://www.energy.gov/eere/water/articles/ aquaharmonics-tests-michigan-and-enjoys-chilly-weather.

99. WEC-Sim Documentation. http://wec-sim.github.io/WEC-Sim/index.html (accessed on 31 Apr 2019).

100. Wheeler, J.D.E., 1970. Method for Calculating Forces Produced by Irregular Waves. Journal of Petroleum Technology. 22 (3), 359-367.

101. Wiggins, S., 2003. Introduction to Applied Nonlinear Dynamical Systems and Chaos, Springer-Verlag, New York.

102. Xie, Z., Liu, Y. and Falzarano, J., 2019. A numerical evaluation of the quadratic transfer function for a floating structure. In Proceedings of the ASME 2019 38th International Conference on Ocean, Offshore and Arctic Engineering, Glasgow, UK.

103. Yang, M., Teng, B., Ning, D., Shi, Z., 2012. Coupled dynamic analysis for wave interaction with a truss spar and its mooring line/riser system in time domain. Ocean Eng. 39, 72-87.

104. Yeylaghi, S., Moa, B., Beatty, S., Buckham, B., Oshkai, P. and Crawford, C., 2015. SPH modelling of hydrodynamic loads on a point absorber wave energy converter hull. 11th European Wave and Tidal Energy Conference, Nantes, France.

105. Yu, Y.H., 2017. WEC-Sim (a time-domain numerical model) development, verification and validation, National Renewable Energy Laboratory, Golden. Colorado, USA.

106. Yu, Y.H., Rij, J., Coe, R. and Lawson, M., 2015, Preliminary wave energy converters extreme load analysis, 34th International Conference on Ocean, Offshore and Arctic Engineering, St. John's, Canada.